Fields, Fractals and Flares: Characterising Magnetic Complexity in Solar Active Regions

Paul A. Conlon, B.Sc (Hons), M.Sc

School of Physics

University of Dublin, Trinity College

A thesis submitted for the degree of

PhilosophiæDoctor (PhD)

2009 October

Declaration

I, Paul A. Conlon, hereby certify that I am the sole author of this thesis and that all the work presented in it, unless otherwise referenced, is entirely my own. I also declare that this work has not been submitted, in whole or in part, to any other university or college for any degree or other qualification.

Name: Paul A. Conlon

Signature: .... **Date:** ....

The thesis work was conducted from October 2006 to October 2009 under the supervision of Dr. Peter T. Gallagher at Trinity College, University of Dublin.

In submitting this thesis to the University of Dublin I agree that the University Library may lend or copy the thesis upon request.

Name: Paul A. Conlon

Signature: .... **Date:** ....

Summary

The main drivers of space weather, solar flares and coronal mass ejections, are thought to originate from active regions on the surface of the Sun. The mechanisms by which active regions produce these eruptive events remains unclear. In this thesis, numerous mathematical methods are developed to characterise the complexity of active region magnetic fields on the Sun.

In the first section of the thesis, a box-counting method was used to measure the temporal evolution of the multifractal parameters of a sample of active regions. These results are compared to other multi-scale methods and changes in the temporal evolution of the multifractal spectrum are found to be associated with a regions flaring potential. As an expansion of the box-counting method, a wavelet-based multifractal method, the wavelet transform modulus methods (WTMM), was similarly used to characterise the changing properties of active region magnetic fields. A study of the multifractal properties of active and quiet Sun magnetic fields showed them to be statistically distinct and separable in wavelet transform space. As such, a segmentation procedure was developed to accurately recover the multifractal parameters of active region magnetic fields from the surrounding quiet Sun. Additionally, the temporal evolution of the fractal dimension and Hölder exponent of active regions were examined for a possible relation to flaring.

The complexity of the coronal field was investigated using extrapolation techniques. A linear force-free extrapolation method was developed to examine the changing topology of active region magnetic fields. Comparisons were made to EUV observations of the solar corona so as to constrain the extrapolations. Using the twin perspectives of the *Solar TErrestrial RElations Observatory (STEREO)* spacecraft the 3D topology of a coronal loop was identified and modelled with time. Changes in the amount of twist, free energy and connectivity of the loop were related to magnetic flux emergence in NOAA 10956.

To Mom and everyone who made me who I am.

Acknowledgements

I would like to thank all the staff in the School of Physics for making my time at Trinity College enjoyable and exciting. A special thanks is due to Dr. Peter Gallagher for his encouragement, dedication, and guidance. Without his help and support, this work would never have been possible.

I would also like to thank Dr. R.T. James McAteer and Dr. D. Shaun Bloomfield for their guidance, assistance and general banter. I am also grateful to, in no particular order, Jack Ireland, Alex Young, and Ryan Milligan for their wisdom, helpfulness and creativity.

To all my fellow ARG members, especially Claire and Jason, a big thank you for all the tea and gossip at lunch time.

A special thanks to all the staff in the School of Mathematical Science in University College Dublin for their passion and ability to instil wonder and awe in me.

For my family without your financial and emotional support would I be who I am today. In particular the numerous free dinners at random points during my studies were very much welcome.

Lastly to my wonderful girlfriend, Caireann, thanks for putting up with me when others wouldn't, reading when I couldn't read, and spending your Sundays correcting my spelling and grammar in a subject in which you have no knowledge.

Referred Publications

1. Kestener P., **Conlon P.A.**, Khalil A , Arneodo A., McAteer R.T.J., Gallagher P.T., and Fennell L.,

   “Characterising Complexity in Compound Systems I: Segmentation in Wavelet-Space”

   Astrophysics Journal, *submitted*, 2009

2. **Conlon P.A.**, Kestener P., McAteer R.T.J., Gallagher P.T., Fennell L., Khalil A. , and Arneodo A.,

   “Characterising Complexity in Compound Systems II: Magnetic Fields, Flares & Forecasts”

   Astrophysics Journal, *submitted*, 2009

3. **Conlon P.A.** and Gallagher P.T.

   “Constraining Magnetic Field Extrapolations of a Solar Active Region Using *STEREO*”

   Astrophysics Journal, *submitted*, 2009

4. McAteer R.T.J., Gallagher P.T., & **Conlon P.A.**

   “Turbulence, Complexity, and Solar Flares”

   Advances in Space Research, accepted, Sept. 2009

---

5. **Conlon P. A.**, Gallagher P. T. , McAteer R. T. J. , Ireland J., Young C.A., Kestener P., Heweitt R., Maguire K.

   “Multifractal Properties of Evolving Active Regions”

   Solar Physics, 248(2), 297, 2008

6. Hewett, R. J., Gallagher, P. T., McAteer, R. T. J., Young, C. A., Ireland, J., **Conlon, P. A.**, Maguire, K.

   “Multiscale Analysis of Active Region Evolution”

   Solar Physics, 248(2), 311, 2008

7. DeRosa M.L., Schrijver C.J., Barnes G., Leka K. D., Lites B.W., Aschwanden M.J., Amari T., Canou A., McTiernan J.M., Rgnier S., Thalmann J,K., Valori G., Wheatland M.S., Wiegelmann T., Cheung M.C.M., **Conlon P.A.**, Fuhrmann M., Inhester B., Tadesse T.

   “A Critical Assessment of Nonlinear Force-Free Field Modeling of the Solar Corona for Active Region 10953”

   Astrophysical Journal, 696(2), 1780, 2009

8. Gallagher, P. T., McAteer, R. T. J., Young, C. A., Ireland, J., Hewett, R., **Conlon, P.**,

   “Solar Activity Monitoring”

   In J. Lilensten (ed) ”In SPACE WEATHER: Research towards Applications in Europe”, Springer, (2006).

Contents

List of Figures

List of Tables

1

Introduction

Humankind has studied the Sun since the dawn of civilisation. As the source of all life on the Earth is has often been worshipped and studied. Since the Irish Celts built Newgrange as a place of burial and worship 5,000 years ago, mankind has been willing, at a great expense and effort, to understand our nearest star. Each epoch of man has studied the Sun to better understand and harness its power. The Celts and early man strove to gain a better understanding of the seasons. Accurate calendars were necessary for the growth and cultivation of crops and therefore the survival of the human race depended on their existence. The aurora borealis (the northern and southern lights) have left many a man in a state of awe. While the aurora are a beautiful sight to behold, they and the Sun represent an ever present danger to modern telecommunication systems and power grids. The energetic particles that bombard the Earth on a daily basis, also have the potential to disrupt satellite communications, electromagnetic networks and explorations of space (National Academies Press, 2008). These events are collectively known as space weather. An ever increasing number of scientists are trying to understand and ultimately forecast the effect space weather has on the Earth and all electronic based infrastructure. The importance this research has on the future of the human race can be measured in the collective efforts of the world governments, and the funds they have made available for the study of the Sun and space weather.

The purpose of this thesis is to study the formation and evolution of solar active regions or sunspots. Active regions are the source of the majority of space weather events that affect the Earth. Active regions are regions of intense magnetic fields on the surface of the Sun. They are highly dynamic and complex structures as shall be shown. This work presents my own contributions to the study of our nearest star. It is my hope that it shall advance our ability to better understand and hopefully predict the events on the Sun and understand their interaction with the Earth. I shall begin with an introduction to the structure and atmosphere of the Sun, as both play important parts in the formation, evolution and study of sunspots.

1.1 The Sun

1.1.1 Facts and Figures

The Sun is one of many billions of stars that make up our galaxy. However, given its close proximity to the Earth, it is interesting to study the Sun as it is the primary source of energy to our planet. Furthermore, it provides us with an insight into stellar structures and astrophysical plasmas.

As a star, the Sun is rather mundane. It is a standard medium-sized star and at 4.6×10^9 years old, it is already half way through its lifetime. Its total mass is 1.99×10^{30} kg, of which 74% of the mass is hydrogen, 24% helium, and small traces of large elements such as oxygen, iron, magnesium, and silicon. Every second, 4.26×10^9 kg of the Sun, is converted into energy by the nuclear fusion reactions taking place inside its core. The radius of the Sun ($R_\odot$) is 696 Mm, where 1 Mm is 10^6 m. Mega-meters are a commonly used length scale on the Sun (a photospheric granule is typically 1 Mm across). 1.3 million Earths would fit into its volume. At its equator, it rotates approximately every 26 days, with the rotational period increasing with latitude to about 35 days near the poles. This effect is know as *differential rotation* and occurs due to the Sun being a gaseous ball of plasma and not a solid body.

1.1.2 Structure

The standard model of the Sun is shown in Figure 1.1. The Sun has a dense core, where temperatures reach $\sim$ 13 MK. These temperatures and densities are sufficient to support nuclear fusion. The core is surrounded by a dense radiative zone. It is so dense that the individual photons created in the core take $\sim 10^6$ years to reach the surface. Surrounding the radiation zone is the convective zone, where energy is transported by large scale convective cells driven by the temperature difference between the inner and outer layers of the Sun. The surface of the Sun is known as the photosphere and is the boundary between the solar interior and atmosphere. The solar atmosphere consists of the chromosphere, transition zone, and corona.

1.1.3 Interior

As the Sun is observed to be neither contracting or expanding, it can be assumed that it is in a state of hydrostatic equilibrium. Therefore, at every depth inside the Sun the weight of the overlying material is balanced by the outward pressure. Starting with the equation of motion and assuming that the plasma in the Sun is in a state of hydrostatic equilibrium, we can derive that the pressure at the centre of the Sun is $P_c = GM^2/8\pi R_{\odot}^4 = 4.4 \times 10^{13} Nm^{-2}$, where P_c is the pressure at the centre of the Sun, G the gravitational constant, M the mass of the Sun and $R_{\odot}$ its radius (Prialnik, 2000). As such the plasma at the centre of the Sun is under extreme pressure and highly compact, with temperatures reaching 13 MK. These are ideal conditions for the production of helium under nuclear fusion. The dominant process of nuclear fusion in the core is known as the proton-proton (pp) chain. The pp chain involves the fusion

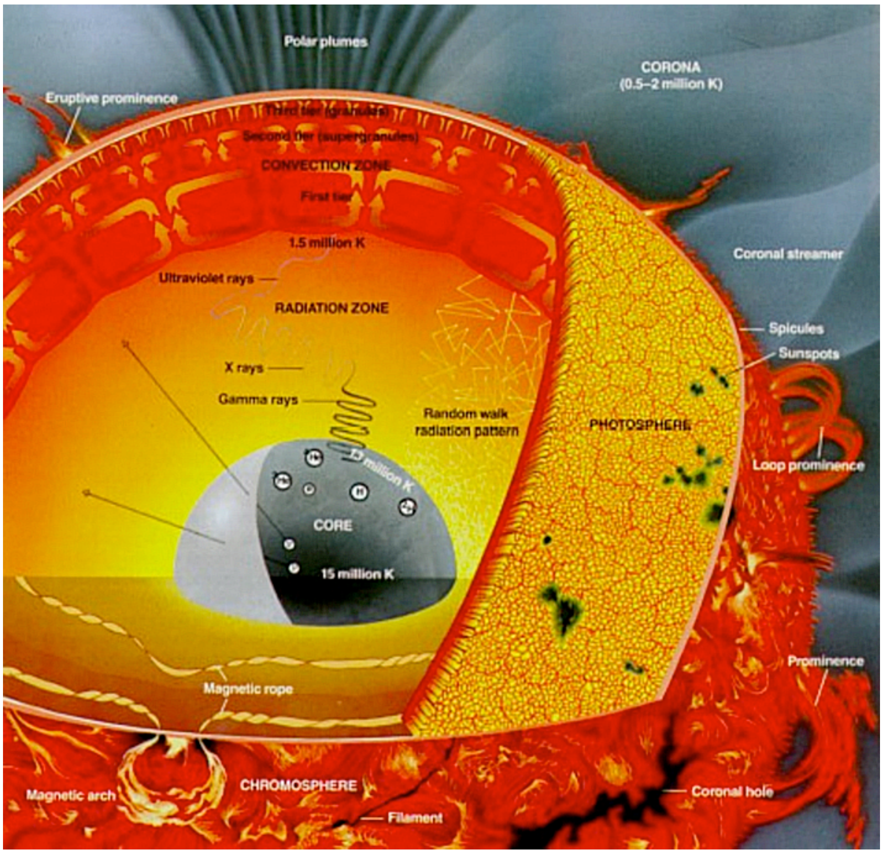

Figure 1.1: Cartoon view of the structure of the active Sun. The core is the source of energy, where fusion heats the plasma to ∼15 MK. Energy is transported away from the core by radiative diffusion in the radiative zone, which extends to $0.75R_{\odot}$. The convection zone is heated from the base at the tachocline, allowing convective currents to flow to the photosphere. Strong magnetic fields inhibit convection and appear as dark *sunspots* on the photosphere. These strong magnetic fields extend into the upper atmosphere of the Sun. Closed field lines are seen as coronal loops and open fields are visible as coronal holes (near the poles; courtesy of *eu.spaceref.com*).

of four protons to form a helium nucleus through a series of nuclear reactions and is outlined as follows:

$$^{1}H +^{1} H \rightarrow {}^{2}D + e^{+}\nu \tag{1.1}$$

$$^{2}D +^{1} H \rightarrow {}^{3}He + \gamma \tag{1.2}$$

$$^{3}He +^{3} He \rightarrow {}^{4}He +^{1} H +^{1} H, \tag{1.3}$$

where ^1H denotes a proton, ^3He a helium nucleus with one neutron, ^4He one with two neutrons, e^+ a positron, ν a neutrino and γ a gamma ray. Every complete pp chain is accompanied with the release of energy, approximately $4.3 \times 10^{-12} J$. The luminosity of the Sun is $3.85 \times 10^{26} W$, therefore we estimate that 9.2×10^{37} fusion reactions occur every second in the core. The solar core extends to 0.25 $R_\odot$ above which lies the radiative zone.

The radiative zone extends from 0.25 to 0.75 $R_\odot$, with a temperature range of 10MK - 5MK. Due to the high densities in the core and radiative zone the gamma rays produced by the pp chain continuously scatter when they encounter free electrons, protons and atomic nuclei. Those absorbed by atomic nuclei are quickly stripped away, resulting in no net increase in energy or particle motion within the plasma. The resulting random walk through the radiative zone under this process means protons from the core take on average $\sim 10^6$ years to reach the surrounding convective zone, compared to the 8 minutes it takes protons to reach the Earth.

The convective zone starts at 0.7 $R_\odot$ and extends to the Sun's surface which is known as the photosphere. Lower temperatures in the convective zone allow for the recombination of electrons and ions. This recombination allows for the absorption of photons, resulting in the localised heating of plasma elements and the formation of convective cells below the solar surface. The convective cells carry the hot gas from the tachocline to the photosphere where it cools. Upon cooling, the material is transported back and the process continues. These convective cells are visible on the solar surface as super-granules.

These convective cells are thought to be the cause and/or the sustaining power behind the solar magnetic field. The solar magnetic field can be pictured as a dipole magnetic field, similar to the magnetic field of the Earth. Unlike the terrestrial magnetic field the solar field varies on an 11-year cycle. The non-uniform differential rotation in the convective zone realigns the global dipole field into a toroidal field (Figure 1.2; Bab-

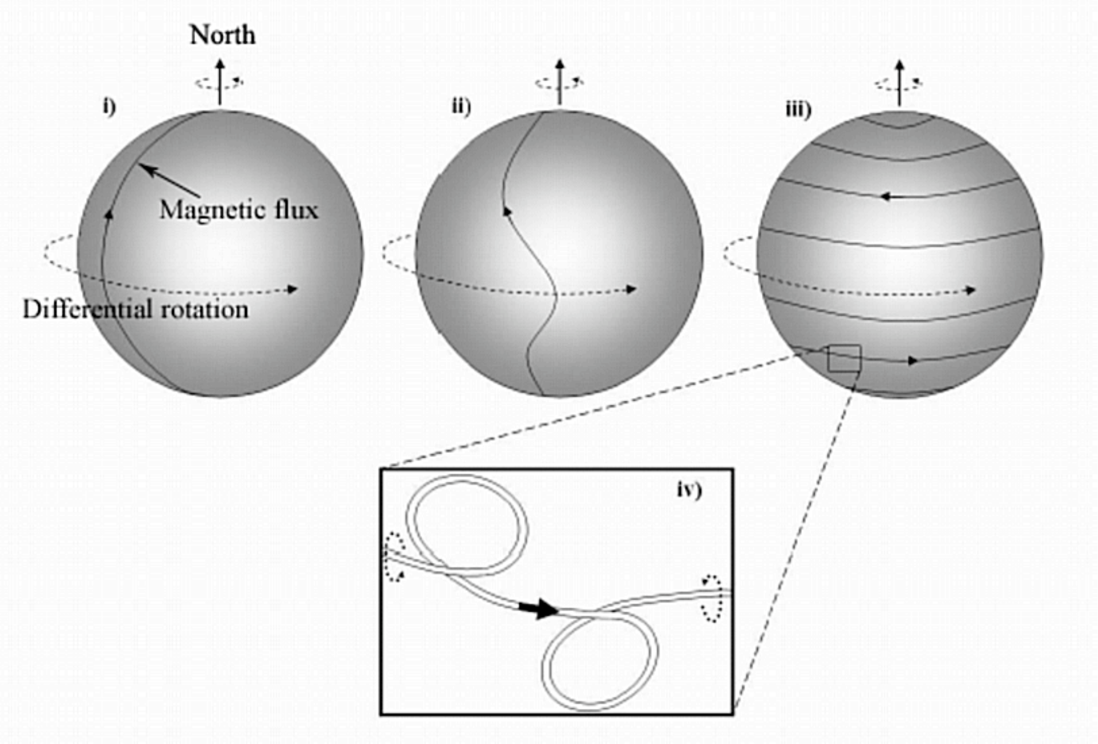

Figure 1.2: The Sun's changing magnetic field. Differential rotation drags the dipole magnetic field of the Sun. The combined effects of the Coriolis force and magnetic buoyancy, twist and lift magnetic field lines towards the surface. The resulting Ω-like structures emerge as active regions on the Sun (O'Neill, 2006).

cock 1953). Turbulent motion in the convective zone causes the magnetic field to become buoyant and rise to the photosphere. These magnetic elements or flux tubes emerge as dipole pairs and appear as dark spots on the photosphere. The magnetic field restricts the convective motions near the photosphere lowering the temperature of the sunspots compared to the surrounding plasma. Over time, these magnetic elements approach the equator where they eliminate each other and the magnetic field orientation flips, and the processes is repeated again.

1.1.4 Atmosphere

Figure 1.3 shows the temperature and density variations between the photosphere and the interplanetary medium. From this it is easy to see the distinct regions of the Sun's

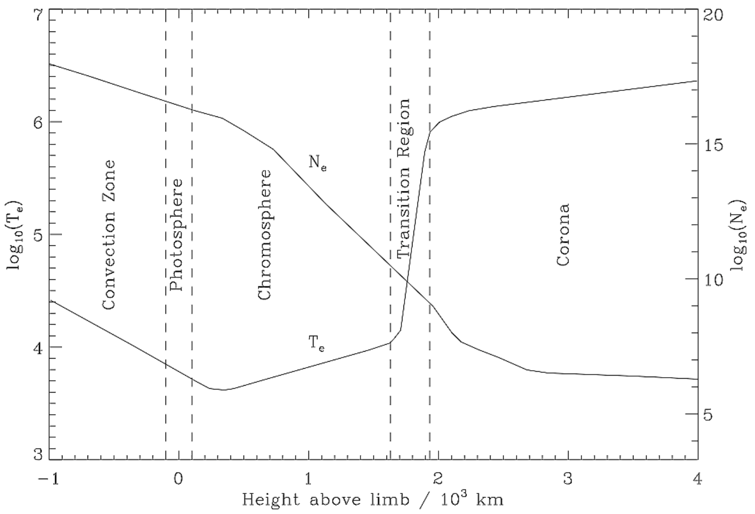

Figure 1.3: A model of electron density and temperature model in the chromosphere and lower corona. In the chromosphere, the plasma is only partially ionised. The plasma becomes fully ionised at the sharp transition from chromospheric to coronal temperatures. n_e indicates the electron density, n_{H_o} the neutral hydrogen density (courtesy of Gallagher 1999).

atmosphere, the photosphere, chromosphere, transition region, and corona.

The photosphere is where the Sun radiates the majority of its energy, in the form of visible and infrared light. The distribution of photospheric radiation closely follows that of a black body at 6,000 K, which can be taken as the temperature of the photosphere. Absorption lines along the solar spectrum allow us to analyse the structure of the photosphere in great detail. Due to the Zeeman splitting of magnetically sensitive lines measurements of the local magnetic field can be inferred. The magnetic field of the photosphere can be separated into three classes, quiet sun, active sun and the polar fields. Quiet Sun magnetic fields are ephemeral regions which rise with the convective flows and rest along the intra-granular network. Active regions are several orders of magnitude larger in both terms of area and magnetic field strength. Their number and strength follows the 11-year cycle of the solar dipole field. Under dynamo theory the polar magnetic field is a consequence of the rise and decay of active regions. As the number of active regions increases, flux is transported from the equatorial regions to

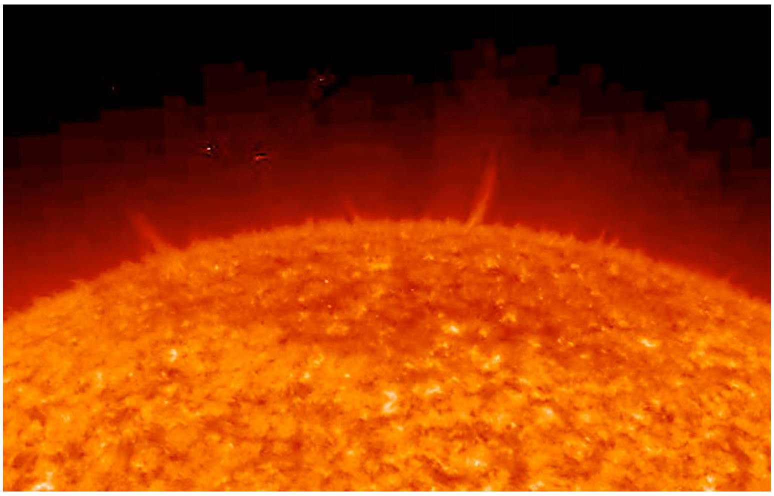

Figure 1.4: A close up view of the top of the Sun as seen in profile shows thousands of little spurts, know as spicules. Image courtesy of the *STEREO* science mission.

the poles by the meridional flow. This process weakens the polar field over time. At solar maximum the polar field is at a minimum. The transfer of flux from the equator to the poles eventually causes the polar fields to switch polarity and increase in strength as the number of active regions starts to decrease.

High resolution observations of the photosphere reveals its dynamic and chaotic granular structure. Analysis of waves within this granular structure allow helioseismologists to investigate the interior of the Sun. Observations taken closer to the solar limb allow for the analysis of different heights within the thin photosphere. This is due to an increase in the line-of-sight (LOS) emission and is the cause of the observed limb darkening, as higher altitudes are cooler by up to 2,000 K.

The chromosphere lies above the photosphere. Visible at the precise moment when a total eclipse begins, it is a dynamic structure characterised by a rise in temperature with height (Phillips, 1998). Special observational filters are required to analyse the structure of the chromosphere in the absence of an eclipse. Observations of the chromospheric limb show numerous narrow columns known as *spicules*, which are seen to fade in and out of view as they oscillate or rotate, Figure 1.4.

The outer atmosphere of the Sun is know as the corona. The corona is an extremely hot and tenuous region, with temperatures in the region of 2 MK and hotter in regions associated with sun spots. It becomes visible in white light during a solar eclipse or with the use of an artificial occulting disk. Such high temperatures fully ionise the mostly hydrogen gas resulting in the emission of X-rays, extreme ultraviolet and radio radiation.

The dominating force in the corona is described by the plasma β , which is the ratio of gas pressure to magnetic pressure, ($\beta = 16\pi\xi n K_B T/\mathbf{B}^2$). In the corona $\mathbf{B} = 10$ G, $n = 10^9$ cm^{-3} and $T = 3 \times 10^6$ K, giving a plasma β of 0.2 (Gary, 2001). Therefore the magnetic field is the dominant force in the corona.

There are two distinct magnetic zones in the corona: Open and closed magnetic field regions, each with different magnetic topologies. Open magnetic fields always exist in the polar regions and can extend towards the equator in the form of coronal holes. These regions of open magnetic flux connect the solar surface to the interplanetary field and are the source of the fast solar wind ($\approx$ 800 km/s). Closed-field regions consist of closed field lines that reconnect to the solar surface and produce the slow solar wind ($\approx$ 400 km/s).

The hot, tenuous corona is separated from the cooler chromosphere by the transition region. The transition region marks the boundary between the neutral matter of the chromosphere and the ionised corona. The energy required to power the corona must pass from the photosphere, through the chromosphere and heat the solar matter across the small length scale of the transition region. It is therefore a highly dynamic interface layer (Gallagher, 2000)

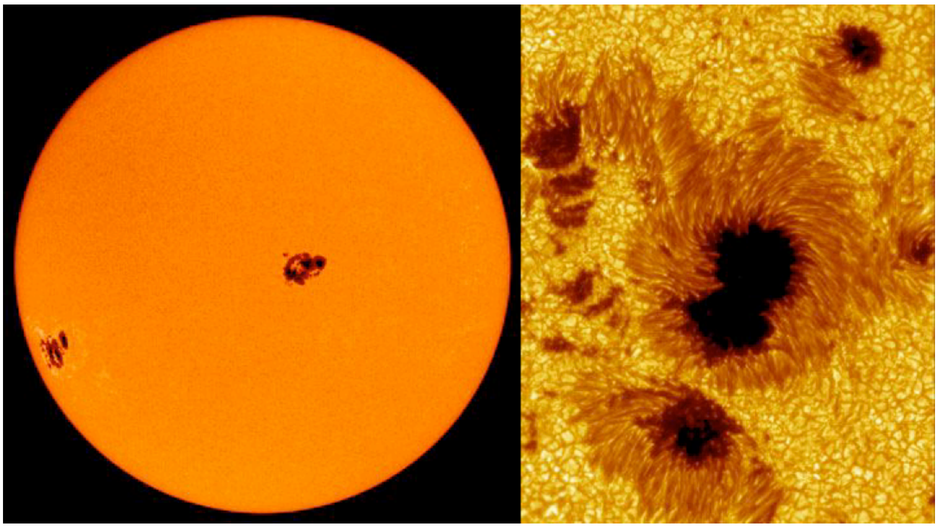

Figure 1.5: Left: Full disk MDI intensity image of the Sun, showing two Jupiter-sized sunspot groups on the face of the Sun. Right: Close-up of a large sunspot group. The central dark part of the large sunspot in the middle of the right hand image is about 14,000 km. Images courtesy *SOHO* (NASA & ESA) and the Royal Swedish Academy of Sciences.

1.2 Active Regions

Active regions, also known as sunspots, appear within $\pm 40^o$ of the solar equator and can grow to cover 1% of the solar disk (Zirin, 1988). Sunspots are regions of kilo-Gauss magnetic fields which emerge from the sub-surface of the sun and expand rapidly into the solar atmosphere. Their global structure and evolution is governed by photospheric and sub-surface flows. As already mentioned the strong magnetic fields present in active regions inhibit the convective flows causing a reduction in temperature compared to the surrounding regions. The dark interior of a sunspot is known as the *umbra* and the lighter area surrounding this is known as the *penumbra*. The penumbra consist of finer filaments which point radially away from the umbra in simple sunspots. Figure 1.5 shows the detailed structure of active regions.

Solar active regions are traditionally classified using one of two systems, the Mount Wilson and McIntosh classification systems (Hale *et al.*, 1919; McIntosh, 1990). At present these two main methods are currently applied to all active regions by eye. This

Table 1.1: Mount Wilson Sunspot Magnetic Classification (SpaceWeather, 2006)

Class	Description
α	A unipolar sunspot group
β	A bipolar sunspot group with a clear, simple division between the polarities
γ	A complex region of positive and negative polarities, a salt and pepper distribution, too complex to classify it as a β
δ	A qualifier to magnetic classes indicating that the umbrae separated by less than 2 degrees within one penumbra have opposite polarity.

results in a non-repeatable and highly subjective classification. The Mount Wilson method, introduced in 1919, outlines the classification of sunspot groups based on the sunspot configuration and characteristics. Each region is coded with a combination of designations which are based on the unipolar(α), bipolar(β) or multipolar(γ) nature of the spots, see Table 1.1.

The McIntosh classification system is a 3-component system, which uses a modified Zurich Sunspot classification for it's first entry. The second component is descriptive of the largest spot in the group and the last entry details the degree of spottiness in the interior of the sunspot group. In all the system has 60 distinct types of sunspot groups. The classification system is outlined in Figure 1.6.

Current prediction techniques of extreme solar events such as solar flares and CMEs, are based on a regions classification and the historical likelihood of these events originating from such regions. Each classification technique attempts to characterise the complexity of active regions into sub-groups. Much work has been done to couple these classifications with physical parameters (area, total magnetic field, ...) to increase the accuracy of the historical prediction methods (Qahwaji & Colak, 2007). However, given that 85% of active regions do not flare these methods require increased accuracy.

Figure 1.7 shows the evolution of active regions on the surface of the Sun. As can be

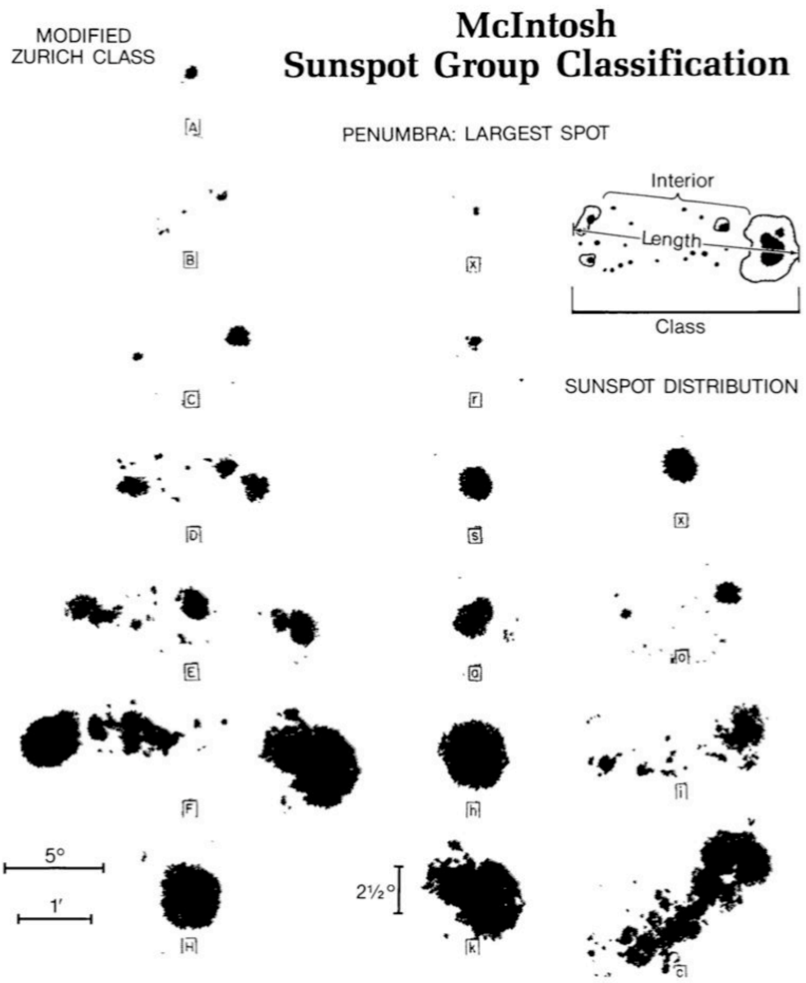

Figure 1.6: The three component McIntosh classification system, with examples of each category.

seen the number and position of active regions follows an 11-year cycle. Active regions emerge at higher latitudes and this emergence gradually migrates towards the equator during the 11-year cycle. Another feature of active regions is the difference in polarity of the leading spot between the northern and southern hemisphere. As one cycle draws to a close and the new one begins the polarity of the leading spot in both hemispheres is observed to flip. As such, the 11-year cycle is in fact periodic over 22-years.

An additional feature of the 11-year cycle is the field strength of the polar magnetic

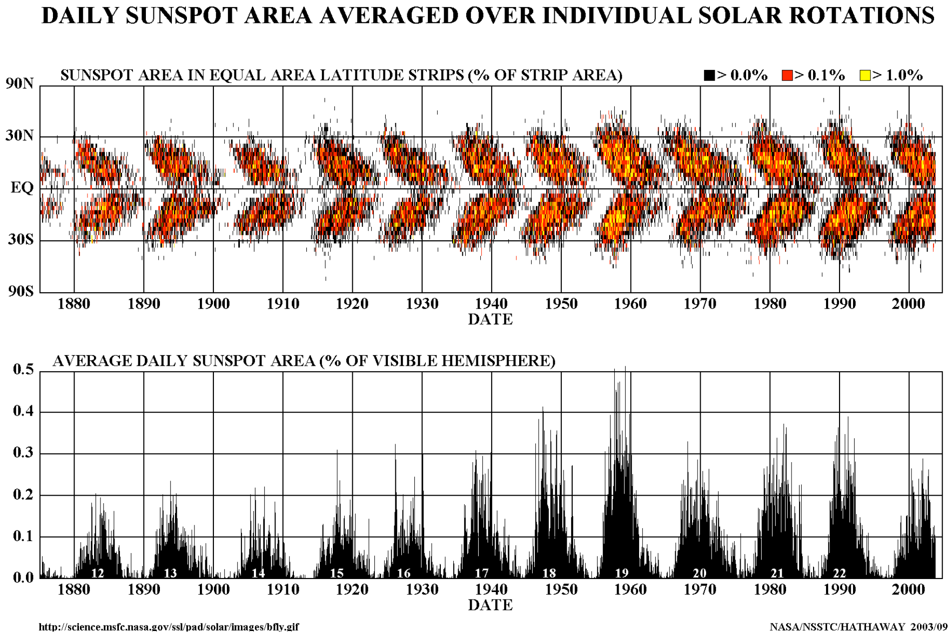

Figure 1.7: This diagram shows the abundance of sunpots at different solar latitudes as a function of time. The shape of the pattern gives rise to the name butterfly diagram. (http://solarscience.msfc.nasa.gov/SunspotCycle.shtml).

field. The strength of the polar magnetic field is observed to mirror the number of sunspots. When the sunspot cycle is at its maximum the polar field is at its minimum and vice versa. Additionally, the polarity of the leading spot in active regions are opposite to the polarity at the pole in each hemisphere. It is thought that the decaying elements of active region magnetic fields migrate along the meridional lines with the polarity of the leading spot heading to the pole and the opposite polarity to the equator. It is this process that is thought to reduce the strength and eventually flip the polarity of the polar field over the course of the 11-year sunspot cycle.

From the mid 17th to early 18th century there were no notable sunspots on the solar surface. The cause of this is still unknown but it's effect is known as the Maunder Minimum. This reduction in the number of sunspots is associated with a climatic event known as the *little ice age*. During this period rivers at lower latitudes that were normally ice free, froze and snow fields remained all year round. The analysis of ice cores taken from the poles indicates that these minima in solar activity are common. As such, the relation between solar activity and the terrestrial climate is still ongoing.

The process by which sunspots are formed was already shown in Figure 1.2. Shearing between the solid-like radiative zone and the differentially rotating convective zone causes a winding-up of the global magnetic dipole field of the Sun into a toroidal (east-west) field. The continuous shearing of the magnetic field eventually cause a build-up of magnetic field in the azimuthal direction. The magnetic pressure associated with these azimuthal field lines ($B^2/8\pi$) forces out the infused plasma in order to maintain a pressure balance with the surrounding plasma (p_0):

$$p_i + \frac{B^2}{8\pi} = p_0. \tag{1.4}$$

This loss of plasma gives rise to a buoyancy force within the field-lines, causing them to rise through the turbulent convective zone (Abbett & Fisher, 2003). During their rise, these flux tubes interact with the convective flows and develop into twisted and fragmented Ω-shaped structures which emerge through the Sun's surface (Figure 1.8). As the solar cycle reaches its end these field-lines approach the equator where it is thought that through a combination of flux-cancellation and convective flows the global dipole is restored.

As magnetic flux emerges through the photosphere, the physical constraints at the surface force the flux tubes to spread out, increasing in size and volume. As the magnetic flux tubes expand and rise into the solar atmosphere they interact with the existing magnetic flux. A combination of magnetic flux emergence and turbulent footpoint motions causes a build-up in the amount of stress and strain along magnetic field lines in the corona. As such, the magnetic fields on the Sun are thought to be responsible for the transfer of energy from the turbulent convective zone into the corona.

The shearing and twisting of magnetic field lines pushes the coronal magnetic field

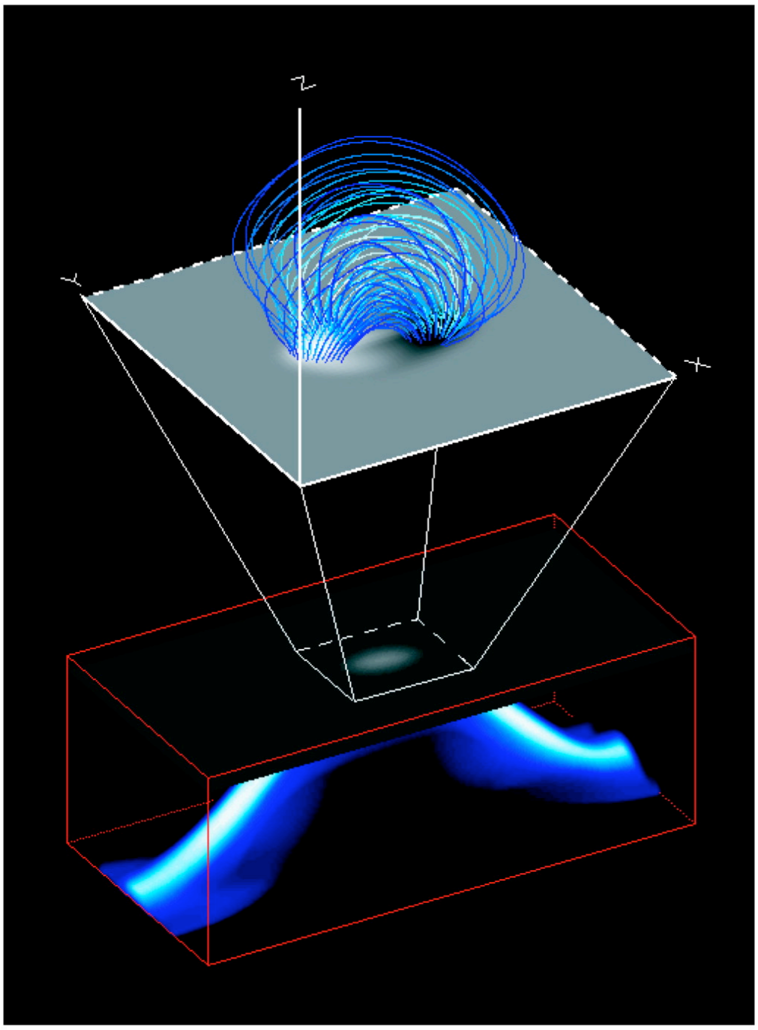

Figure 1.8: Snapshot of an emerging Ω-shaped flux tube (Abbett & Fisher, 2003).

from a stable configuration to an unstable state. The difference in energy between this potential-like state and the strained state is know as free-energy. Upon reaching an unknown critical level the system will undergo self re-organisation to a preferred stable state. Active regions are thought to achieve this through a series of topological changes, known as magnetic reconnection (Aschwanden, 2005). Magnetic reconnection allows for the conversion of the stored magnetic energy. The released energy heats and expands the coronal plasma, producing high energy X-rays and bright, intense loop structure (solar flares). Under certain conditions the reconfiguration of magnetic field lines in the solar corona can result in the ejection of material into interplanetary space as coronal mass ejections (CMEs).

The launch of the *Solar and Heliospheric Observatory* (*SOHO*) in 1995 marked a milestone in the study of active regions and extreme solar events. *SOHO*'s LOS observations of the photospheric magnetic field of active regions have a cadence of 96 minutes and a resolution of 2". Their availability coupled with the other instruments on *SOHO* have expanded our understanding of the structure and evolution of active regions. For the first time *SOHO* offered modellers data of the necessary resolution and cadence which assisted their predictions of extreme solar events. Authors have studied the mathematical properties of solar magnetogram data in order to detect precursors to solar events using a variety of methods (Abramenko, 2005b; Georgoulis, 2008; McAteer *et al.*, 2005a). Numerous potential field extrapolation techniques have been developed to model the coronal field using *SOHO* LOS observations as their boundary conditions. The potential field source surface (PFSS) is one such model and can be used to identify the global structure of the coronal field over a solar rotation. The PFSS method can also be used to model the evolution of coronal holes and the structure of the solar dipole neutral line (Wang & Sheeley, 1992).

Recent advances in ground based observations and the launch of *Hinode* have given modellers the opportunity to study vector magnetogram observations of active regions, although with limited field of view and cadence. The ever increasing resolution of vector magnetogram data allows for the use of more advanced methods that more accurately model the coronal field of active regions. Non-linear force-free (NLFF) extrapolation methods are more advanced and allow the structure of active regions to be modelled in greater detail (Metcalf *et al.*, 2008). Local correlation tracking methods have been developed to extract velocity information from LOS and vector magnetogram data sets (Welsch *et al.*, 2007). These methods have been tested and shown to accurately recover the velocity field of simulated active regions. Time series magnetogram data coupled with velocity information can be used to run magnetohydrodynamic (MHD) models of solar active regions. Both MHD and NLFF methods can be used to calculate the helicity of active regions. Helicity is a conserved quantity in the magnetic fields of active regions. As such, it can only be injected into or ejected from active regions. Changes in the helicity of active regions provided insight into the build-up of twist and the release of CMEs and other eruptions in the corona.

The *Solar TErrestrial RElations Observatory* (*STEREO*) is a twin spacecraft mission, one spacecraft orbits the Sun ahead and the other behind the Earth. *STEREO* allows the three dimensional structure of the solar corona to be studied (Aschwanden *et al.*, 2008b). Additionally, as the reconstruction methods are independent of magnetic field observations they may provide a check on extrapolation methods (Aschwanden *et al.*, 2009). These advanced methods allow a more detailed understanding of the formation and evolution of active regions.

While these instruments and observations have furthered our understanding of active regions a lot is still left unanswered. The precise mechanisms by which active regions produce solar flares and CMEs is still unknown but it thought to be some form of magnetic reconnection. While some mathematical methods have been shown to be sensitive to changes in the structure of active regions, none have been shown with sufficient certainty to detect changes indicative of solar flares or CMEs. Additionally, current extrapolation methods are restricted to single observations and as such, cannot provide detail into the evolution of active regions.

1.3 Solar Flare Theory

There are two major types of energy release on the Sun, namely solar flares and CMEs. Solar flares are sudden, rapid and intense variations in brightness (Gordon Holman,

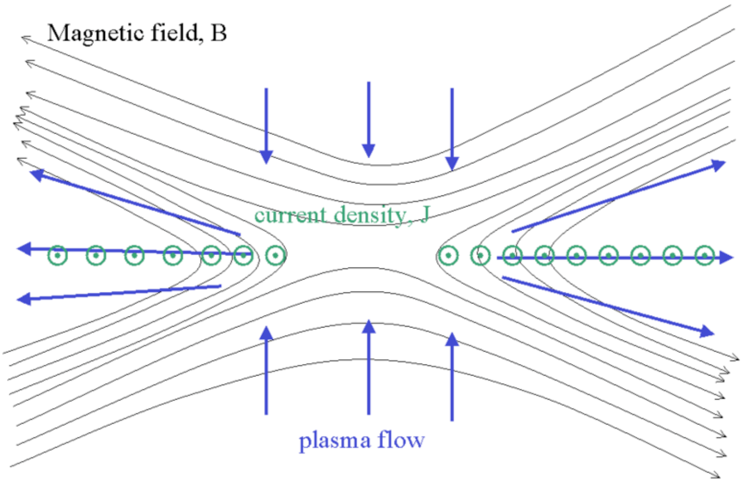

Figure 1.9: 2D model of a magnetic reconnection process. Two oppositely directed magnetic flux systems are driven together by external forces. A diffusion region forms at the boundary ($\mathbf{B} = \mathbf{0}$), creating horizontal outflows (Aschwanden 2005,pg. 409).

1990), which usually originate from large concentrations of magnetic fields on the Solar surface. Large gradients within the magnetic fields of sunspot groups can cause magnetic reconnection in the solar corona (Gallagher *et al.*, 2002). These reconnections heat and accelerate the surrounding plasma. Magnetic reconnection is believed to be the main driver for solar flares and CMEs.

Theoretical models for magnetic reconnection provide an insight into the likely processes involved in the release of magnetic free energy. The driving force of all magnetic reconnection models is the convergence of two oppositely directed magnetic flux systems, as outlined in Figure 1.9. Therefore, the magnetic field across the boundary is zero. In this region of strong gradients the frozen-in condition of the corona breaks down and the plasma is able to diffuse across the magnetic field lines. Strong vertical inflows into the diffusion zone create horizontal outflows. As plasma is ejected horizontally from the diffusion zone, it joins newly created field-lines of a different connectivity and the frozen in-condition is restored. The newly created field-lines are highly pointed.

The curvature of these new field-lines creates a magnetic restoring force. It is this sling shot effect which converts the magnetic energy to kinetic energy (Aschwanden, 2005; Priest & Forbes, 2000).

The two main MHD theories for magnetic reconnection are Sweet-Parker and Petschek. The Sweet-Parker model assumes that the diffusion zone is much longer than it is wide (Parker, 1957; Sweet, 1958). As the problem is essentially a boundary layer problem the reconnection rate can be estimated. According to the Sweet-Parker theory, this boundary layer analysis results in the release of energy over a period of time several orders of magnitude larger than that observed on the Sun (Kulsrud, 2001). Petschek (1964) developed a modification of the Sweet-Parker topology to increase the reconnection rate. By shortening the length of the diffusion region significantly, a very rapid reconnection rate can be achieved. A by-product of the shorter diffusion region is the creation of slow mode shocks that accelerate the horizontal plasma flows. The controversy over which theory is correct is ongoing, however recent computational models have favoured the Sweet-Parker theory (Biskamp, 1986).

1.4 Space Weather

Solar activity can have a direct influence on the Earth. The stream of high energy particles from the Sun, is known as the solar wind. It constantly buffers the Earth's magnetic field and atmosphere. Luckily, the Earth's atmosphere and magnetic field defect or absorb most of the harmful radiation from the Sun. Figure 1.10 shows the protective umbrella of the Earth's magnetic field. Extreme solar events such as solar flares and CMEs can reduce the stand-off distance of the Earth's magnetic field. This reduction in the stand-off distance between the Earth and the stream of particles from the Sun allows radiation to reach further into the atmosphere. These events can be harmful to space based electronics and human explorations.

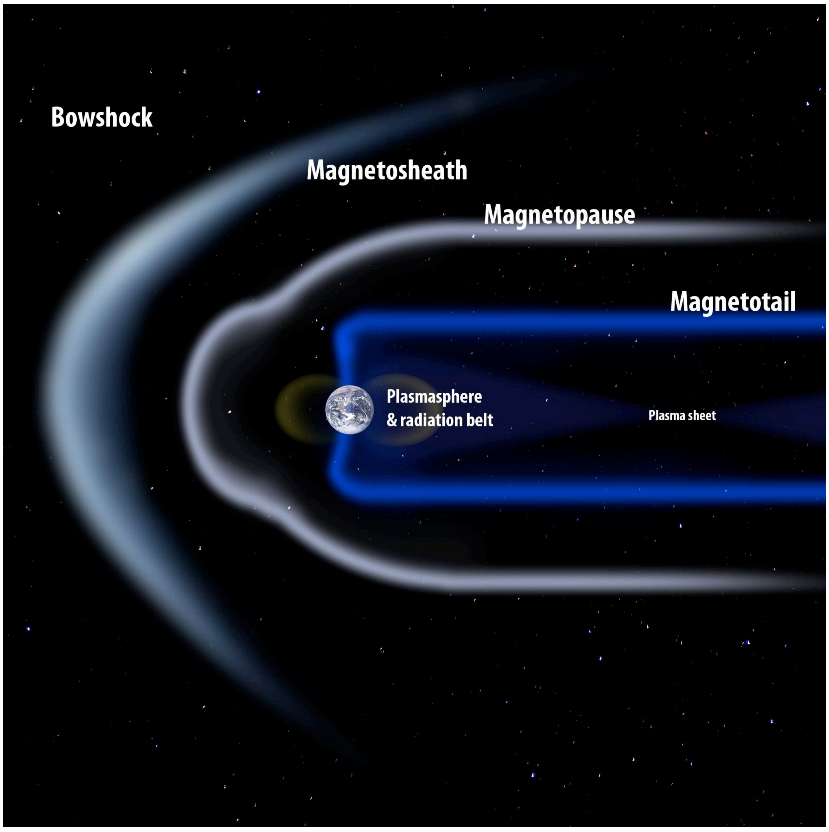

Figure 1.10: Artistic rendering of the Earth's Magnetopause, shown here in the magnetosphere between the magnetosheath and the magnetotail (`http://en.wikipedia.org/wiki/Magnetopause`).

Numerous adverse effects on technology have been associated with fluctuations in solar activity (Jansen *et al.*, 2000). CMEs represent a particular danger to satellites as they are held together by strong magnetic fields and carry a large voltage difference. Solar flares are the sudden release of high energy particles from the Sun. They emit a stream of high energy particles into the solar wind and are a radiation hazard to spacecraft and astronauts. Their associated X-rays increase the ionisation of the upper atmosphere of the Earth. They cause an interference in short wave radio communications and increase the drag of low orbit satellites. These effects have real term economic impact on the global economy. Examples include, the diversion of polar flights, the degradation of GPS positioning, and the shortening of satellite missions.

1.5 Thesis Outline

The work presented in this thesis strives to understand and predict the release of energy in solar flares using a number of mathematical methods to characterise and model the changing properties of the photospheric and coronal magnetic fields. Descriptions of the instruments, their associated data products, and analysis techniques are outlined in Chapter 2. A detailed description of the mathematical methods and theories used and their interpretations are given in Chapter 3 and Chapter 4.

Solar flares have often been associated with active regions that can be best described as being *big, bad, and ugly.* In an attempt to accurately characterise *big, bad, and ugly* McAteer *et al.* (2005a) undertook a large statistical study of active region fractal properties and related them to flaring. A result of this study was that a fractal dimension of $D > 1.2$ was a necessary but not sufficient condition for flaring. As an expansion of this idea, multifractal analysis was applied to a sample of active regions and is presented in Chapter 5. Following the results of this work, a much improved and accurate wavelet based fractal and multifractal analysis package the *wavelet transform modulus maximum method* (WTMM), was applied to the study of solar magnetic fields. As shown in Chapter 6, the analysis of solar active regions using the WTMM method highlighted the need for the segmentation of active region magnetic field information from that of the surrounding quiet sun. The introduction of the segmentation procedure increased the accuracy and reliability of the WTMM method. The returned fractal properties of the WTMM method reinforced the power of fractal properties to predict conditions favourable to flaring in active regions. Given that solar flares originate in the corona a extrapolation method was developed to examine the 3D structure of the corona, and is presented in Chapter7. In Chapter 8 a summary of this thesis is presented and a discussion of the major points and outstanding questions is given.

2

Instrumentation

In the course of this thesis numerous data products from space-based observatories were used to analyse solar active regions. A short description of *SOHO*, *TRACE*, and *STEREO* follows. The combined coverage of these satellites provide a complete picture of the changing structure of active regions.

2.1 SOHO

For the purpose of this thesis data from the Solar and Heliospheric Observatory (SOHO) was used to observe the Sun. SOHO is a joint European Space Agency (ESA) and National Aeronautics and Space Administration (NASA) mission. It was launched on 2 December 1995 and was designed to study the interior structure of the Sun and the solar atmosphere (Domingo *et al.*, 1995). It is located in a stable orbit at the inner Lagrangian between the Earth and the Sun some 1.5×10^6 km from the Earth. This is a point of equilibrium where it remains at rest relative to the Sun and Earth. Here it has an uninterrupted view of the Sun, except for a brief period in 1998 when contact was lost with the spacecraft due to the effects of space weather.

The SOHO satellite has twelve instruments on-board which are roughly divided

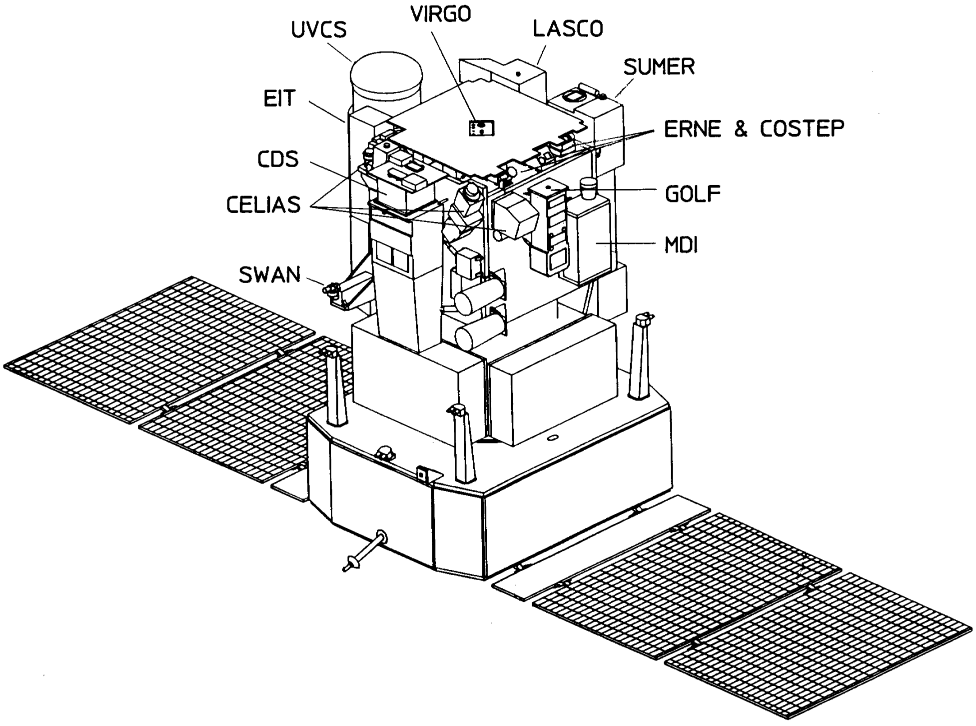

Figure 2.1: Payload diagram of the SOHO satellite (courtesy of *SOHO ESA/NASA*).

into three areas of research. Three helioseismological experiments have been providing highly accurate measurements of solar oscillations. Three more instruments investigate the solar wind around SOHO, measuring mass, ionic charge states, densities, energies and velocities of the low and high speed solar wind. The other six instruments include telescopes and spectrometers which provide data on the dynamics of the solar atmosphere in and above the chromosphere. A schematic diagram of the SOHO satellite and instruments is shown in Fig 2.1. During the course of this thesis work data from the Michelson Doppler Imager (MDI; Scherrer *et al.* 1995) instrument and the Extreme-ultraviolet Imaging Telescope (EIT) were used to analyse the magnetic photosphere and structure of the solar atmosphere.

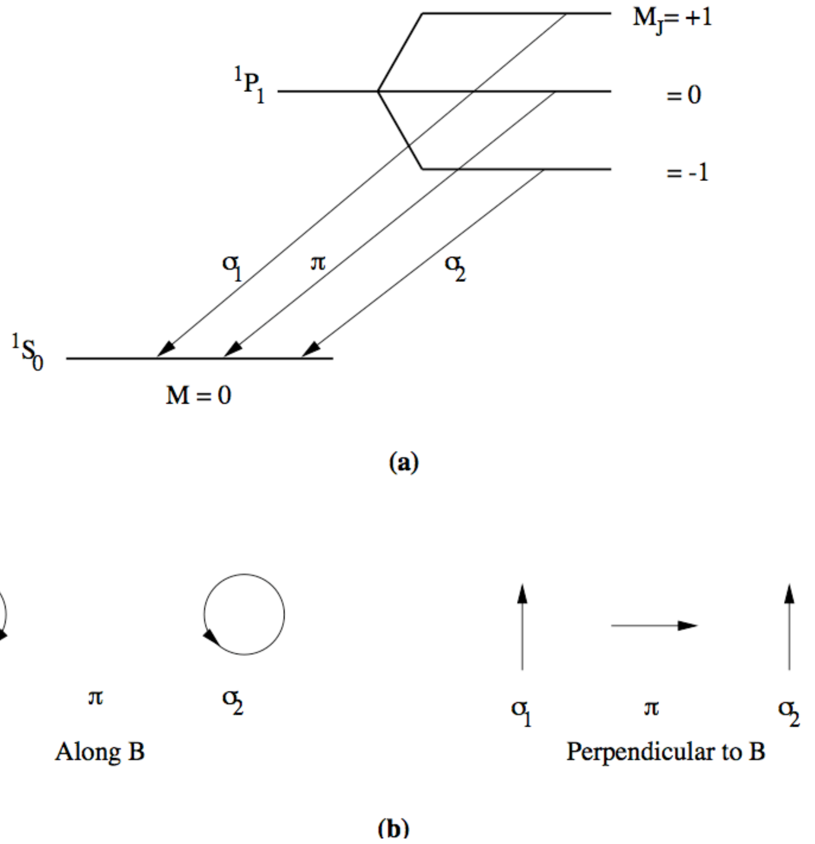

Figure 2.2: The Zeeman effect. (a) Structure of levels giving the simplest Zeeman triplet. (b) Polarisation of the Zeeman components viewed parallel and perpendicular to the magnetic field. Along the magnetic field, we can only see the σ_1 and σ_2 components, with the opposite circular polarisations while perpendicular to the field we see the π component polarised parallel to the field and the σ components linearly polarised in the perpendicular direction (Gallagher, 2000).

2.1.1 The Michelson Doppler Imager

MDI consist of a 1024 × 1024 CCD camera, providing magnetogram images of the photosphere with a cadence of 90 minutes. To date, MDI has produced about ninety million images, of these about fifteen million raw data images were sent to ground based stations.

MDI works by filtering the light from the Sun through a series of narrowing filters. The final filtering stage is a pair of tunable Michelson interferometers, enabling MDI to record filtergrams of the Sun. These filtergrams are used to calculate the velocity

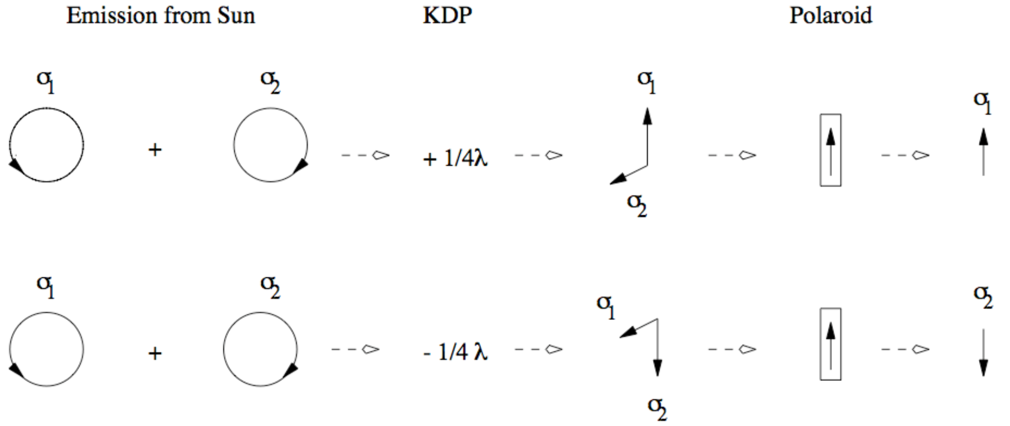

Figure 2.3: The basic operation of a Babcock type magnetograph (Babcock, 1953). The potassium dihydrogen phosphate (KDP) electrooptic cell converts the circularly polarised light into plane polarised light shifter by 90 according to the sign of the KDP voltage. These components are then selected by the Polaroid (Gallagher, 2000).

and continuum intensity with a resolution of 4" over the whole disk. In another mode MDI can use 10 filtergrams on a smaller region to gain a resolution of 1.25".

MDI utilises the principles of the Zeeman effect to transfer the filtergrams into magnetograms. The Zeeman effect is the splitting of lines in a spectrum when the source of the spectrum is exposed to a magnetic field. In the normal Zeeman effect a single line is split into three if the field is perpendicular to the light path or two lines if the field is parallel to the light path.

The energy levels are then split according to the quantum number M_j, which is the projection of the total angular momentum J along the direction of the magnetic fields. An example of the normal zeeman effect is the transition from $^1P \rightarrow ^1S$ is given in Figure 2.2. In the absence of a magnetic field the energy levels of the atom remain unperturbed and a single spectral line is observed. When there is a magnetic field we find that the energy levels of the ^1P level split into three states given by $M_j = -1, 0, +1$. The ^1S level remains unaffected as it has no orbital or spin angular momentum. The unshifted line is called the π component and is only observable perpendicular to the magnetic field. The two shifted components are called σ_1 and σ_2 and are shifted to the right and left of the unperturbed line by:

$$\Delta\lambda_H = 4.7 \times 10^{-13} g \lambda^2 H, \tag{2.1}$$

where H is the field strength in Gauss and g is the Landé factor of the spectral line, and λ_H and $\Delta\lambda_H$ are in Å units.

For weak magnetic fields the splitting of spectral lines can be impossible to detect even with high resolution spectrographs. The polarisation properties of the Zeeman components are then used to measure the magnetic field strength. The σ_1 and σ_2 components are shifted in wavelength and oppositely circularly polarised. Therefore choosing the right or left polarised light entering the telescope corresponds to the σ_1 and σ_2 components.

In the standard Babcock design, Figure 2.3, the σ components are separated using an electrooptic crystal (Babcock, 1953). Passing the correct voltage through the crystal produces a retardation of $\lambda/4$ which converts the circularly polarised σ components into two linearly polarised beams at right angles to each other. A linear Polaroid then allows only one beam to pass through. A retardation in the opposite sense can be achieved by applying an opposite voltage to the crystal, thus allowing both σ components to be calculated. The difference in intensity of the signal in each of these states is then used to infer the longitudinal magnetic field strength.

2.1.2 The Extreme-ultraviolet Imaging Telescope

Figure 2.4, shows a schematic drawing of EIT. EIT provides full-disk images of the solar transition region and inner corona up to 1.5 $R_\odot$ above the solar limb using normal incidence multilayer optics and an EUV sensitive 1024 × 1024 CCD camera. A Ritchey-Chretien design telescope, EIT images in four narrow passbands with a field of view of 45” square and a spatial resolution of 2.6”. The four quadrants of both the primary and

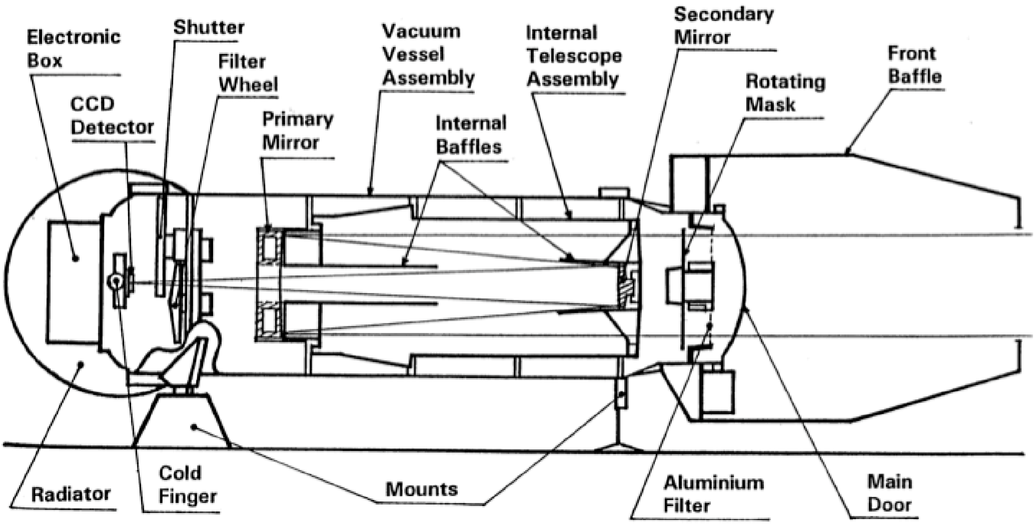

Figure 2.4: Schematic of the EIT indicating its major subsystems (Delaboudinière *et al.*, 1995).

secondary mirror are coated in four different multilayers (Table 2.1). The passbands are selected through interference effects arising in the multilayer coatings. A rotating mask allows a single multilayer-coated quadrant of the telescope to be illuminated by the Sun at any given time. The images from each quadrant are then focused onto a back-illuminated CCD which is cooled to about -80 C.

Table 2.1 shows the four passbands available from EIT observations. The 304 Å band is centred on the He II emission line which is formed in the upper chromosphere at a temperature of 8×10^4 K. The other lines are centred on the Fe IX/X (171 Å), Fe XII (195 Å) and Fe XV (284 Å) emission lines, and are all designed to study the structure of the solar corona in the 1.3×10^6 K to 2×10^6 K range. EIT data must first be properly calibrated using a variety of techniques, all of which are available in the EIT branch of the IDL based SOLARSOFT analysis tree. For the purpose of this work, data from 171 Å observations was used. The 171 Å passband has fewer contributions from the diffuse higher temperature emission lines compared to the 195 Å passband (Phillips *et al.*, 2005).

Table 2.1: Details of the EIT bandpasses, temperatures and observables.

Wavelength	Ion	Peak Temperature	Observational Objective
304 Å	He II	8.0×10^4 K	chromospheric network, coronal holes
171 Å	Fe IX/X	1.3×10^6 K	corona/transition region boundary
195 Å	Fe XII	1.6×10^6 K	quiet corona outside coronal holes
284 Å	Fe XV	2.0×10^6 K	active regions

2.2 STEREO

STEREO is a NASA mission that was launched on the 25 October 2006 aboard a single Boeing Delta II rocket from Cape Canaveral Air Force Station. The primary objective of the STEREO mission is to study the properties and causes of CMEs. *STEREO* comprises of two identical spacecraft that orbit the Sun, one ahead of the Earth and the other behind. The twin spacecraft offer a unique view of the Sun and allow, for the first time, a three dimensional view of the Sun. For the purpose of this thesis EUV observations from the *Extreme UltraViolet Imager* (EUVI; Wuelser *et al.* 2004) on-board *STEREO* were used to constrain the choice of α in LFF extrapolations. The twin views of *EUVI* enabled a double check on the scientific results of the magnetic field extrapolations.

2.2.1 Extreme UltraViolet Imager

EUVI was developed at Lockheed Martin Solar and Astrophysics Lab and is similar in design to *EIT*. EUVI observes the solar atmosphere in four narrow passbands with a field of view of 45” square and a spatial resolution of 2.6”. The four quadrants of both the primary and secondary mirror are coated in four different multilayers (Table 2.2). The passbands are selected through interference effects arising in the multilayer coat-

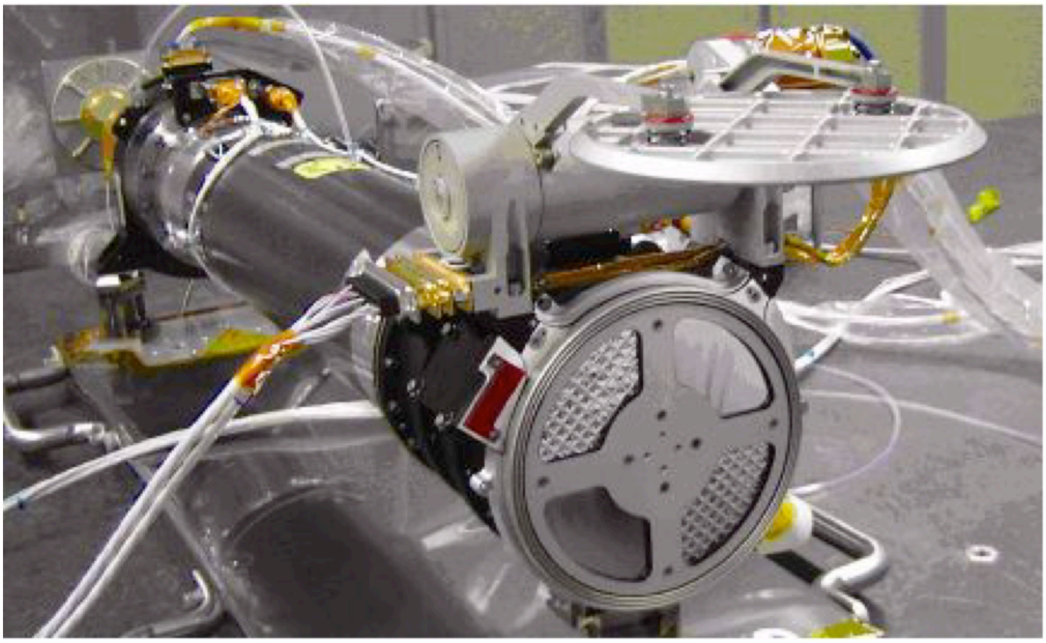

Figure 2.5: The *EUVI* telescope prior to integration into the *SECCHI* suite (Wuelser *et al.*, 2004).

ings. A rotating mask allows a single multilayer-coated quadrant of the telescope to be illuminated by the Sun at any given time. The images from each quadrant are then focused onto a back-illuminated CCD which is cooled to about -80 C.

It is a normal-incidence telescope with thin metal filters, multilayer coated mirrors and a back illuminated CCD detector. Figure 2.5 shows one of the *EUVI* telescopes during set-up. The four *EUVI* passbands are the same as those in *EIT* and their properties are outlined in Table 2.2.

While similar in design to EIT, the twin spacecraft of *STEREO* allows for the 3D reconstruction of coronal loops as observed by EUVI. Aschwanden *et al.* (2008b) first outlined a method by which the 3D structure of coronal loops could be recovered from EUVI observations. As a continuation of that initial study Aschwanden *et al.* (2008a, 2009), examined the temperature and electron density along observed coronal loops.

Table 2.2: Properties of the *EUVI* multilayer coating.

Principal emission lines	Centre wavelength
Fe IX, Fe X	172 Å
Fe XII, Fe XIV	194 Å
Fe XV	284 Å
He II	304Å

2.3 TRACE

Transition Region and Coronal Explorer (TRACE; Handy *et al.* 1999) is a space-borne solar telescope which observes emissions from solar plasma in three EUV wavelengths and several UV wavelengths, covering temperatures from 6,000 K to 10MK (Handy *et al.*, 1999). It orbits in a polar trajectory roughly following the day-night terminator. It has uninterrupted solar viewing for nine months of the year. Normal incidence multilayer optics allow TRACE to observe UV and EUV emissions from the photosphere to the corona. A schematic diagram of the satellite is shown in figure 2.6.

Pointing is achieved through a guiding telescope on the top of the satellite and limb finding algorithm. Wavelength selection is determined by a quadrant selector located just behind the entrance filter chamber, similar in design to EIT and EUVI. The bandpass is defined by multilayer coatings on the primary and secondary mirrors. Focused images with a resolution of 1" are projected onto a phosphor-coated CCD sensitive to UV and EUV wavelengths.

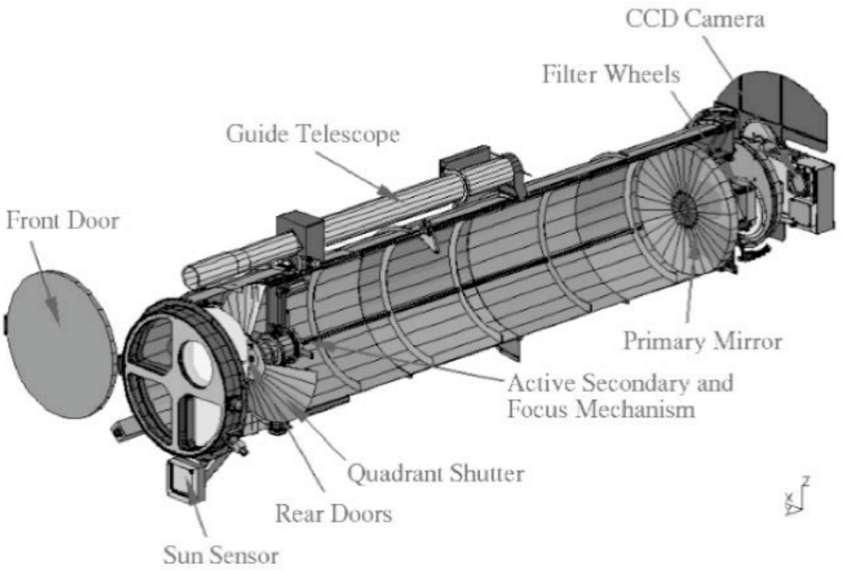

Figure 2.6: An isometric diagram of the TRACE telescope (Handy *et al.*, 1999).

3

Magnetohydrodynamic Theory

In this chapter, we outline the basic equation and theory behind the structure and evolution of plasma in the solar atmosphere. The set of equations which govern the magnetised plasma on the Sun are known as magnetohydrodynamics (MHD) and the foundations of MHD theory is outlined. Additionally, the theory of turbulence is examined and shown to apply to all systems on the Sun across a range of spatial scales. Finally the method used to extrapolate the coronal magnetic field from photospheric observations is outlined.

3.1 Introduction

The evolution and structure of the solar atmosphere is governed by the interaction of the solar plasma with the magnetic field (Osterbrock, 1961). These interactions are governed by a set of equations known collectively as magnetohydrodynamics (MHD). They are a combination of the equations of electric and magnetic fields and those of fluid dynamics. This chapter contains a brief summary of these equations and the approximations used to model the changing structure of the solar atmosphere as part of this study.

3.2 Fundamental Equations

The starting point of any study into the interaction of magnetic fields in a dynamic system are Maxwell's equations.

3.2.1 Maxwell's Equations

Maxwell's equations govern the inter-relationship of the magnetic and electric fields in a system. They are given by:

$$\begin{aligned}\nabla \times \mathbf{B} &= \mu \mathbf{j} + \frac{1}{c^2}\frac{\partial \mathbf{E}}{\partial t} &(3.1)\\ \nabla \cdot \mathbf{B} &= 0 &(3.2)\\ \frac{\partial \mathbf{B}}{\partial t} &= -\nabla \times \mathbf{E} &(3.3)\\ \nabla \cdot \mathbf{E} &= \frac{1}{\epsilon}\rho, &(3.4)\end{aligned}$$

where $\mathbf{B}$ is the magnetic field, $\mathbf{E}$ is the electric field, $\mathbf{j}$ the current density, μ the magnetic permeability in a vacuum, ρ the charge density, ϵ the permittivity of free space and c the speed of light in a vacuum.

Assuming that the typical plasma velocity is much less than the speed of light c, we can neglect the second term on the right hand side of Equation 3.1. Ampère's Law then becomes:

$$\nabla \times \mathbf{B} = \mu \mathbf{j} \tag{3.5}$$

In addition to the four Maxwell equation we have Ohm's Law:

$$\mathbf{j} = \sigma(\mathbf{E} + \mathbf{v} \times \mathbf{B}), \tag{3.6}$$

where σ is the electrical conductivity and $\mathbf{v}$ is the plasma velocity. Ohm's law couples the plasma velocity to Maxwell's equations.

3.2.2 Fluid Equations

The mass continuity equation states that plasma is neither created or destroyed as such:

$$\frac{\partial\rho}{\partial t} + \nabla \cdot \rho\mathbf{v} = 0, \tag{3.7}$$

where ρ is the plasma density and $\mathbf{v}$ the velocity. If the plasma is incompressible ($D\rho/Dt = 0$), then, with the use of vector identities, the mass continuity equation (Equation 3.7) reduces to:

$$\nabla \cdot \mathbf{v} = 0. \tag{3.8}$$

The equation of motion, $\mathbf{F} = m\mathbf{a}$, is given by:

$$\rho\frac{D\mathbf{v}}{Dt} = -\nabla P + \mathbf{F}, \tag{3.9}$$

where P is the pressure and $\mathbf{F}$ the external forces. D/Dt is the convective time derivative:

$$\frac{D}{Dt} = \frac{\partial}{\partial t} + \mathbf{v} \cdot \nabla \tag{3.10}$$

The external forces that govern our system are the magnetic (Lorentz), the gas pressure and the gravitational forces. The equation of motion is then:

$$\rho\frac{D\mathbf{v}}{Dt} = -\nabla P + \mathbf{j} \times \mathbf{B} + \rho\mathbf{g}. \tag{3.11}$$

3.2.3 The Induction Equation

Rearranging Ohm's Law (Equation 3.6) and Ampère's Law (Equation 3.5) gives:

$$\mathbf{E} = -\mathbf{v} \times \mathbf{B} + \frac{1}{\mu\sigma}\nabla \times \mathbf{B}, \tag{3.12}$$

This can be used to remove **E** from Faraday's law (Equation 3.3) to give the Induction Equation:

$$\begin{aligned} \frac{\partial \mathbf{B}}{\partial t} &= -\nabla \times \mathbf{E}, & (3.13) \\ &= -\nabla \times (-\mathbf{v} \times \mathbf{B} + \frac{1}{\mu\sigma}\nabla \times \mathbf{B}), & (3.14) \\ &= \nabla \times (\mathbf{v} \times \mathbf{B}) + \eta\nabla^2\mathbf{B}, & (3.15) \end{aligned}$$

where $\eta = 1/\mu\sigma$ is the magnetic diffusivity.

3.2.4 The Magnetic Reynolds Number

The magnetic Reynolds number is defined as the ratio of the advection and diffusion terms in the induction equation:

$$\begin{aligned} R_m &= \frac{\nabla \times (\mathbf{v} \times \mathbf{B})}{\eta\nabla^2 B} & (3.16) \\ &= \frac{v_0 B/l_0}{\eta B/l_0^2} & (3.17) \\ &= \frac{l_0 v_0}{\eta} & (3.18) \end{aligned}$$

where v_0 is a typical velocity and l_0 a typical length scale. As R_m is a dimensionless quantity, it provides us with a means to simplify the induction equation. The magnetic Reynolds number is a measure of the relations between the flow and the magnetic field. For a sunspot the typical parameters are $l_0 = 10^7$m, $v_0 = 10^3$ms^{-1} and $\eta = 10^3$m^{2}s^{-1}, therefore the magnetic Reynolds is $R_m = 10^7 10^3/10^3 = 10^7 \gg 1$.

If $R_m \gg 1$ then the induction equation can be simplified to become:

$$\frac{\partial \mathbf{B}}{\partial t} = \nabla \times (\mathbf{v} \times \mathbf{B}). \tag{3.19}$$

As such, the coupling of the flow and the magnetic field is strong. However if $R_m \ll 1$

then the induction equation becomes:

$$\frac{\partial \mathbf{B}}{\partial t} = \eta \nabla^2 \mathbf{B}. \tag{3.20}$$

In this case any irregularities in the magnetic field will diffuse away on the time scale of $\tau_{diffusion} \approx l_0^2/\eta$. Typically values for a sunspot give a diffusion time of 10^{11}s. Therefore diffusion cannot be the main method of particle motion in sunspots, unless large gradients are present or processes occur over small length scales.

3.2.5 Frozen Flux Theorem

Knowing $\nabla \cdot \mathbf{B} = 0$, the total time derivative of the magnetic flux through a surface that moves with velocity $\mathbf{u}$ is given by (Goossens, 2004):

$$\frac{d}{dt} \int_S \mathbf{B} \cdot \mathbf{n} dS = \int (\frac{\partial \mathbf{B}}{\partial t} - \nabla \times (\mathbf{u} \times \mathbf{B})) \tag{3.21}$$

As already mentioned a consequence of the large magnetic Reynolds numbers found on the Sun is $\partial \mathbf{B}/\partial t - \eta \nabla^2 \mathbf{B} = 0$. As such, assuming the surface S moves with the plasma, $\mathbf{u} = \mathbf{v}$, the total time derivative of the magnetic flux is:

$$\frac{d}{dt} \int_S \mathbf{B} \cdot \mathbf{n} dS = 0 \tag{3.22}$$

As a result, the magnetic flux that moves through a plasma is conserved, or the magnetic field and plasma are frozen together. This means that motions parallel to the magnetic field have no effect but motions perpendicular to the field carry the flux with it.

An additional consequence of the large magnetic Reynolds numbers on the Sun is the conservation of magnetic helicity:

$$\frac{d}{dt} \int_{V_B} \mathbf{B} \cdot \mathbf{A} dV = 0, \tag{3.23}$$

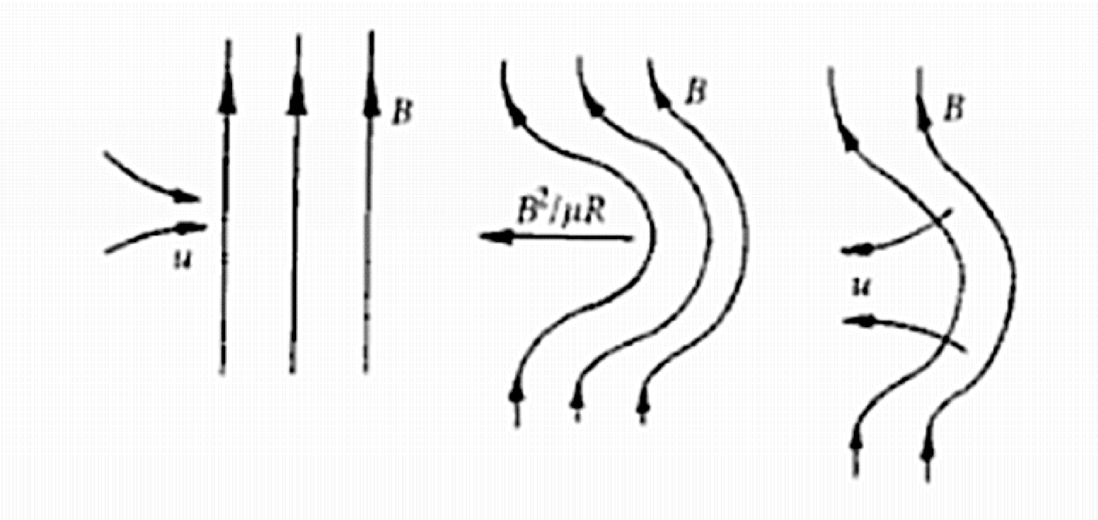

Figure 3.1: Magnetic field lines behave like elastic bands frozen into the fluid (Davidson, 2004).

where V_B is a volume that encloses all the magnetic field, and $\mathbf{A}$ is the vector potential of $\mathbf{B} = \nabla \times \mathbf{A}$ (Davidson, 2004). The proof of Equation 3.23 follows from Equation 3.19 in the form:

$$\frac{\partial \mathbf{A}}{\partial t} = \mathbf{u} \times \mathbf{B} + \nabla \phi. \tag{3.24}$$

As such, the magnetic field is frozen to the plasma and impulsive forces perpendicular to the magnetic field will cause distortions in the magnetic field, see Figure 3.1. The resulting curvature of the field-lines causes a restoring force. The restoring force is known as *Faraday tension* and is a results of the Lorentz force:

$$\mathbf{F} = \mathbf{J} \times \mathbf{B} = (\mathbf{B} \cdot \nabla)[\mathbf{B}/\mu] - \nabla[\mathbf{B}^2/2\mu]. \tag{3.25}$$

The second term on the right hand side is known as the *magnetic pressure*. The restoring force is a result of the first term, which can be rewritten in curvilinear coordinates as:

$$(\mathbf{B} \cdot \nabla)[\mathbf{B}/\mu] = \frac{B}{\mu}\frac{\partial B}{\partial s}\hat{\mathbf{e}}_t - \frac{B^2}{\mu R}\hat{\mathbf{e}}_n, \tag{3.26}$$

where $B = |\mathbf{B}|$, $\hat{\mathbf{e}}_t$ and $\hat{\mathbf{e}}_n$ are the unit vectors tangential and normal to the magnetic field, R is the radius of curvature of the field line and s is a coordinate measured along the field line.

As such, plasma motions that distort the magnetic field are resisted by the magnetic tension force until such a time as the fluid comes to rest. The tension force then moves to restore the field-lines to their original position. However, the inertia of the plasma causes the field-lines to overshoot and the processes continues. This is the basis upon which Alfvn waves move along magnetic field lines.

3.3 Turbulence

Turbulent flows are ubiquitous in nature. Virtually all fluid have an extremely low viscosity and, as will be shown below, this results in turbulent flows. Common themes of turbulence include:

- A randomly fluctuating velocity field in both time and space.
- A wide range of length scales.
- Small perturbations in the initial conditions giving rise to large differences in the velocity field.

In order to understand turbulence it is first important to understand how it is formed. Newton's second law (Equation 3.9) can be written as:

$$\rho \frac{D\mathbf{v}}{Dt} = -\nabla p + \mathbf{F}, \tag{3.27}$$

where $\mathbf{F}$ is all additional forces. Coupled with the continuity equation (Equation 3.7) and assuming we are dealing with an incompressible Newtonian fluids, Newton's second law for viscous fluids can be rewritten as:

$$\rho \frac{D\mathbf{v}}{Dt} = -\nabla p + \mu \nabla^2 \mathbf{v} \tag{3.28}$$

This is known as the Navier-Stokes equation. Expanding the equation as follows:

$$\rho \frac{D\mathbf{v}}{Dt} = \rho \left(\frac{\partial \mathbf{v}}{\partial t} + (\mathbf{v} \cdot \nabla)\mathbf{v} \right) = -\nabla p + \mu \nabla^2 \mathbf{v}, \tag{3.29}$$

$$\frac{\partial \mathbf{v}}{\partial t} + (\mathbf{v} \cdot \nabla)\mathbf{v} = -\frac{1}{\rho}\nabla p + \frac{\mu}{\rho}\nabla^2 \mathbf{v}, \tag{3.30}$$

highlights the non-linear or quadratic nature of the Navier-Stokes equation. The non-linear term $((\mathbf{v} \cdot \nabla)\mathbf{v})$ in the equation is the cause of the resulting chaotic behaviour.

The Navier-Stokes equation can be rewritten in its non-dimensional form as follows:

$$\frac{V^2}{L}\left(\frac{\partial \mathbf{v}'}{\partial t'} + (\mathbf{v}' \cdot \nabla)\mathbf{v}' \right) = -\frac{V^2}{L}\nabla\left(\frac{p'}{\rho'}\right) + \frac{\mu}{\rho'}\frac{V}{L^2\rho}\nabla^2 \mathbf{v}', \tag{3.31}$$

where L is a characteristic length scale, V is a characteristic velocity, ρ is a characteristic density and the characteristic pressure $P = \rho V^2$ and the $'$ variables are dimensionless. The Reynolds number is defined as:

$$R_e = \frac{\rho V L}{\mu} = \frac{VL}{\nu}, \tag{3.32}$$

where $\nu = \mu/\rho$. This allows us to rewrite the Navier-Stokes equation as:

$$\frac{\partial \mathbf{v}}{\partial t} = \nabla\left(\frac{p'}{\rho'}\right) - (\mathbf{v} \cdot \nabla)\mathbf{v} + \frac{1}{R_e}\nabla^2 \mathbf{v}, \tag{3.33}$$

where the $'$ notation has been dropped for ease of reading. As can be seen the Reynolds number relates the inertial forces to the viscous forces.

At low Reynolds numbers the viscous force is large compared to the inertia force. Therefore, small disturbances in the velocity field caused by small roughness or pressure perturbations, will be damped out and not allowed to grow. As the Reynolds numbers increases the viscous forces become less significant and at a critical point small scale perturbations are allowed to grow. At this point the system will experience a transition to a turbulent state where large variations in the velocity field are possible. Figure 3.2 outlines the transition from a low Reynolds number system to one with a high Reynolds number. As the smoke rises the plume accelerates and the local Reynolds number increases. Instabilities set-in at a given Reynolds number and the velocity of the plumes becomes chaotic.

As already mentioned most fluids have extremely low viscosity and the Navier-Stokes equation can be written as:

$$\frac{\partial \mathbf{v}}{\partial t} = \nabla\left(\frac{p'}{\rho'}\right) - (\mathbf{v} \cdot \nabla)\mathbf{v}. \tag{3.34}$$

A characteristic of a turbulent process is the range of scales over which structures exist. It is thought that energy is injected into the system at large length scales (typically the length scale of the mean field). Turbulent process then transfer energy to smaller length scales through some means, most likely the distortion and break-up of eddies or vortices. Eventually a scale is reached at which viscous forces become dominant and the energy is dissipated. Figure 3.3 outlines this cascade of energy in a turbulent system. Hewett *et al.* (2008) used a wavelet based method to study the evolution of such an energy spectrum for active region NOAA 10488. They found evidence for an inverse cascade during the formation of the active region. An inverse cascade is the movement of energy from small scales to large scales. The inverse cascade found by Hewett *et al.* (2008) is most likely due to the initial emergence of small scale magnetic elements within the active region. Over time these elements coalesce and form larger

Figure 3.2: Cigarette smoke as it rises develops turbulent characteristics (photo credit: Cigarette smoke, Pal & Basu).

magnetic elements. As such, energy is transported from small to large scales during the formation of active regions.

Kolmogorov (1941) formulated a theorem which states that:

> When R_e is large, and in the range $\mu \ll k \ll l$, the statistical properties of $[\Delta \mathbf{v}](k)$ have a universal form which is uniquely determined by k and $\epsilon =< 2\mu S_{ij} S_{ij} >$ alone and is given by:

$$< [\Delta \mathbf{v}]^2 >= \beta \epsilon^{2/3} k^{2/3}, \tag{3.35}$$

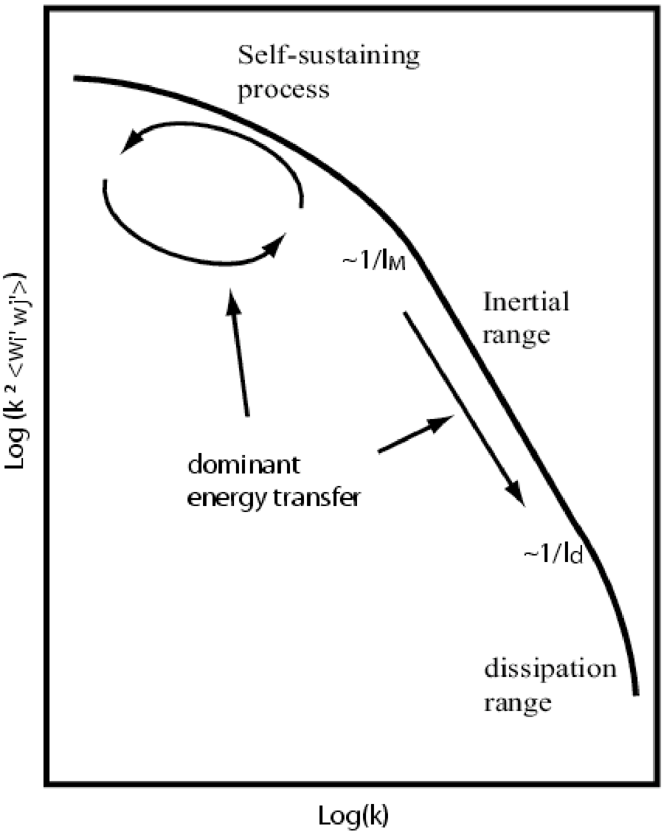

Figure 3.3: Idealised energy spectrum in a turbulent shear flow. Arrows indicate the energy flow. The length-scales l_M and I_d correspond to the top of the inertial range and the top of the dissipation range (Lesur & Longaretti, 2005).

where k is the wave number as shown in Figure 3.3, $\mu = 1/l_M$ is a lower limit and $l = 1/l_d$ an upper limit in k-space. Therefore, a sub-range exists in the inertial dominant part of the spectrum governed by the above equation. It is known as "Kolmogorov's 2/3 law" and is a characteristic of fully developed turbulence.

In the late 1960s Mandelbrot (1974a); Mandelbrot & Van Ness (1968) observed that in infinite cascade models, the energy dissipation generally concentrated on a set of non-integer (fractal) Hausdroff dimensions. This is not surprising when one considers that turbulence is characterised by a cascade of energy across a broad range. The continuous breakup of eddies or vortices from the larger to smaller scales produces a self-similar structure. These self-similar structure are ideally modelled by fractal structures.

In the mid 1980s the fractal formalism was expanded to provide a more complete understanding of the fluctuations of the singular measures found in chaotic systems (Halsey *et al.*, 1986; Parisi & Frisch, 1985). This work founded the theory of multifractals. Multifractals as will be discussed later, have a range of scaling exponents which characterise their structure. Both methods along with other self-similar statistical tools are used extensively to model and characterise turbulent systems.

3.4 3D Extrapolation Methods

Observations of the solar corona show that the field remains stable and essentially static for multiple observations. In this case the magnetohydrostatic solution to the MHD equations can be used. Assuming the magnetic fields are stationary and neglecting flows, $\mathbf{v} = 0$, the equation of motion becomes:

$$0 = -\nabla P + \mathbf{j} \times \mathbf{B} + \rho \mathbf{g}, \tag{3.36}$$

where P is the plasma pressure term, $\mathbf{B}$ the magnetic field, ρ the plasma density and $\mathbf{g}$ the gravitational force. Examining features with length, l_0, less than the gravitational scale height we can neglect the gravitational term. Given that the solar corona is a low β plasma and neglecting velocity variations less than the Alfvn speed, the equation of motion can be reduced to the *force-free approximation* (Aschwanden, 2005; Gary, 2001):

$$\mathbf{j} \times \mathbf{B} = 0, \tag{3.37}$$

where $\mathbf{j}$ is the current density and $\mathbf{B}$ is the magnetic field. The force-free approximation requires that the current must be proportional to the magnetic field:

$$\mathbf{j} = \alpha \mathbf{B}. \tag{3.38}$$

Table 3.1: Possible choices of α

$\alpha =$	0	Potential field
$\alpha =$	constant	Linear force-free field (LFF)
$\alpha =$	constant along each field line	Non-linear force-free field (NLFF)

As such, Equation 3.5 can be rewritten as:

$$\nabla \times \mathbf{B} = \mu \mathbf{j} = \alpha(r)\mathbf{B}. \tag{3.39}$$

The choice of α is not arbitrary. Coupling the vector identity $\nabla \cdot (\nabla \times \mathbf{B})$, with the divergence-free Maxwell equation ($\nabla \cdot \mathbf{B} = 0$) results in:

$$\nabla \cdot (\nabla \times \mathbf{B}) = \nabla \cdot (\alpha \mathbf{B}) = \alpha(\nabla \cdot \mathbf{B}) + \mathbf{B} \cdot \nabla\alpha = \mathbf{B} \cdot \nabla\alpha = 0. \tag{3.40}$$

As such there are three choices of α as outlined in Table 3.1

3.4.1 Non-linear Force-Free Fields

Potential and LFF methods are unable to reconstruct the complex topology of active region cores. Therefore, NLFF methods are required to investigate their changing topology. In the case of NLFF fields, $\alpha = \alpha(\mathbf{r})$, the governing equation is:

$$\nabla \times \mathbf{B} = \alpha(\mathbf{r})\mathbf{B}. \tag{3.41}$$

Calculations of the NLFF field are possible provided all boundary conditions are fully known. Therefore vector magnetogram data is required. While NLFF methods offer the possibility of better accuracy, they require costly computational power.

Taking the curl of the current density, $\mathbf{j} = \alpha\mathbf{B} = \nabla \times \mathbf{B}$ gives:

$$\nabla \times (\nabla \times \mathbf{B}) = \nabla \times \alpha\mathbf{B} = \alpha(\nabla \times \mathbf{B}) + \nabla\alpha \times \mathbf{B} = \alpha^2\mathbf{B} + \nabla\alpha \times \mathbf{B}. \tag{3.42}$$

Additionally, vector identities give:

$$\nabla \times (\nabla \times \mathbf{B}) = \nabla(\nabla \cdot \mathbf{B}) = \nabla^2\mathbf{B}. \tag{3.43}$$

Combining these two expressions for the curl of the current density and making use of the divergence-free condition leads to the following:

$$\nabla^2\mathbf{B} + \alpha^2\mathbf{B} = \mathbf{B} \times \nabla\alpha(\mathbf{r}), \tag{3.44}$$

$$\mathbf{B} \cdot \nabla\alpha(\mathbf{r}) = 0. \tag{3.45}$$

As such, we have two coupled equations for $\mathbf{B}$ and $\alpha(\mathbf{r})$ that need to be solved together. Many other solutions to the NLFF field have been developed and can be grouped into the following categories:

- Finite Element Modeling,
- Euler Potential Methods,
- Full MHD,
- Potential Grad-Rubin,
- Magneto-frictional,
- Evolutionary methods.

In general, these methods are numerical approximations to the governing set of coupled equations. They are relaxed to a stable state which is assumed to accurately model the coronal field defined by the boundary conditions given.

A non-linear force-free field working group has been working together to advance the modelling of the coronal magnetic field using the existing methods already discussed. The group has developed a series of metrics by which each method can be compared to each other and the true field, if it is known. Figure 3.4 shows the ability of existing NLFF methods to recover the magnetic field from theoretical boundary conditions. As reported in Schrijver *et al.* (2006) the group found that all the methods tested were able, within reasonable error bounds, to reconstruct the theoretical fields in question. Energy calculations for all methods were within 4% of the true value.

Following on from this study much work has been done to test NLFF methods with solar data sets. The *STEREO* satellite mission allows, for the first time, the true structure of the corona to be compared to extrapolations. Figure 3.5 shows the ability of a selection of NLFF methods to recover the coronal field. As can be seen, for real solar data sets the recovered field varies depending on the NLFF method. As such, the methods are unable to fully overcome errors induced by the limited field of view and inaccuracy of present vector magnetogram data. However, the methods still provide insight into the energy budget and global topology of active regions (DeRosa *et al.*, 2009; Metcalf *et al.*, 2008; Schrijver *et al.*, 2008).

3.4.2 Potential Fields

Forcing $\alpha = 0$ results in the current free ($\mathbf{J} = 0$) solution to the coronal magnetic field:

$$\nabla \times \mathbf{B} = 0. \tag{3.46}$$

A result of the current free solution is that the force-free field can be expressed as the gradient of a potential scale function $\phi(r)$, such that:

$$\mathbf{B}(\mathbf{r}) = \nabla\phi(\mathbf{r}). \tag{3.47}$$

Hence, the current free solution is also known as the potential solution.

As the magnetic field must remain divergence free, $\nabla \cdot \mathbf{B}(r) = 0$, the potential magnetic field also satisfies the Laplace equations:

$$\nabla \cdot \mathbf{B} = \nabla(\nabla\phi) = \nabla^2\phi = 0. \tag{3.48}$$

The potential field solution represents a first order approximation to the coronal magnetic topology. Given its reduced complexity, only measurements of the line-of-sight magnetic field are required as boundary conditions, to form a solvable set of equations (Gary, 1989). Green's functions can be used to solve this boundary problem.

Green's functions were first proposed as a solution to calculate the solar magnetic field by Schmidt (1964) and were further developed by Sakurai (1982). These methods require knowledge of the magnetic field at the surface of the Sun. As the solar wind is radial, they additionally assume that the magnetic field is radial at a distance of two or three solar radii. Figure 3.6 shows some potential field extrapolations using this method. As can be seen, the potential solution recovers the global structure of the coronal magnetic field and is often used in the identification of coronal holes.

3.4.3 Linear Force-Free Fields

The third and final class of solutions to the force-free equations are LFF fields, where $\alpha = constant$ and $\nabla \times \mathbf{B} = \alpha\mathbf{B}$. As such, Equation 3.44 reduces to:

$$\nabla^2\mathbf{B} + \alpha^2\mathbf{B} = 0, \tag{3.49}$$

which is the Helmholtz equation.

The method used as part of this study to solve the LFF fields starts from $\nabla \times \mathbf{B} = \alpha\mathbf{B}$. As α is constant for all field lines a closed set of equations can be formed, with only the knowledge of the LOS magnetic field (Alissandrakis, 1981).

In order to use line-of-sight magnetograms to model the solar corona ($z > 0$), the magnetic field is assumed to decay exponentially with z:

$$\mathbf{B} = exp(-k\mathbf{z})\mathbf{B}(x, y, 0), \tag{3.50}$$

where k is the scale height (Alissandrakis, 1981).

With these assumptions Equation 3.50 can be further simplified with the use of Fourier transforms. Taking the Fourier transformation (FT) of both sides of Equation 3.50 with respect to the variables x and y gives:

$$\begin{aligned} \alpha\hat{B}_x - k\hat{B}_y - i2\pi v\hat{B}_z &= 0 & (3.51)\\ k\hat{B}_x + \alpha\hat{B}_y + i2\pi u\hat{B}_Z &= 0 & (3.52)\\ i2\pi v\hat{B}_x - i2\pi\hat{B}_y + \alpha\hat{B}_Z &= 0, & (3.53) \end{aligned}$$

where $\hat{B}_x(u, v, z)$ is the FT of B_x with respect to variables x and y, similarly for $\hat{B}_y(u, v, z)$ and $\hat{B}_z(u, v, z)$. u and v are variables in the FT domain. Solutions exist when the determinant of the coefficients is zero. Giving the scale height k as:

$$k = \pm(4\pi^2 q^2 - \alpha^2)^{\frac{1}{2}}, \tag{3.54}$$

where $q^2 = u^2 + v^2$.

We can then express $\hat{B}_x$, $\hat{B}_y$ and $\hat{B}_z$ in terms of the FT of the normal component of the field at the photospheric boundary, $\hat{B}_z(u, v, 0)$:

$$\hat{\mathbf{B}}(u, v, z) = \hat{\mathbf{G}}(u, v, z)\hat{\mathbf{B}}_z(u, v, 0). \tag{3.55}$$

Real solutions of $\hat{\mathbf{G}}$ exist for $q \geq\mid \alpha \mid /2\pi$ and are:

$$\hat{G}_x = -i(uk - v\alpha)exp(-kz)/2\pi q^2 \tag{3.56}$$

$$\hat{G}_y = -i(vk + u\alpha)exp(-kz)/2\pi q^2 \tag{3.57}$$

$$\hat{G}_z = exp(-kz). \tag{3.58}$$

For $q < |\alpha|/2\pi$, k is imaginary. Taking a linear combination of solutions with positive and negative values of k and requiring that the components be real, gives the following solution for the large scale spatial components of the field:

$$\hat{G}_x = -i\{u\gamma sin(\gamma z) - v\alpha cos(\gamma z) - C(u\gamma cos(\gamma z) + v\alpha sin(\gamma z))\}/2\pi q^2, \tag{3.59}$$

$$\hat{G}_y = -i\{v\gamma sin(\gamma z) + u\alpha cos(\gamma z) - C(v\gamma cos(\gamma z) - u\alpha sin(\gamma z))\}/2\pi q^2, \tag{3.60}$$

$$\hat{G}_z = cos(\gamma z) + C sin(\gamma z), \tag{3.61}$$

where $\gamma = (\alpha^2 - 4\pi^2 q^2)^{1/2}$ and C is a real constant. These equations provide a full set of solutions to the force-free field based on our assumptions.

For a *potential* force-free field $\alpha = 0$ and the equations become:

$$\hat{G}_x = -iukexp(-2\pi qz)/2\pi q^2 \tag{3.62}$$

$$\hat{G}_y = -ivkexp(-2\pi qz)/2\pi q^2 \tag{3.63}$$

$$\hat{G}_z = exp(-kz). \tag{3.64}$$

Thus, LFF field solutions introduces deviations from the potential field due to the introduction of current into the system.

LFF methods are a special class of force-free extrapolation methods. While not as accurate as NLFF methods, they require sufficiently less computational time and for large scale coronal structure they provide an accurate reconstruction of the field *provided the choice of α is correct.*

Previous methods have made use of EUV and X-ray observation of the coronal structure to constrain the choice of α in the LFF extrapolations (Burnette *et al.*, 2004). Other authors have developed methods that minimise the separation between the field lines calculated from observations and extrapolations as a constraint on the choice of α (Lim *et al.*, 2007).

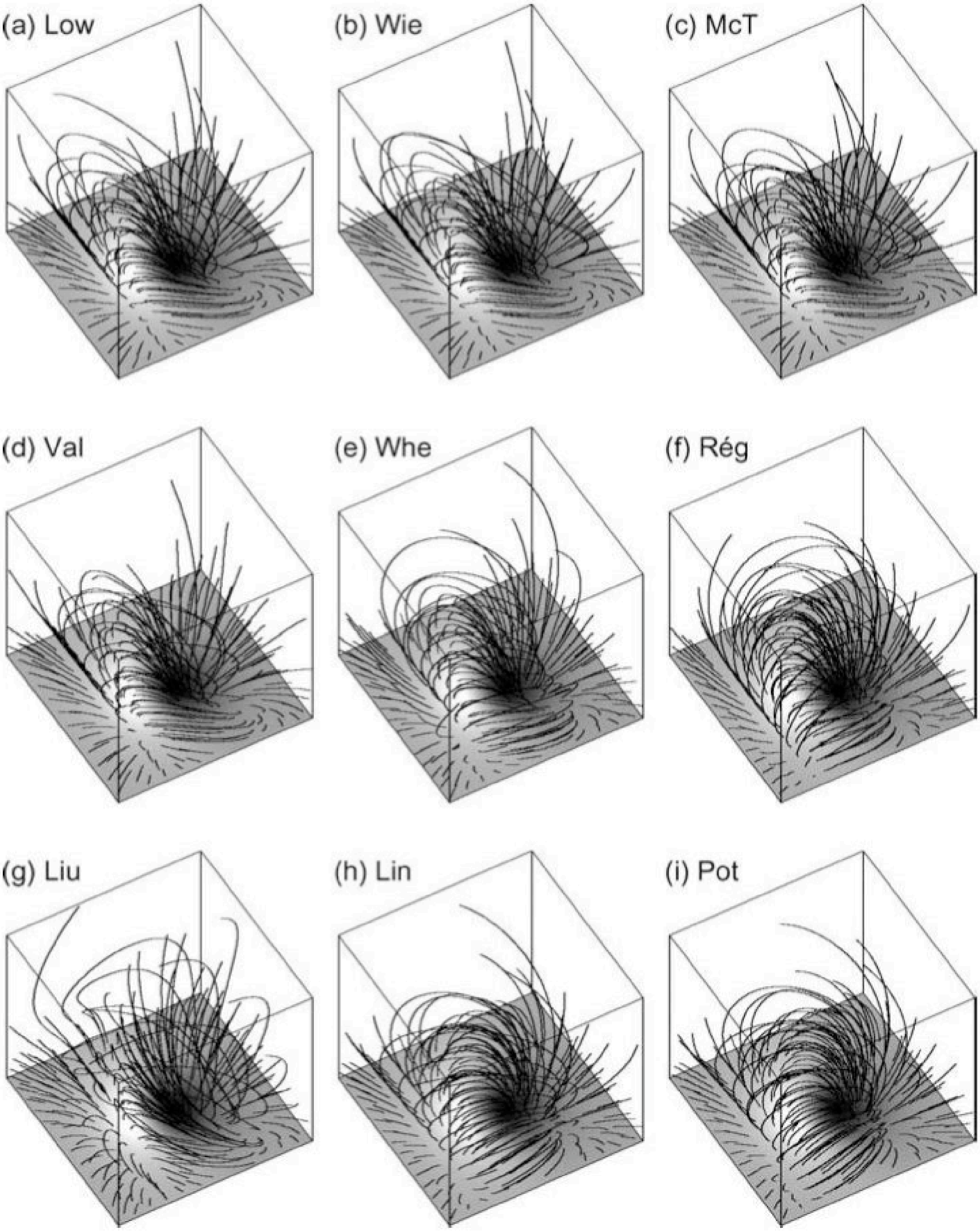

Figure 3.4: Magnetic fields for theoretical data set and extrapolated fields based on boundary conditions of the same the data set. NLFF models are: (a) Low and Lou input model; (b) Wiegelmann; (c) McTiernan; (d) Valori; (e) Wheatland; (f) Rgnier; (g) Liu; (h) LFF field; (i) potential field (Schrijver *et al.*, 2006).

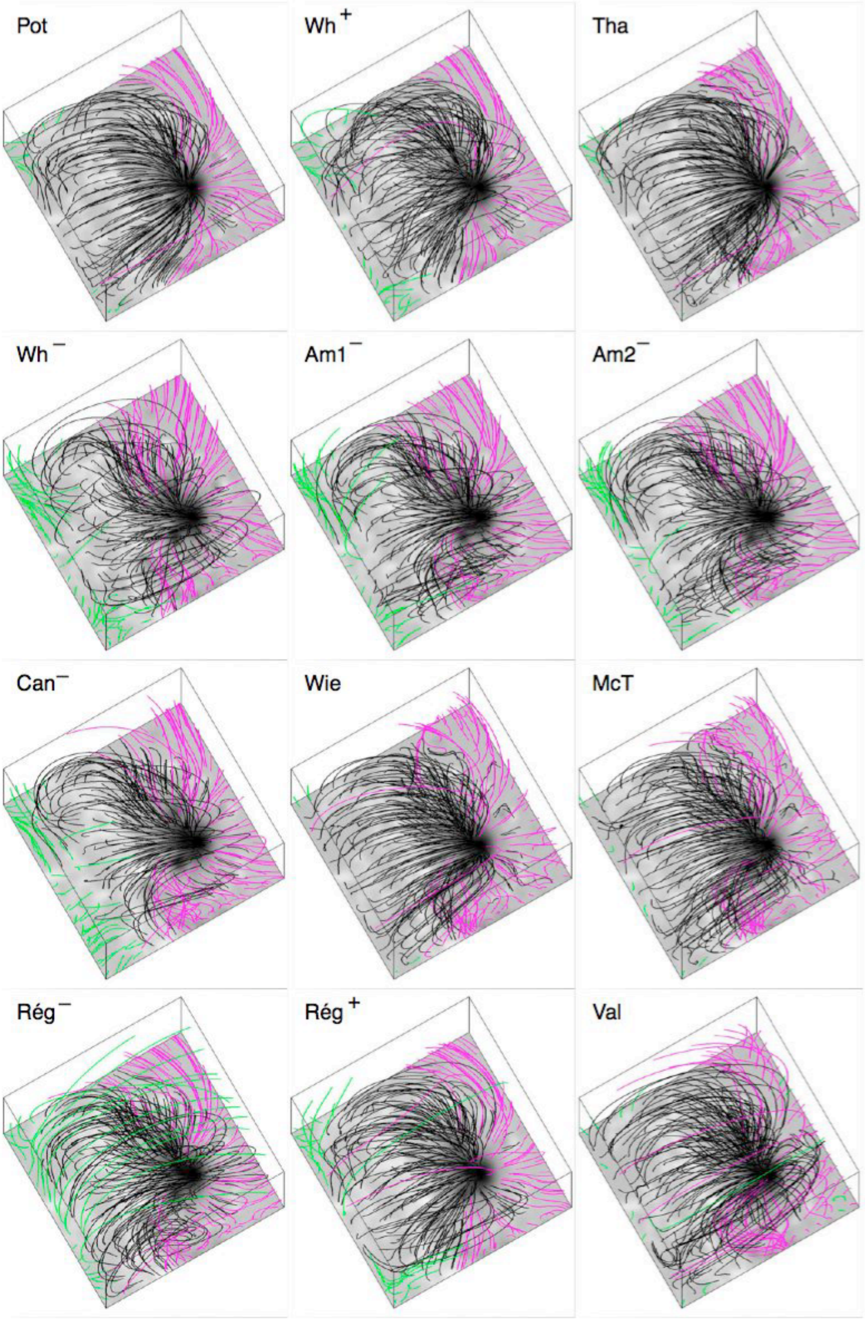

Figure 3.5: Representative field lines in the central portion of active region NOAA 10953 for each a section of NLFF field models. The cubes shown here comprise the same 160 × 160 × 160 pixel sub-volumes excerpted from the full 320 × 320 × 256 pixel computational domain. The starting locations for the integration of the field lines are the same in each case, and form an array of regularly spaced grid points located near the lower boundary of the volume. Black field lines indicate (closed) lines that intersect the lower boundary twice, and red and green field lines represent field lines that leave the box through either the sides or top, with colour indicative of polarity (DeRosa *et al.*, 2009).

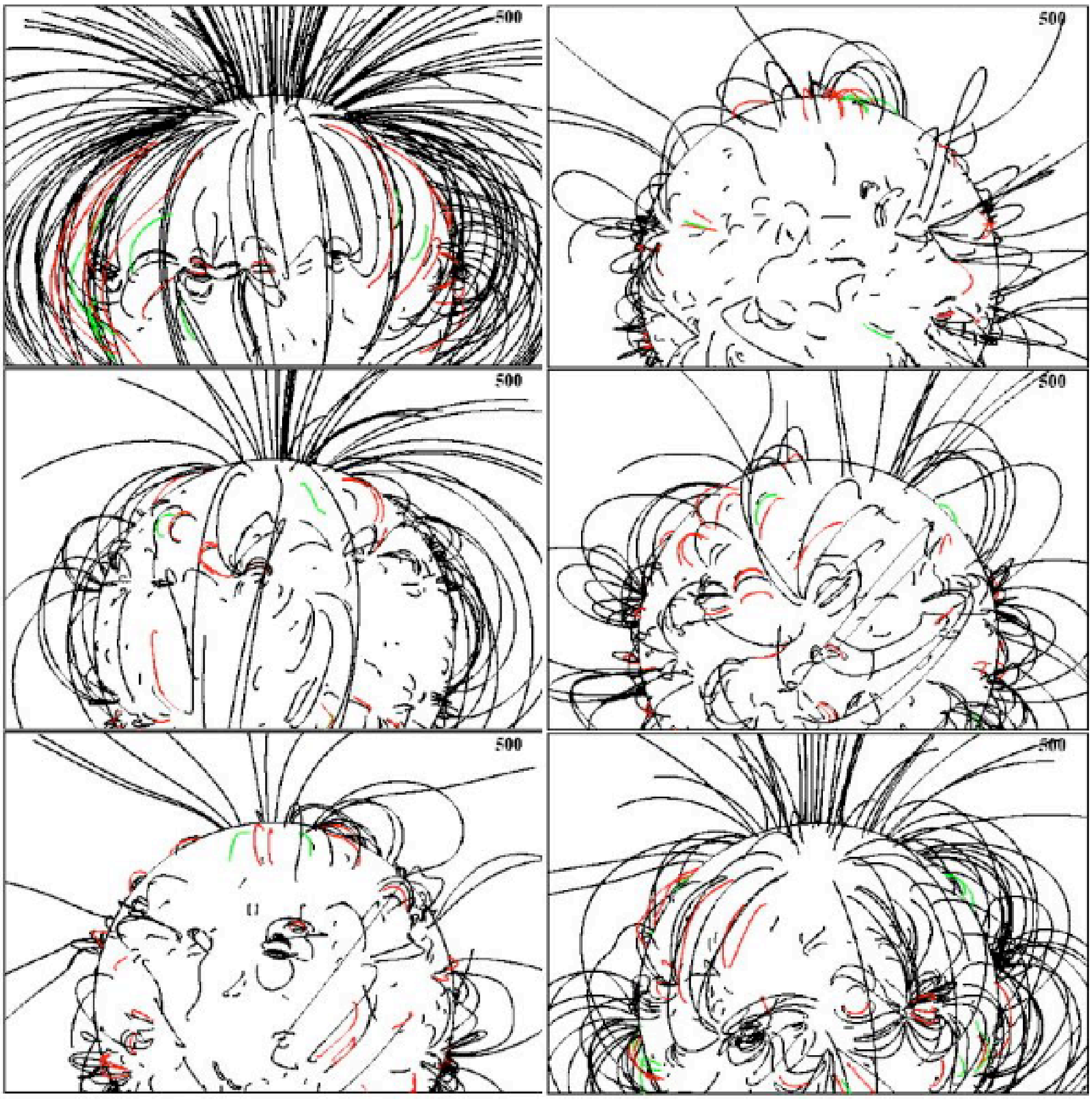

Figure 3.6: Potential field models of the global corona calculated from a source surface model during 6 different phased of the solar cycle. Each display shows 500 potential magnetic field lines, computed from simulated magnetograms that mimic the flux dispersion during the solar cycle (Schrijver & Aschwanden, 2002)

4

Complexity Measure

In this chapter the theory of fractal and multifractal analysis is examined and interpreted for use in the characterisation of magnetic fields on the solar surface. A brief overview is given of existing multiscale methods, along with their relative strengths and weaknesses. A detailed overview is given of the box-counting and wavelet transform modulus maximum methods. These methods are used in later chapters to examine the changing structure of solar active regions. Examples of parameters used are provided to allow for interpretation of later results.

4.1 Introduction

Active regions are formed by turbulent motion deep in the convective zone. Power-law indices of active regions magnetic properties and energies suggest that they are self-similar across a range of scales. The relationship between turbulence and fractal scaling was first suggested by Mandelbrot (1974b). Fractal and multifractal analysis has been used extensively in the study of turbulence and complexity in a wide and varied range of interdisciplinary fields (Mandelbrot, 1977; Schroeder, 1991).

The methods of Euclidean geometry can be used to describe the shape and integer dimensions of a geometric object (e.g., perimeter, area and volume). Complex features such as those found in nature, cannot be adequately described using these traditional methods. Fractals and multifractals are mathematical techniques which can used to describe the complex nature of a system. Fractals relate the detail across scale for self-similar objects. In order to calculate the fractal dimension of any object a relation between detail and scale must be established. For example, by taking meter sticks of various lengths ϵ, the number of sticks that is needed to measure a length is $N(\epsilon)$. Relating these two terms we find the scaling law,

$$N(\epsilon) \propto \epsilon^{-D}, \tag{4.1}$$

where D is the fractal dimension. Fractals are a mathematical tool that give us insight into complexity of systems, something that Euclidean geometry does not offer.

In order to perform the box-counting method on a line, cover the line in line segments of length ϵ. $N(\epsilon) = L/\epsilon$ of them are needed, where L is the length of the line. From this we would find that $N(\epsilon) \approx \epsilon^{-1}$, where the fractal dimension is then 1. When performing the box-counting method on a cube, cover the cube with smaller cubes with sides of length ϵ. $N(\epsilon) = L^3/\epsilon^3$ cubes are required to over the cube. The relation is then $N(\epsilon) \propto \epsilon^{-3}$, where the fractal dimension is 3. For general geometric objects the fractal dimension is the dimension of the objects themselves.

As an example, in order to calculate the fractal dimension of the coast line of Norway, boxes of varying length ϵ are used to cover all the detail, see Figure 4.1. It is found that at the different scales, more or less boxes are needed to cover the detail than in the case of Euclidean objects. It is this non-linear scaling that produces the non-integer fractal dimensions. The fractal dimension for the coastline of Norway is 1.52. As such, it is has more detail than that of a line with dimension 1, but less than a square with dimension 2.

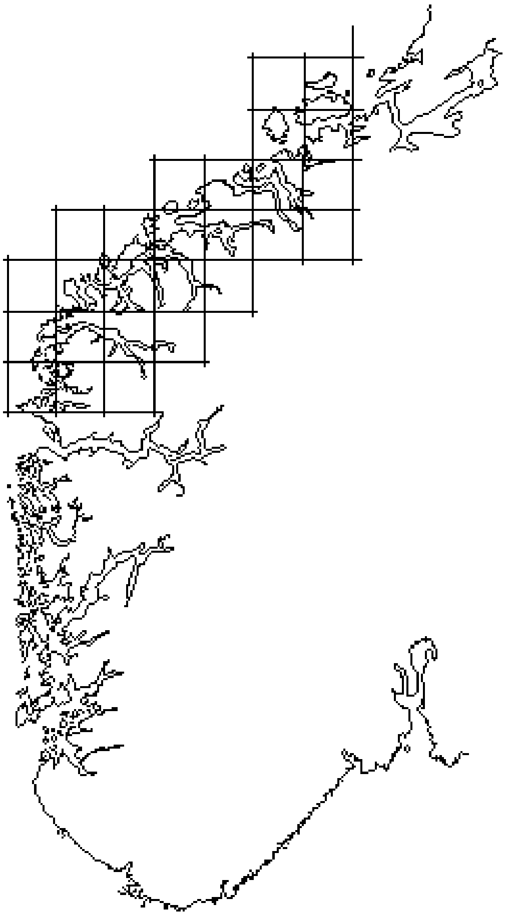

Figure 4.1: The southern coast of Norway (courtesy of Pro Software), fractal dimension of 1.52.

Figure 4.2, shows a number of different theoretical fractals and their fractal dimensions. From this, it can been seen that the fractal dimension gives greater insight into the structure and complexity of systems.

Fractals give insight into the layout of an object across a length of scales. Fractals assume that the object is uniformly distributed. Fractals cannot tell us how the magnitude of a feature changes within its structure. In nature, objects are not black and white, as such, more advanced methods are required to accurately characterise their complexity and structure.

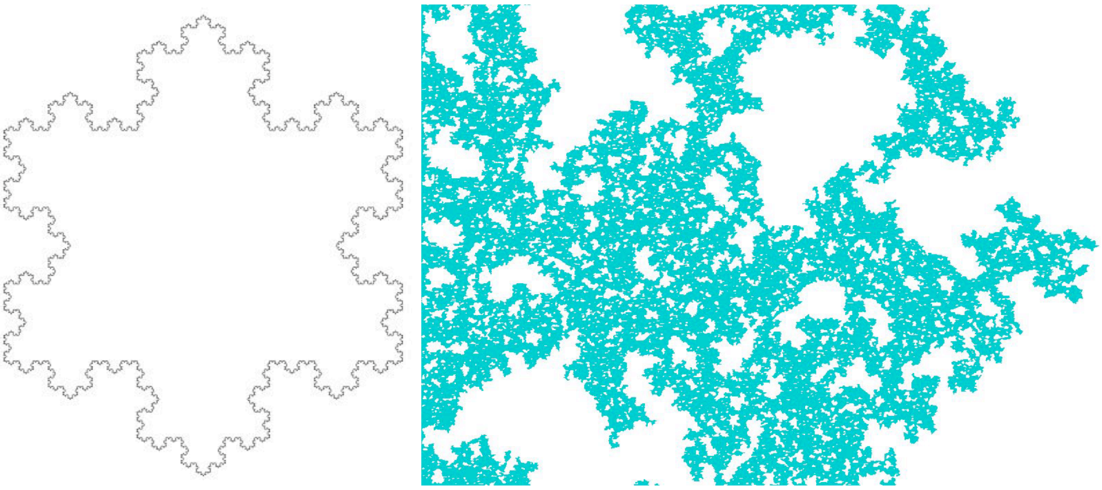

Figure 4.2: Left: Koch snowflake, fractal dimension $D = 1.26$. Right, 2D percolation cluster, fractal dimension $D = 1.89$.

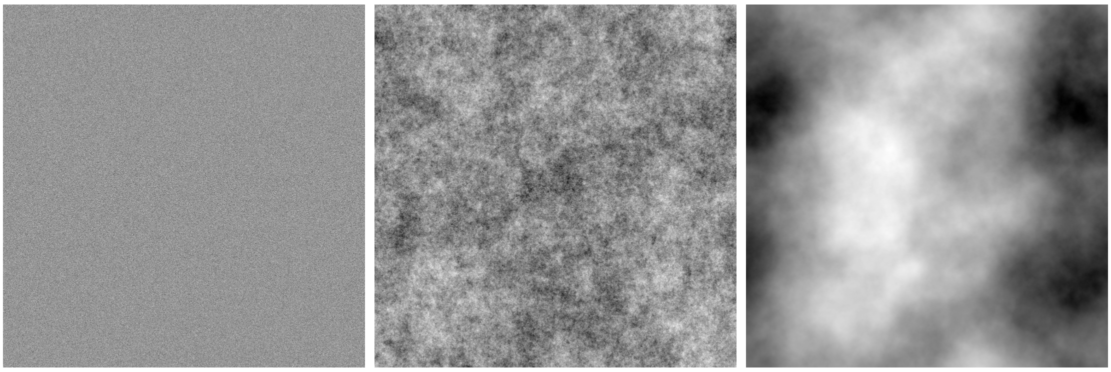

Figure 4.3: Left: Brownian motion image with Hölder exponent of -1.0. Centre: Same but with Hölder exponent of 0.0. Right: Same but with Hölder exponent of 1.0

Multifractals were developed as an expansion of the fractal theory in the mid-eighties. They provide us with a complete description of the fluctuations of singular measures found in chaotic dynamical systems (Mandelbrot, 1974a) or in modelling the energy cascading process in turbulent flows (Frisch, 1995; Meneveau & Sreenivasan, 1991). Multifractal objects have a spectrum of fractal dimensions each with varying degrees of importance and contributions to the overall system or design.

Specifically, the multifractal spectrums, which are plots of $f(\alpha)$ versus α or $D(h)$ vs h provide an intuitive way of characterising the changing physical properties of a system.

For a fractal, a Dirac δ-like spectrum is expected. For a multifractal, the spectrum takes the form of a parabola. The peak of the singularity spectrum corresponds to the fractal dimension of the object. A broadening of the spectrum results in an increase in the complexity or the injection of complexity at different scales. Results can be related between the different spectra as follows:

$$\begin{aligned} f(\alpha) &= D(h), \\ h &= \alpha - 1, \end{aligned}$$

for a two dimensional image. h is known as the Hölder exponent and is a measure of roughness in the data. $h = -1$ corresponds to Dirac white noise, $h = 0$ a step function-like features and $h = 1$ smooth continuously differentiable function, as outlined in Figure 4.3.

The self-similar and turbulent nature of active regions suggest that fractal and statistical methods may be able to accurately characterise complexity and structure within active regions. Furthermore, they may assist in the prediction of space weather events. The fractal and multifractal properties of solar magnetic fields have been studied by many authors (e.g., Lawerence *et al.* 1993,Abramenko 2005b,Conlon *et al.* 2009). Most recently, (McAteer *et al.*, 2005a) used the box-counting methods to analyse the fractal dimension of a large sample of active regions (10^4). They concluded that large complex regions which produced significant flares had larger fractal dimensions. In this body of work both multifractal spectrums are used to study the changing properties of active region and detect any correlations with extreme solar events.

4.2 Multifractal Algorithms

Many multifractal algorithms exist to extract the singularity spectrum and other relevant spectrums. The box-counting and structure function methods are by far the easiest to understand and implement. Other methods use wavelet transformations to extract power spectrums and scaling for calculating the multifractal (Daubechies, 1992; Hewett *et al.*, 2008). A comparison of some of these methods is given in Turiel *et al.* (2005), a brief description of the main methods follows.

4.2.1 Box-counting

The box-counting algorithm is particularly suited to obtaining the fractal and multifractal properties of a system. The basic method involves covering the image in a grid with inter grid spacing ϵ and counting the number of locations that contain part of the detail (Mandelbrot, 1983). Modification to the standard box-counting algorithm are numerous, and their effects on the results vary considerably (Pontrjagin & Schnirelmann, 1932). One modification is to randomly sample the image and re-normalise the calculations (Cadavid *et al.*, 1994) .

Figure 4.4 shows the results of a large statistical study into the relation of active region flaring and the calculated fractal dimension. As can be seen for the 10^4 active regions studied, the range of fractal dimensions is broad and their is no clear distinction between flaring and non-flaring regions. The authors conclude that a fractal dimension, $D(h) > 1.2$ is a necessary but not sufficient condition for flaring.

4.2.2 Structure Functions

Abramenko (2005b) describes structure functions as:

> “statistical moments of the increment of a field, ... very useful non-traditional tools to study multifractality and intermittence.”

Mathematically, they are defined as :

$$S_q(r) =< |\mathbf{B}_{||}(\mathbf{x}+\mathbf{r}) - \mathbf{B}_{||}(\mathbf{x})|^q > \tag{4.2}$$

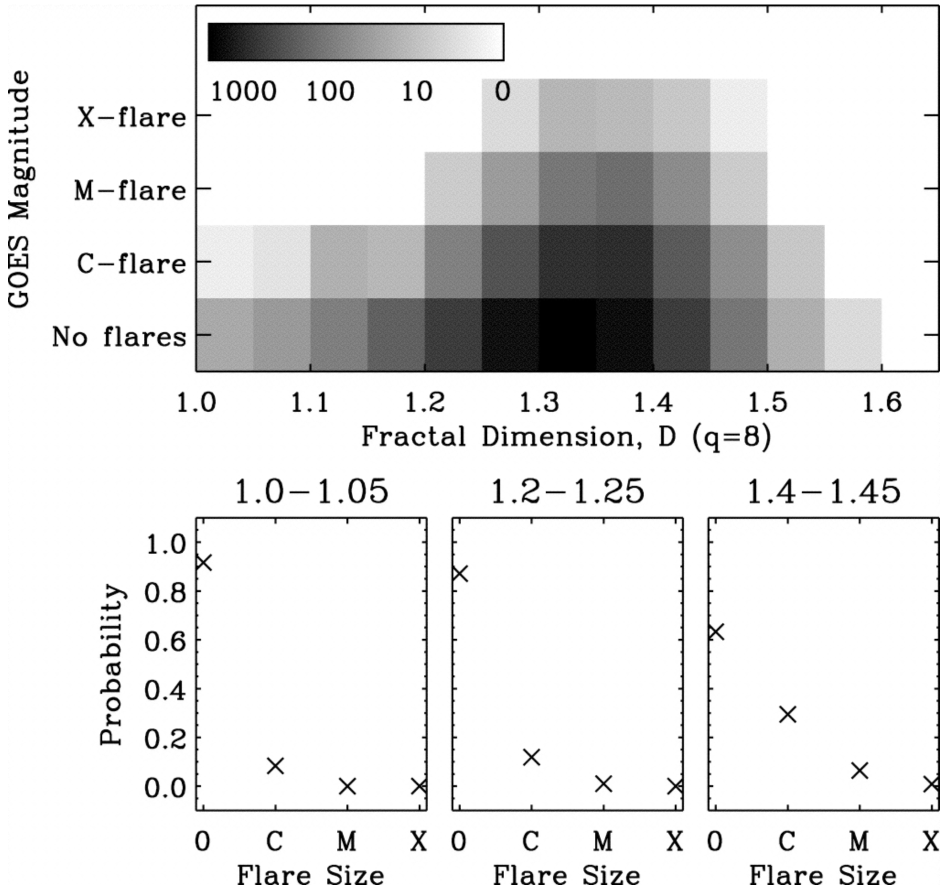

Figure 4.4: Top: The q = 8 fractal dimension of the entire data set is plotted against flare productivity (flare of at most this type occurred in a 24 hr window) according to the colour bar displayed. More, and larger, flares are evident at larger fractal dimensions. A lower threshold of 1.2 (1.25) is necessary to produce M-class (X-class) flares. Bottom: Probability of a region producing C-, M-, and X-class flares is presented at three fractal dimension bins. At small fractal dimension (1.0 1.05) there is only a small chance of any flares. At larger values (1.2 1.25), C-class flares are possible, while at 1.4 1.45 the chances of M- and X-class flares increase (McAteer *et al.*, 2005a).

Where **x** is all the points in the image and **r** a separation vector and q is the moment as described before. The angular brackets denote an averaging over the image, for fixed **r** and q. q is known as the moment and as r acts across a range of spacial scales, q acts across a range of scales in intensity. Structure functions are linear within a given range on a log-log plot. The slope of these plots is given by $\zeta(q)$, if ζ is flat then the image is a fractal and for multifractal samples the curve tends to be concave.

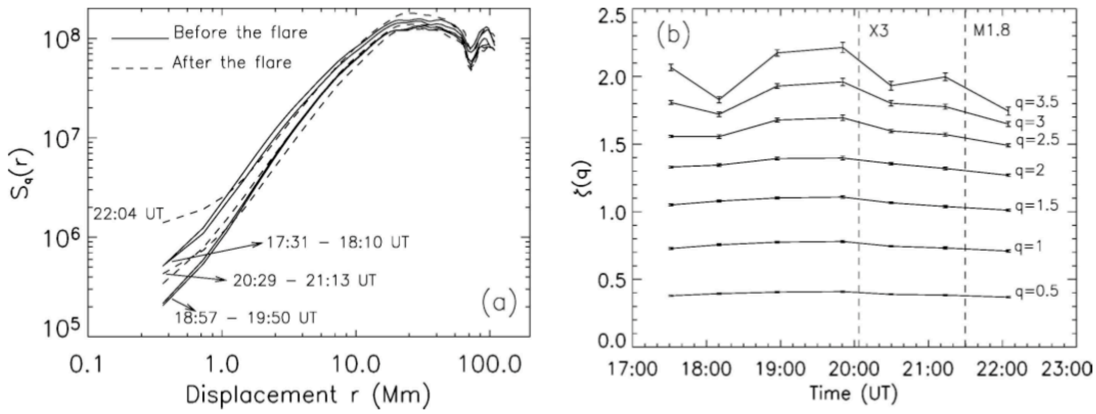

Figure 4.5: Temporal multifractal analysis of the flaring NOAA AR 10030. (a)The structure functions $S_3(r)$, for $q = 3$,for various times before and after the X3 flare (solid lines and dashed lines, respectively). (b)The temporal evolution of the inertial-range scaling exponents $\zeta(q)$ for various selectors q. The onset times of the two flares triggered in the AR are indicated by the two parallel dashed lines (Georgoulis, 2005).

Georgoulis (2005) analysed the predictive ability of a range of fractal, multiscale and structure function methods for their flare prediction ability. The main conclusions are that:

- "The calculation of the fractal dimension is not a particularly fruitful way to discriminate flaring from quiescent active regions".
- "Structure functions $S_q(r)$ and their inertial-range exponent $\zeta(q)$ provide some forecasting clues, but not without limitations".
- The temporal evolution of $\zeta(q)$ may have "specific flare-predictive value" but it remains to be confirmed.

Figure 4.5 shows the temporal evolution of ζ for a range of q values for a flaring active region. As can be seen, there are significant changes in the values of $\zeta(q)$ for large values of q prior to flaring. These are thought to be due to *a decrease in the intermittence in the active regions magnetic field during the pre-flare phase followed by an increase in the post-flare phase.* Abramenko (2005a) reports similar changes in both the level of

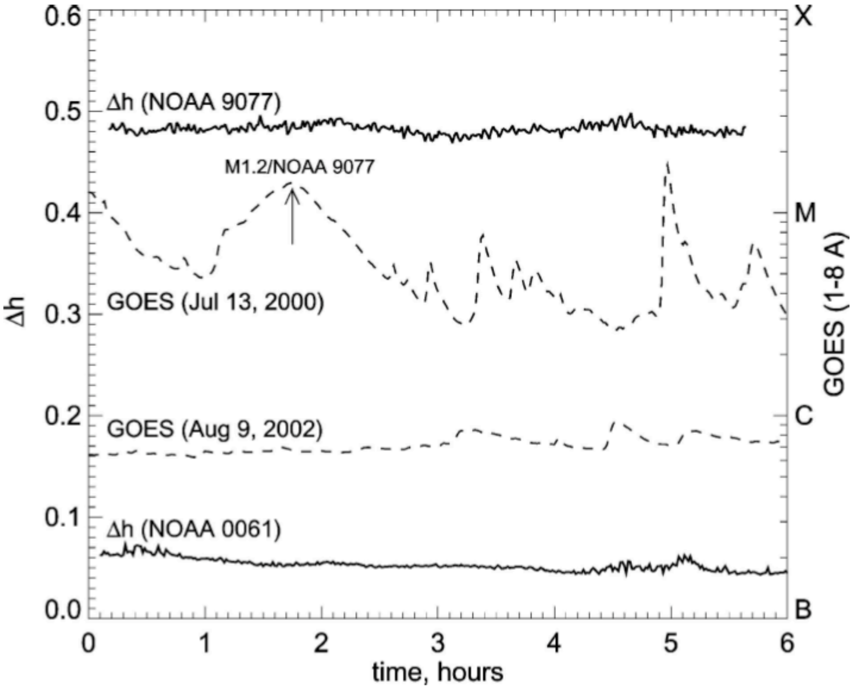

Figure 4.6: Time variations of the measure of multifractality, $\triangle h$ (left axis), and GOES soft X-ray flux (right axis, dashed lines) plotted for 6-h time intervals for the two active regions. Data for NOAA 9077 (black lines) were obtained between 17:00 and 23:00 UT on 13 July 2000. The *arrow* marks the M1.2 flare that occurred in NOAA 9077 whereas other peaks of the GOES flux are associated with other active region on the solar disk. Data from NOAA 0061 (gray lines) refer to an interval between 11:00 and 17:00 UT on 9 August 2002 (Abramenko, 2005a).

multifractality present in flaring and non-flaring regions and temporal changes during flaring periods (Figure 4.6).

While the structure functions do give insight into the behaviour of regions as they evolve and flare, they fail to resolve the small scale elements of the system (Abramenko, 2005a,b; Georgoulis, 2005). Additionally, they are ill defined for negative values of q.

4.2.3 Wavelet Transform Modulus Maximum Method

The wavelet transform (WT) is similar to the Fourier transform in its application to signal processing and other areas. It has a major advantage as it characterises the signal onto a set of functions that vary in both scale and location. This makes the WT an excellent tool for the analysis of the scale-invariance properties of fractal and multifractal signals. Muzy *et al.* (1995) described the WT as a “mathematical microscope”.

The wavelet transform modulus maxima (WTMM) method was introduced by Arneodo *et al.* (1995b). It is a wavelet-based method that uses the different dilations of the mother wavelets as “generalised oscillating boxes”(Khalil *et al.* 2006 and references therein). The use of the wavelets instead of boxes removes any possible errors due to smoothing or discritisation of the data. The WTMM method has shown promising results in many areas. Examples include the study of cloud structures with images from Landsat satellite images and the concentration of Hydrogen in galactic arms (Khalil *et al.*, 2006; Roux *et al.*, 2000a).

4.3 The Box-counting Method

Although fractals are useful for describing the complexity of images and regions, it has been found that most systems are a convolution of different fractal processes. To accurately characterise such systems, the idea of a *multifractal* was introduced. Multifractals, like fractals, relate the number of boxes $N(\epsilon)$ to the size of each box ϵ and are characterised by a similar equation to Equation 4.1:

$$N(\epsilon) \propto \epsilon^{-f(\alpha)}, \tag{4.3}$$

where instead of a single exponent, there is a spectrum of exponents $f(\alpha)$ each with a relative strength or significance α.

Information about the $f(\alpha)$ spectrum is calculated using a scaling exponent q. During the calculation of each α, $f(\alpha)$ pair q is used to extract a different moment scale. q, acting as a microscope, allows for a detailed examination of the range of scales that exist within the measure of the system. In the case of active region magnetogram images the measure of the system is the magnetic flux. When q is positive it magnifies the larger measures, dwarfing the smaller ones. The opposite occurs when q is negative; it inverts the measure, thus enhancing the smaller measures and dwarfing the larger ones.

The measure of the line-of-sight magnetograms is given by:

$$B_\epsilon(i) = |\sum B(k,m)| \qquad \forall\ k,\ m \in i \text{ of size } \epsilon, \tag{4.4}$$

as such oppositely signed magnetic flux elements are allowed to cancel within each box (Cadavid *et al.*, 1994; Lawerence *et al.*, 1993). Thus $B_\epsilon(i)$ is always positive and contains information about the mixing of oppositely signed flux elements (*i.e.* neutral lines). The range of box sizes examined was from 5 to 47 Mm. This allowed the examination of small scale neutral lines and structures and restricted the analysis of larger bipolar regions that could have skewed the results.

The normalised flux $\hat{B}_\epsilon(i)$ is then given by:

$$\widehat{B}^q_\epsilon(i) = \frac{B^q_\epsilon(i)}{\sum_{i=1}^{N(\epsilon)} B^q_\epsilon(i)} = \frac{B^q_\epsilon(i)}{z_\epsilon(q)}, \tag{4.5}$$

where $z_\epsilon(q) = \sum_{i=1}^{N(\epsilon)} B^q_\epsilon(i)$ is known as the partition function.

The strength or significance of a measure is then:

$$\begin{aligned} \alpha(q) &= \lim_{\epsilon \longrightarrow 0} \sum_{i=1}^{N(\epsilon)} \widehat{B}^q_\epsilon(i) \log_\epsilon B_\epsilon(i), && (4.6) \\ &= \lim_{\epsilon \longrightarrow 0} \sum_{i=1}^{N(\epsilon)} \widehat{B}^q_\epsilon(i) \alpha_\epsilon(i), && (4.7) \end{aligned}$$

where $B_\epsilon(i) = \epsilon^\alpha$. $\alpha(q)$ measures the concentration strength of the range of measure scales given by q (Chappell & Scalo, 2001). For $\alpha = 2$ we have a two-dimensional image, for a sharp spike $\alpha = 0$.

The distribution (fractal dimension) of all the points in the image of a given concentration strength is then given by $f(\alpha)$:

$$f(q) \quad = \quad \lim_{\epsilon \longrightarrow 0} \sum_{i=1}^{N(\epsilon)} \widehat{B}_\epsilon^q(i) \log_\epsilon \widehat{B}_\epsilon(i). \tag{4.8}$$

Inserting Equation 4.5 gives:

$$f(q) \quad = \quad \lim_{\epsilon \longrightarrow 0} \sum_{i=1}^{N(\epsilon)} \widehat{B}_\epsilon^q(i) \log_\epsilon \frac{B_\epsilon^q(i)}{z_\epsilon(q)}. \tag{4.9}$$

Rearranging the $\log_\epsilon$ allows:

$$f(q) \quad = \quad \lim_{\epsilon \longrightarrow 0} \sum_{i=1}^{N(\epsilon)} \widehat{B}_\epsilon^q(i)(\log_\epsilon B_\epsilon^q(i) - \log_\epsilon z_\epsilon(q)). \tag{4.10}$$

Taking down the power of q gives:

$$\begin{aligned} f(q) &= \lim_{\epsilon \longrightarrow 0} \sum_{i=1}^{N(\epsilon)} \widehat{B}_\epsilon^q(i) q \log_\epsilon B_\epsilon(i) - \lim_{\epsilon \longrightarrow 0} \sum_{i=1}^{N(\epsilon)} \widehat{B}_\epsilon^q(i) \log_\epsilon z_\epsilon(q), & (4.11) \\ f(q) &= q \lim_{\epsilon \longrightarrow 0} \sum_{i=1}^{N(\epsilon)} \widehat{B}_\epsilon^q(i) \log_\epsilon B_\epsilon(i) - \lim_{\epsilon \longrightarrow 0} \sum_{i=1}^{N(\epsilon)} \widehat{B}_\epsilon^q(i) \log_\epsilon z_\epsilon(q), & (4.12) \\ & & (4.13) \end{aligned}$$

Using Equation 4.6:

$$\begin{aligned} f(\alpha) &= q\alpha - \lim_{\epsilon \longrightarrow 0} \sum_{i=1}^{N(\epsilon)} \widehat{B}_\epsilon^q(i) \log_\epsilon z_\epsilon(q), & (4.14) \\ &= q\alpha - \tau, & (4.15) \end{aligned}$$

where $\tau = \lim_{\epsilon \rightarrow 0} \log_\epsilon E(z_\epsilon(q))$. $E(z_\epsilon(q))$ is the expectation value of the partition function. The Hausdroff, or fractal, dimension is given by $f(\alpha(q = 0))$. This corresponds to the peak of the $f(\alpha)$ versus α curve. Positive q corresponds to the left side of the $f(\alpha)$

versus α curve and the larger measures. The right side corresponds to negative values of q and smaller measures. Smaller measures have larger values of α as they occupy and contribute to more of the image.

4.4 The Wavelet Transform Modulus Maximum Method

The multifractal formalism was introduced in the mid 1980s (Halsey *et al.*, 1986; Parisi & Frisch, 1985). It provides a statistical description of the fluctuations of the regularity of singular measures that are found in chaotic dynamical systems (Halsey *et al.*, 1986) or in the modelling of the energy cascading process in turbulent flows (Mandelbrot, 1974a; Meneveau & Sreenivasan, 1991). A self-similar monofractal system can be well characterised by a single global scaling quantity like the Hurst exponent H. Multifractals display a complex geometrical structure best described by a spectrum of fractal dimensions, either the so-called [$D(h)$ or $f(\alpha)$] singularity spectrum or the generalised fractal dimensions D_q (Badii & Politi, 1985).

In the mid 1990s, the ability of the continuous wavelet transform to look at signals through position and scale was shown to provide a natural way of performing a unified multifractal analysis of both singular measures and multi-affine functions. As an illustration of the interest in using wavelets, a singular behaviour at x_0 of a function f can be described by:

$$|f(x) - f(x_0)| \sim |x - x_0|^{h(x_0)}, \tag{4.16}$$

can be seen in the wavelet transform coefficients under a power law:

$$T_\psi[f](a, b) =< f, \psi_{a,b} >= 1/a \int_{-\infty}^{+\infty} dx\, f(x)\psi^*(x - b/a) \sim a^{h(\mathbf{x_0})}, \tag{4.17}$$

where ψ is the analysing wavelet and $h(x_0)$ is the Hölder exponent. The different dilations of the analysing wavelet act as “generalised oscillating boxes” that reveal quantitative information at every scale considered. The wavelet transform modulus maxima (WTMM) method is a wavelet based multifractal formalism designed for studying self-similar properties of 1D signals (Arneodo *et al.*, 1995b; Muzy *et al.*, 1991, 1993, 1994). The method avoids some of the drawbacks of both the box-counting multifractal formalism and the structure function approach (Conlon *et al.*, 2008). This method was later generalised to 2D (Arneodo *et al.*, 1999; Arnéodo *et al.*, 2000), 3D (Kestener & Arneodo, 2003) scalar functions and finally to vector-valued functions (Kestener & Arneodo, 2004, 2007).

In astrophysics, the 2D WTMM method was adapted and used to characterise the anisotropic structure of atomic hydrogen gas (HI) in the Galactic disk (Khalil *et al.*, 2006). From the analysis of very large mosaics taken from the Canadian Galactic Plane Survey (Taylor *et al.*, 2003), directional roughness exponents were introduced to show that the HI in the Galactic spiral arms has a scale-dependent anisotropic signature while the HI in the inter-spiral-arm regions exhibits scale-independent anisotropy.

4.4.1 Basics Of The 2D WTMM Method

The 2D WTMM method provides a way to estimate the $D(h)$ singularity spectrum (i.e. the fractal (Hausdorff) dimension of the set of points in the 2D image that are characterised by a specific local roughness (Hölder) exponent h, or, in the case of a monofractal (isotropic) signature, by a global Hurst exponent; Arnéodo *et al.* 2000). Let us in brief recall the main steps of the WTMM method (details can be found in Arnéodo *et al.* 2000):

1. Computation of the 2D continuous wavelet transform of the input image (function $f(x,y)$) with analysing wavelet defined as the partial derivatives of a smoothing

kernel ϕ (Gaussian):

$$\begin{aligned}\mathbf{T}_{\psi}[f](\mathbf{b},a) &= \begin{pmatrix} T_{\psi_1}[f] = a^{-2}\int d^2\mathbf{x}\ \psi_1(a^{-1}(\mathbf{x}-\mathbf{b}))f(\mathbf{x}) \\ T_{\psi_2}[f] = a^{-2}\int d^2\mathbf{x}\ \psi_2(a^{-1}(\mathbf{x}-\mathbf{b}))f(\mathbf{x}) \end{pmatrix}, \\ &= \nabla\{T_{\phi}[f](\mathbf{b},a)\} \\ &= \nabla\{\phi_{\mathbf{b},a} * f\},\end{aligned} \tag{4.18}$$

where $\psi_1 = \partial\phi/\partial x$ and $\psi_2 = \partial\phi/\partial y$.

2. For each scale a, extract the WTMM edges defined as the locations $\mathbf{b}$ where the WT modulus $\mathcal{M}_{\boldsymbol{\psi}}[f](\mathbf{b},a) = |\mathbf{T}_{\boldsymbol{\psi}}[f](\mathbf{b},a)|$ is locally maximum in the direction of the WT vector $\mathbf{T}_{\boldsymbol{\psi}}[f](\mathbf{b},a)$. These WTMM points lie in connected *maxima chains*.

3. Extract the WT skeleton which is the set of *maxima lines* $\mathcal{L}_{\mathbf{x}_0}$ defined as the location $\mathbf{b}$ where the WT modulus $\mathcal{M}_{\boldsymbol{\psi}}[f](\mathbf{b},a)$ is a local maximum along a *maxima chain.* It is important to recall here that these lines contain all the information about the local Hölder regularity properties of the function f under consideration and that along a maxima line $\mathcal{L}_{\mathbf{x}_0}$ that points to $\mathbf{x}_0$ in the limit $a \to 0^+$, the wavelet transform modulus behaves as a power law with exponent $h(\mathbf{x}_0)$:

$$\mathcal{M}_{\psi}[f][\mathcal{L}_{\mathbf{x}_0}(a)] \sim a^{h(\mathbf{x}_0)}, \tag{4.19}$$

4. From the WT skeleton compute the partition functions:

$$\mathcal{Z}(q,a) = \sum_{\mathcal{L}\in\mathcal{L}(a)} \mathcal{M}_{\psi}[f](\mathbf{x}\in\mathcal{L},a)^q, \tag{4.20}$$

which allows to define the $\tau(q)$ scaling exponents as $\mathcal{Z}(q,a) \sim a^{\tau(q)}$, $a \to 0^+$.

One can optionally compute the companion partition functions and define the corresponding scaling exponents when $a \to 0^+$

$$\begin{aligned} h(q,a) &= \sum_{\mathcal{L}\in\mathcal{L}(a)} \ln|\mathcal{M}_{\boldsymbol{\psi}}[f](\mathbf{x},a)| \; W_{\boldsymbol{\psi}}[f](q,\mathcal{L},a) \;\sim a^{h(q)}, &(4.21)\\ D(q,a) &= \sum_{\mathcal{L}\in\mathcal{L}(a)} W_{\boldsymbol{\psi}}[f](q,\mathcal{L},a) \; \ln(W_{\boldsymbol{\psi}}[f](q,\mathcal{L},a)) \;\sim a^{D(q)}. &(4.22)\end{aligned}$$

5. Compute the $\tau(q)$ spectrum by performing linear regression fits of the $\mathcal{Z}(q,a)$ partition functions and finally compute the $D(h)$ singularity spectrum from the scaling exponents $h(q)$ and $D(q)$.

Note that recently, an alternative method based on the discrete wavelet transform was proposed, namely the Wavelet Leaders (Abry *et al.*, 2004). We think that the continuous WT better suits our goal to provide a selective multifractal analysis of multi-component images, i.e the ability to quantify multifractal properties of an object embedded into a complex texture such as active region magnetic fields surrounded by the quiet Sun texture.

5

Complexity Of Active Region Photospheric Fields Using The Box-counting Method

Magnetohydrodynamic turbulence is thought to be responsible for producing complex, multiscale field distributions in solar active regions. Here we explore the multiscale properties of the magnetic field of a number of evolving active regions. The multifractal spectrum was obtained using a modified box-counting method to study the relationship between the magnetic field multifractality and the region's evolution and activity. The initial emergence of each active region was found to be accompanied by characteristic changes in the multfractal spectrum. Additionally, the method was found to be responsive to changes in the structure of active regions prior to flaring. This is based on research published in Conlon *et al.* (2008).

5.1 Introduction

Fractal and multifractal methods give insight into the changing structure of natural systems. Given the self-similar and power-law distribution within the magnetic structure of active regions these mathematical tools can be used to characterise their complexity and structure. Several authors have investigated the self-similar nature of solar active regions (Abramenko, 2005b; Abramenko *et al.*, 2002; Georgoulis, 2005; Lawrence *et al.*, 1996; McAteer *et al.*, 2005a). Numerous methods have been used to extract parameters associated with the turbulent properties of active regions and some have found a relation between multifractal parameters and flaring (Abramenko, 2005a). A more extensive statistical study by McAteer *et al.* (2005a) found that flaring activity was only weakly related to a region's fractal dimension. Our work expands on the methods of McAteer *et al.* (2005a), by using a box-counting method to extract the multifractal spectrum of evolving active regions.

Multifractal methods are sensitive to changes across a range of scales and are excellent tools for characterising the complexity of active region magnetic fields. This allows for the detection of topological changes in the distribution of active region magnetic fields during region evolution. Georgoulis (2005) concluded that fractal and multifractal parameters have a limited ability in the prediction of space weather events. Although, Georgoulis (2005) concluded that the temporal evolution of fractal and multifractal parameters may have some flaring predictive powers. Additionally, Abramenko (2005b) has shown the power of multifractal methods to detect the difference between flaring and non-flaring regions.

This work investigates the potential of box-counting multifractal methods to detect characteristic changes in the magnetic field of active regions and their association if one exists with flaring activity.

5.2 Data Pre-Processing

For the purpose of this work, four active regions were analysed as they evolved on the solar disk. NOAA 10727 emerged as a β region on 24 January 2005 and experienced significant flux emergence on the 29th, before rotating off disk on 3 February 2005. NOAA 10763 rotated onto the disk on 11 May 2005 as a $\beta\gamma$ region. It subsequently formed a δ in its trailing portions and went into decay from 16 May 2005. The most active region in the sample was the rapidly emerging active region, NOAA 10488. This region emerged on 26 October 2003 to become a $\beta\gamma\delta$ region on the subsequent day. The final region in the sample was NOAA 10798, which emerged on 15 August 2005 and slowly grew in size and complexity over a ten-day period.

Flux densities were corrected using the algorithm suggested by Berger & Lites (2003) and implemented in Green *et al.* (2003). Magnetic field projection effects were corrected by assuming a radial field at each point on the solar disk and implementing a cosine-correction algorithm. Image projection effects were corrected using an equal-area cylindrical projection method (Bugayevskiy & Snyder, 1995; McAteer *et al.*, 2005b).

5.3 Application Of The Box-counting Algorithm

The algorithm used was a modified box-counting method as developed by Mach & Mas (1997). The basic method involves covering the image with a grid of inter-grid spacing ϵ and counting the number of locations that contain part of the detail (Mandelbrot, 1983). A modification of this is to randomly sample the image and re-normalise the calculations (Cadavid *et al.*, 1994).

A number of modifications were made to the basic box-counting method in order to increase the accuracy of the method. These included the “fuzzy ball” method. This involves shaking the boundary of the box to increase the accuracy of the result (Alber, 1997).

Due to errors in the calculation of the multifractal spectrum for negative q, we decided to characterise the changing complexity by only using the results for positive q (the poor resolution of the fine scale structures being enhanced by the discrete and numerical nature of the method (Alber, 1997). The following terms were to used describe changes in the multifractal spectrum, *contribution diversity* and *dimensional diversity* (Chappell & Scalo, 2001) defined as:

$$C_{\text{div}} = \alpha_{\text{max}} - \alpha_{\text{min}}, \tag{5.1}$$

$$D_{\text{div}} = f(\alpha)_{\text{max}} - f(\alpha)_{\text{min}}, \text{ for } q > 0. \tag{5.2}$$

This allows us to parameterize changes in the system over time. A broadening of the spectrum would result from a decrease in the contribution of larger measures to an active region. While the region grows, the larger measure will become more significant and the contribution diversity will increase.

The program was designed in the C programming language, as the final goal of the project is a real time analysis package. The code was developed in a segmented manner and is outlined as follows:

1. Read in the FITS images.
2. Calculate physical parameters (image size, active region area and magnetic field strength).
3. Perform box-counting over the desired range of scales.
4. Calculate the multifractal parameters.
5. Perform regression across scales.

The CFITSIO library (a subroutine library for reading and writing fits files) was implemented to read in the fits formatted images (Pence, 1999). The multifractal code is a modified version of the MFRAC v2.0 algorithm, as developed by (Mach & Mas, 1997). The regression method used was a bi-weight function developed by Mostelle & Tukey (1977), this is a modified robust regression method.

5.4 Testing: Theoretical Fractals

The method described in Section 4.3 was tested using a known fractal and multifractal. The Sierpinski carpet was chosen as the fractal for testing. This was constructed by covering the domain with a 3 × 3 grid and setting the middle section to zero. This process was continued until the smallest scale was reached (one pixel). This created a self-similar image with a fractal dimension of $D = \log(8)/\log(3) \approx 1.8928$. The top left of Figure 5.1 shows an image of the Sierpinski carpet with its corresponding theoretical singularity spectrum below. Using the methods outlined in the previous section, a point-like singularity spectrum with a fractal dimension of D or $f(\alpha) = 1.89 \pm 0.01$ was obtained with a corresponding value of $\alpha = 1.87 \pm 0.01$. A monofractal has the same fractal dimension at all scales with equal strength.

A multifractal image and its theoretical singularity spectrum was created using the methods of Cadavid *et al.* (1994). The multifractal image is shown in the centre-top panel of Figure 5.1. Its corresponding theoretical spectrum (dashed lines) is given in the panel below. Also shown is the spectrum obtained using our methods. It can be seen that there is strong agreement between the theoretical and calculated spectra for $q > 0$ (*i.e.*, the left-hand side of the spectrum). Results for the right side of the spectrum ($q < 0$) deviate due to errors in the discretization of the data and numerical issues with small measures. The final set of panels on the far right of Figure 5.1 show an MDI magnetogram for NOAA 10030. Its singularity spectrum is shown in the panel below. Due to the errors already mentioned, only the left side of the spectrum ($q > 0$) could be reliably calculated.

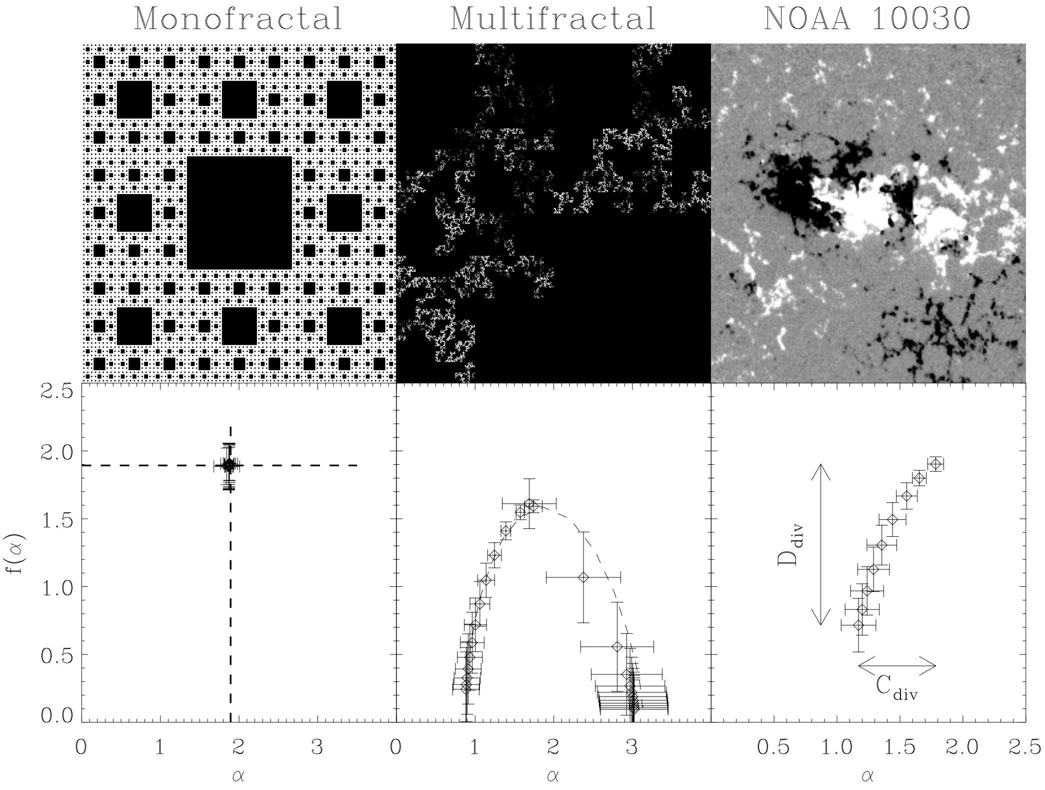

Figure 5.1: (Top) A monofractal image, multifractal image, and magnetogram of NOAA 10030. (Bottom) The corresponding $f(\alpha)$ spectra. Dashed lines in the bottom left image centre on the fractal dimension of the monofractal. Dashed lines in bottom cent panel present the theoretical multifractal spectrum (Conlon *et al.*, 2008).

5.5 Active Regions

5.5.1 NOAA 10488

The evolution of the NOAA 10488 is shown in Figure 5.2 and Figure 5.3. The region emerged rapidly over three days, starting on 26 October 2005. From Figure 5.2, the emergence was characterised by a significant change in the region's $f(\alpha)$ spectrum. Most notably, the contribution and dimensional diversities became smaller as the region formed a large-scale coherent structure. This is due to large field measures becoming more significant (*i.e.*, moving to higher α) and more complex (*i.e.*, moving to larger $f(\alpha)$).

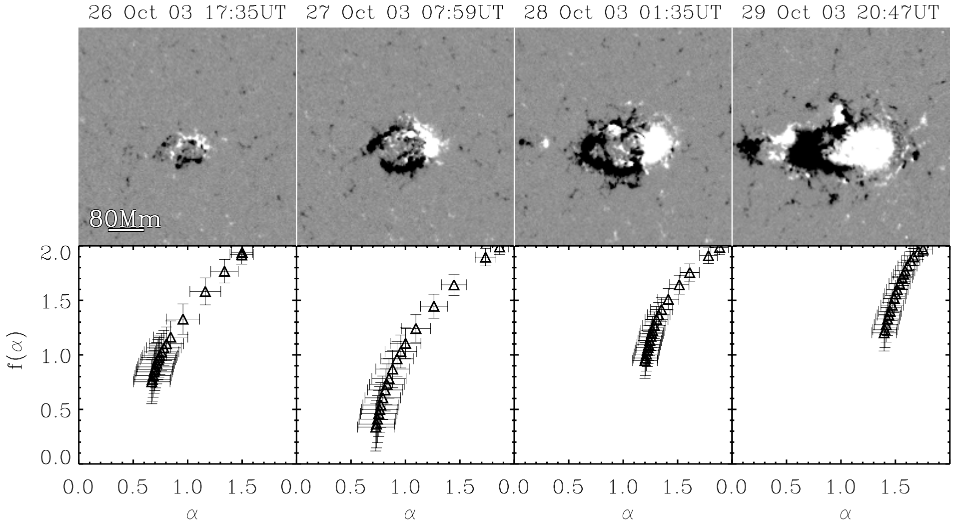

Figure 5.2: The emergence of NOAA 10488 on 26 − 30 October 2003. (Top) MDI magnetograms. (Bottom). The corresponding $f(\alpha)$ spectra.

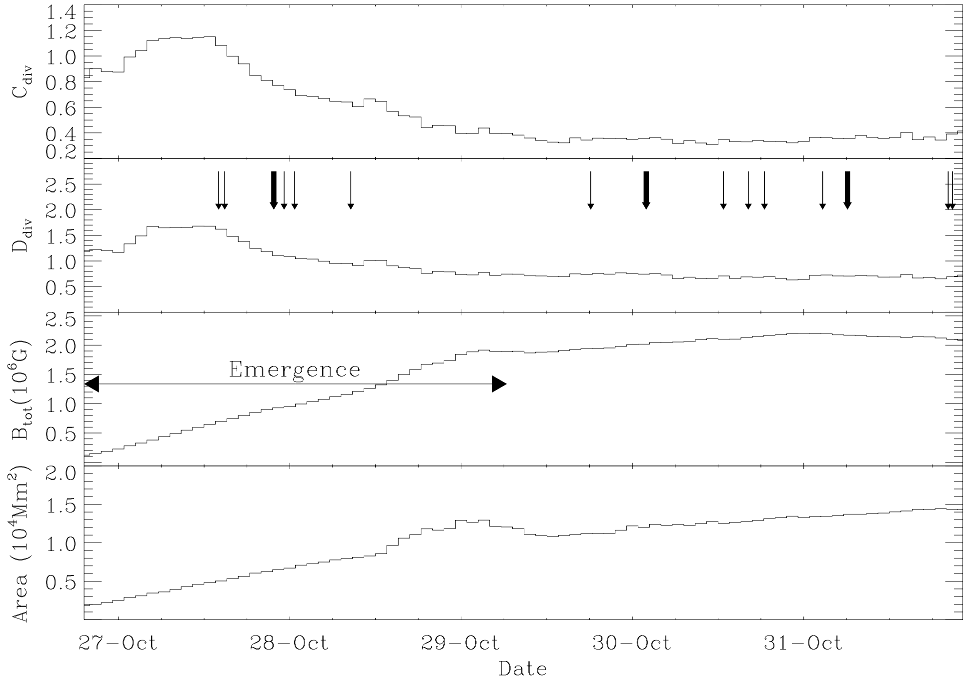

Figure 5.3: The evolution of NOAA 10488. (Top) Contribution diversity. (Second) Dimensional diversity. The total field strength (Gauss) and area (Mm) of the region are shown in the third and fourth panel respectively. Associated C-class flares are indicated by thin arrows, bolder arrows indicate M-class flares.

Figure 5.3 shows the evolution of NOAA 10488's area, total flux, and contribution and dimensional contributions over five days, from 27 October to 1 November 2007. The initial flux emergence is characterised by a small increase in the multifractal parameters on 27 October 2005. This results from the emergence of isolated small-scale flux elements which subsequently coalesce to form a number of large-scale structures with reduced significance. The multifractal properties of the region then remain constant for a number of hours as the region continues to grow in size and total flux.

At the end of 27 October 2003, the multifractal nature of the region again begins to change. Although the region continues to evolve rapidly, the contribution and diversity dimensions shows a continued decrease, until reaching a plateau on 29 October 2005. This gradual decrease in D_{div} and C_{div} results from an increase in the significance and fractal dimension of larger scales as the region becomes a large-scale coherent active region. This gradual evolution of the region's multifractal properties is accompanied by an increase in the flaring activity of the region. The region then remains relatively stable from 29 October 2003 to 1 November 2003, during which its fractal properties do not change significantly.

5.5.2 NOAA 10798

The emergence of NOAA 10798 is seen in Figure 5.4 and Figure 5.5. The initial emergence of flux is characterised by an increase in the contribution and dimensional diversity, due to the "dust" nature of the large flux elements at this time. Similarly to NOAA 10488, the contribution diversity and dimensional diversity decreases as the region develops a coherent structure. The region is observed to flare at 10:06 UT on 21 August 2005. This corresponds to an increased fractal dimension at larger scales.

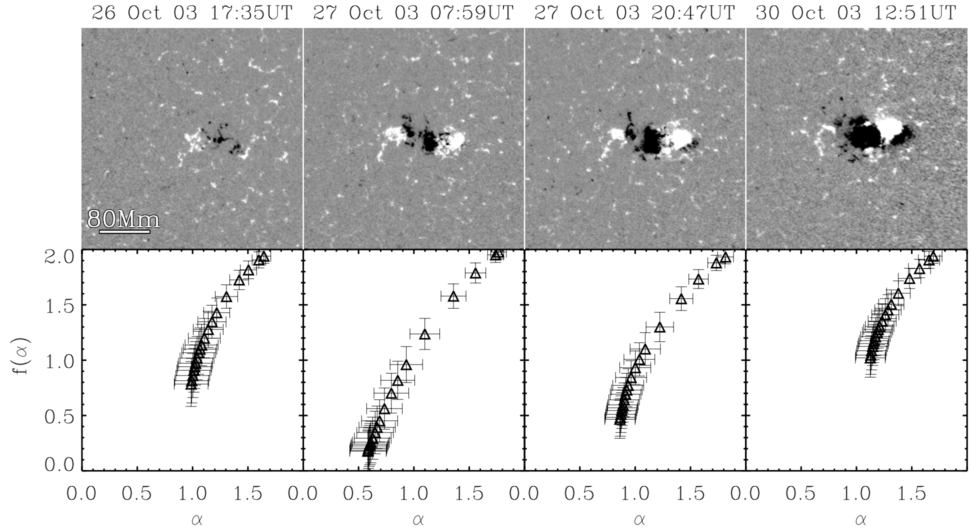

Figure 5.4: (Top) MDI magnetogram images of NOAA 10798 on 18 August 2005 04:47 UT, 18 August 2005 14:23 UT, and 19 August 2005 09:35 UT. (Bottom) The corresponding $f(\alpha)$ spectrum for each date.

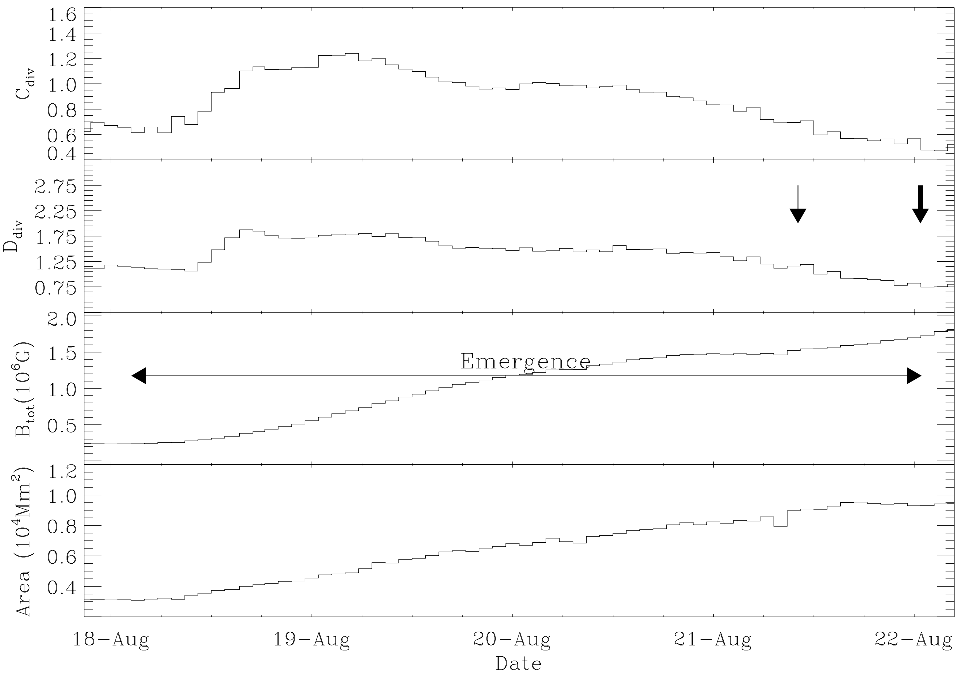

Figure 5.5: NOAA 10798: (top) contribution diversity, (second) dimensional diversity, (third) total field strength (Gauss) and (fourth) area (Mm). Associated C-class flares are indicated by thin arrows, bolder arrows indicate M-class flares.

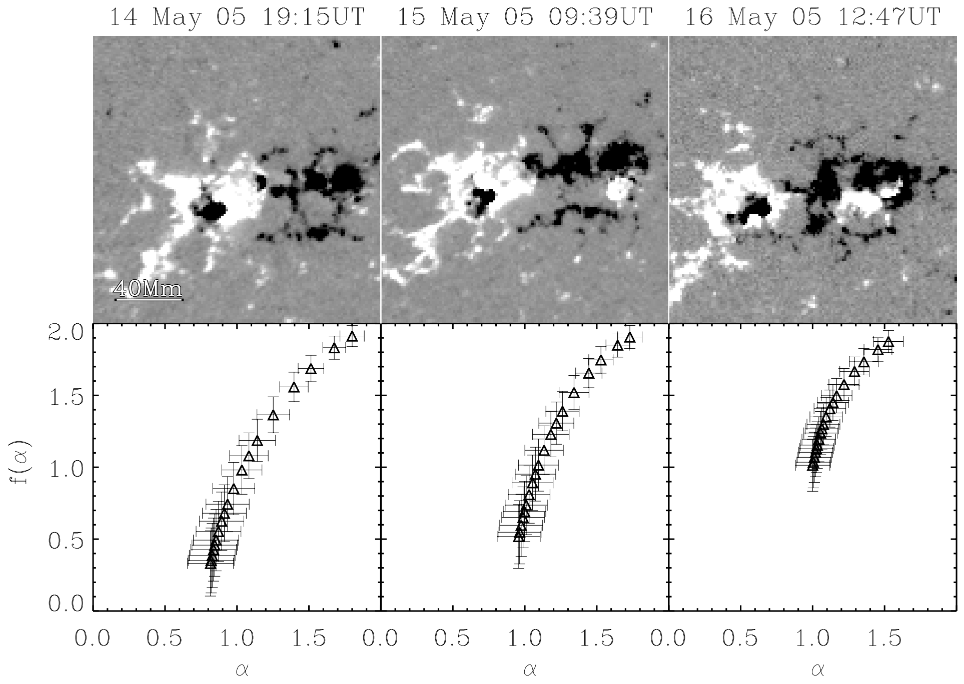

Figure 5.6: (Top) MDI magnetogram images for NOAA 10763 on 14 May 2005 19:15 UT, 15 May 2005 09:39 UT, and 16 May 2005 12:47 UT. (Bottom) $f(\alpha)$ spectra for each date.

5.5.3 NOAA 10763

The emergence of large flux measures in NOAA 10763 is shown in Figure 5.6 and Figure 5.7. As the region grows from 19:15UT on 14 May 2005, an increase in the significance of the larger scales is seen (α_{min}). The dimensional diversity decreases over this time as the complexity of the larger scales increases from a dust like nature ($f(\alpha) \ll 1.0$) to a line like nature ($f(\alpha) \approx 1.0$). The region flares on 15 May 2005 17:35 UT. This corresponds to the formation of a coherent structure with increased fractal dimensions across all scales. An M3.5 flare is observed on 15 May 2005 22:27 UT. Unlike the emergence of flux in NOAA 10488 and 10798, an increase in the multifractal parameters was not present. The emergence in this case occurred in the centre of an already developed region. With this there was no initial increase in the contribution and dimensional diversity. Instead the multifractal parameters decrease steadily as the

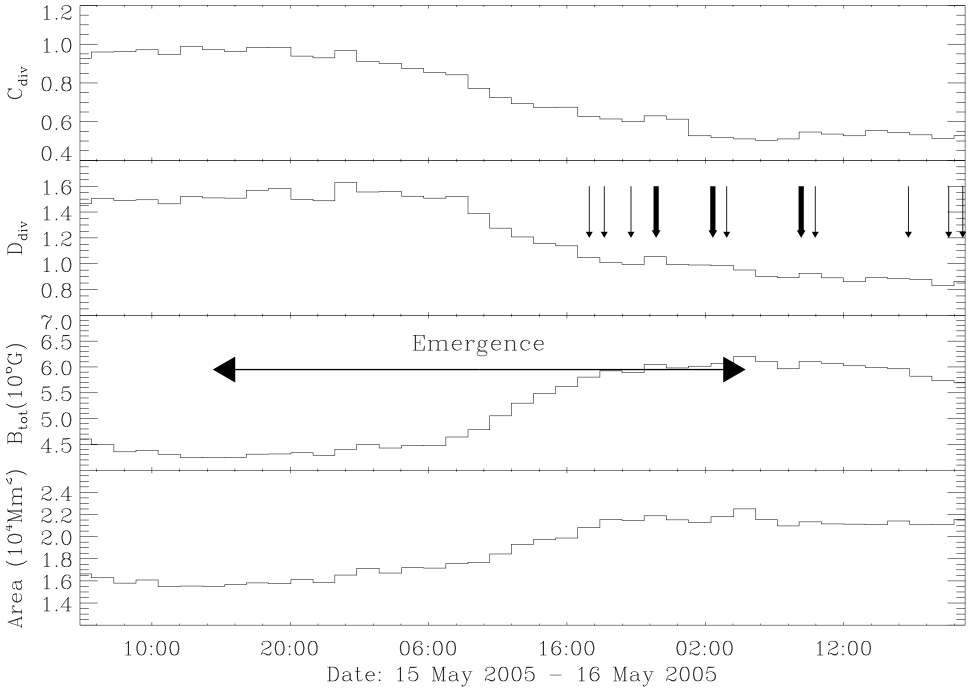

Figure 5.7: NOAA 10763. Contribution diversity (top) and dimensional diversity (second). Total field strength (Gauss) and area (Mm) are shown in third and fourth panels. Associated C-class flares are indicated by thin arrows, bolder arrows indicate M-class flares.

larger scale flux elements grow in significance and complexity.

5.5.4 NOAA 10727

The formation of NOAA 10727 is shown in Figure 5.8 and Figure 5.9. As flux elements emerge and form on the surface, the peak of the singularity spectrum ($q = 0$) can be seen to move to the right (Figure 5.8). This is due to the increased significance of the medium scales across the domain of interest. Similarly to the formation of NOAA 10488, the initial emergence is characterised by an increase in the contribution diversity (C_{div}) and dimensional diversity (D_{div}). This is followed by a decrease in same as the region forms a coherent structure. The emergence of additional large scale flux on 24 January 2005 is shown in Figure 5.9. The fractal dimensions of larger scales ($f(\alpha_{min})$) are seen to decrease as the regions grow, a characteristic which differs from NOAA

10488. NOAA 10727 failed to flare during the time of observation, which may be due to the small fractal dimension of the larger scales ($f(\alpha_{min})$).

5.6 Discussion And Conclusions

The methods of Section 4.3 have been shown to characterise changes in the distribution of active region magnetic fields during the formation and flaring periods. The multifractal spectrum allows for the monitoring of complexity and significance across different scales. The emergence of small flux measures causes a change in the singularity spectrum, as the significance of larger flux measures is reduced. A decrease in the fractal dimension is also seen in the α_{min} region of the $f(\alpha)$ spectrum. As such, sudden changes in the multifractal parameters are an excellent mathematical tool for detecting characteristic changes in active regions.

A correlation between region flaring and decreases in the breadth of the multifractal parameters was evident. This corresponds with the results of Abramenko (2005b), where a significant difference in the multifractality, (Δh), was found between flaring and non-flaring regions. For non-flaring regions, the larger moments of magnetic flux have a significantly lower fractal dimension ($f(\alpha)$), corresponding to a reduced complexity or fill-factor at this scale. A sudden change in the structure of active regions, as evident in the increased fractal dimensions across all scales, might represent a critical transition for an active region as it begins to flare. This further indicates that active regions have to grow in complexity and size before flaring, corresponding with the SOC nature of active regions.

The work of McAteer *et al.* (2005a) found a weak correlation between active region flaring and mono-fractal scaling. As shown active regions are highly complex structures, with several processes across a spectrum of scales contributing to their multifractal structure. By using multiscale/multifractal methods we can separate the different process within the range of scales given by q. Mono-fractal analysis of active regions returns only the Hausdroff dimension within this multifractal structure. Therefore the previous study of McAteer *et al.* (2005a) was restricted in its analysis by looking at only one scale. We plan to preform a similar study to McAteer *et al.* (2005a), on the correlation between active region flaring and multifractal properties. Such large scale statistical studies are needed to justify the inclusion of any parameter of solar active regions in space weather predictions.

We have shown that multifractal methods have the ability to detect characteristic changes in active regions. Coupling this technique with the results of Hewett *et al.* (2008), into power law spatial scaling, would provide a more complete analysis tool for the detection of extreme solar events.

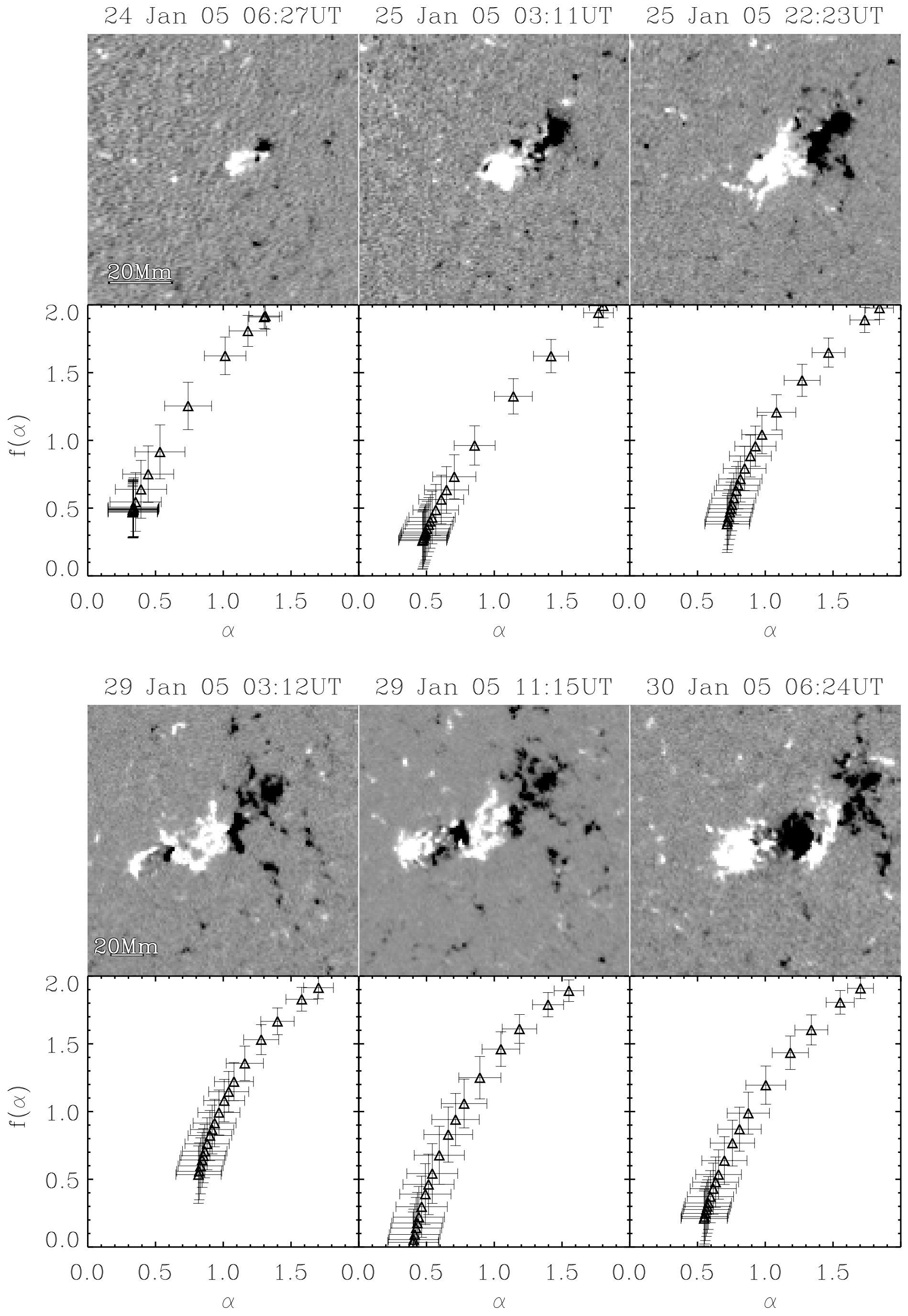

Figure 5.8: (Top) The emergence of NOAA 10727 MDI magnetogram on 24 January 2005 06:27 UT, 24 January 2005 03:11 UT, and 25 January 2005 22:23 UT. (Second panel) The corresponding $f(\alpha)$ spectra for each image. (Third panel) MDI magnetogram on 29 January 2005 03:12 UT, 29 January 2005 11:15 UT and 30 January 2005 06:24 UT. (Bottom) The $f(\alpha)$ spectra for each magnetograms.

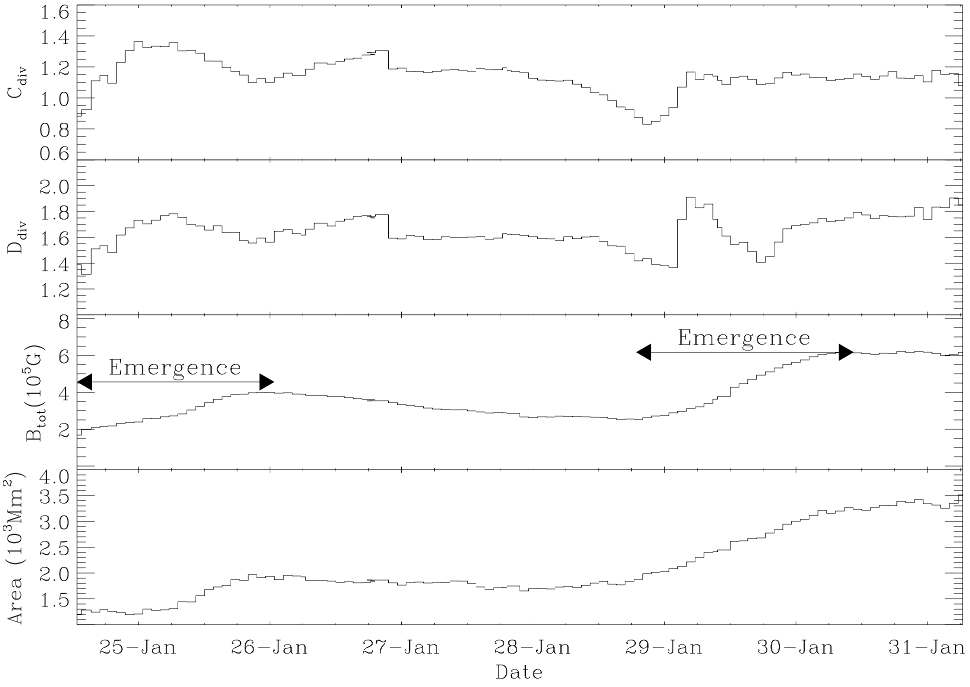

Figure 5.9: The evolution of NOAA 10727: Contribution diversity (top) and dimensional diversity (second). Total field strength (Gauss) and area (Mm) are shown in the third and fourth panels. There was no flares associated with NOAA 10727

6

Complexity Of Active Region Photospheric Fields Using The WTMM Method

In this chapter we study the multifractal nature of magnetic features on the solar surface using a wavelet transform modulus maxima method (WTMM). This is based on research published in Conlon *et al.* (2009); Kestener *et al.* (2009). The WTMM method provides an adaptive space-scale partition of the fractal distribution, from which one can extract the $\tau(q)$ and $D(h)$ multifractal spectra. The multifractal nature of magnetic features for both quiet and active regions on the Sun is obtained. We describe the implementation of an image processing segmentation procedure in the wavelet skeleton space which allows the separation of the information corresponding to the multifractal spectrum of an active region from the surrounding quite Sun texture. The use of a segmentation procedure allows us to accurately study the evolution of active region multifractal parameters for a possible correlation with flaring events. It is shown that prior to an active region flaring the magnetic field undergoes restructuring as Dirac-like features ($h = -1$) coalesce to form step-functions ($h = 0$). The resulting configuration has a higher concentration of gradients along a single neutral line and is a more favourable environment for flaring.

6.1 Introduction

The WTMM method replaces the boxes from the traditional box-counting method with wavelets, which act as fuzzy boxes and are defined for both finite and discrete domains and are better suited for real data sets. Application of the so-called WTMM method to 1D signals have already provided insight into a wide variety of problems e.g. fully-developed turbulence, financial markets, meteorology, physiology, and DNA sequences (Arneodo *et al.*, 1995a; Bunde *et al.*, 2002). The WTMM method has been generalised to 2D for multifractal analysis of rough surfaces and associated physical systems (Decoster *et al.*, 2000; Kestener *et al.*, 2001; Roux *et al.*, 2000b) and to 3D turbulence dissipation data (Kestener & Arneodo, 2004).

In order to examine the self-similarity and complexity of active regions many authors have used the box-counting technique to examine the fractal dimension of active regions (Conlon *et al.*, 2008; McAteer *et al.*, 2005a). McAteer *et al.* (2005a) examined 10^4 active regions and found a low threshold for M/X-class flares as a necessary but insufficient signature of flare production. Conlon *et al.* (2008) similarly used a modified box-counting technique to examine the multifractal properties of evolving active regions. They found that as a region developed towards a state favourable to flaring, there was a decrease in the breadth and height of the multifractal spectrum. An additional method used to examine the fractal and multifractal properties of active regions is the *structure function* (Abramenko *et al.*, 2008; Abramenko, 2005a). A structure function is defined as a statistical moment of the increments of a field and measures its associated intermittence. Abramenko *et al.* (2008) have shown that their is a relation between systematic changes in the ratio of certain powers of the structure function at both the photospheric and chromospheric level. Georgoulis (2005; 2008) examined the ability of these methods to predict solar flares and the eruption parameters of solar active regions. They highlighted the problems such methods have as predictive tools but support their use as analytical tools for the understanding of the fundamental processes involved in the formation and evolution of active regions. The authors add that the multifractal analysis of Abramenko (2005a) shows a greater sensitivity to flaring regions. Each method faces several problems when dealing with the data presently available. Box-counting methods are threshold-dependent and numerical errors combined with poorly resolved data can result in enlarged errors for large and negative q values (Conlon *et al.*, 2008; Georgoulis, 2005). The structure function by definition is unable to examine the multifractal nature of active regions for negative q values. In order to overcome these problems the more stable and reliable wavelet transform modulus maxima (WTMM) method is used in this paper to examine the fractal properties of solar magnetogram data.

This work expands the WTMM method to the study of magnetic features on the Sun. A theoretical example of segmentation in wavelet-transform space is presented. The distribution of gradients across scale is analysed for both quiet Sun and active region type magnetic features to determine an accurate threshold for the segmentation procedure. Additionally, the multifractal properties of the quiet Sun are analysed. The WTMM method is used to analyse a series of magnetogram images of various active regions, so as to investigate any possible relation between the fractal and multifractal properties and flaring potential.

6.2 Observations

For the purpose of this work a series of magnetograms have been analysed to examine the difference in fractal properties between quiet and active solar regions. A series of magnetograms, twenty nine in total, representative of the quiet Sun were taken from the 21 to the 22 December 2006 and a similar series of 28 images representative of the active Sun were taken from the 27 to the 29 October 2003.

A series of magnetograms have been analysed to examine the differences in fractal properties between flaring and non-flaring active regions. A total of six active regions were analysed as they evolved on the solar disk, National Oceanic and Atmospheric Administration (NOAA) 10488, 9878, 10763, 10942, 10954, and 10956. Pre-processing was not performed on these magnetograms so as not to adversely affect the results of the multifractal analysis. Additionally, following an MDI data set upgrade the redistribution of magnetic flux densities as suggested by Berger & Lites (2003) were no longer needed. However, for the calculation of an active regions physical parameters a number of methods were applied to each magnetogram to reduce the projection effects on magnetic field strength and area (Conlon *et al.*, 2008; McAteer *et al.*, 2005a).

6.2.1 A Complete Example Of Segmentation Using The WTMM Method Applied To Theoretical Data

In the study of biomedical images, the 2D WTMM method was adapted and used in cell biology to perform a rigorous and automatic segmentation of chromosome territories from the cell nucleus background (Caddle *et al.*, 2007; Khalil *et al.*, 2007). For the study of digitised mammograms, the 2D WTMM method was used to develop a fractal-based segmentation of micro-calcification clusters from breast tissue background (Kestener *et al.*, 2001). This latter approach is perfectly suited for the present analysis. This section shows how the space-scale partitioning provided by the WT skeleton enables

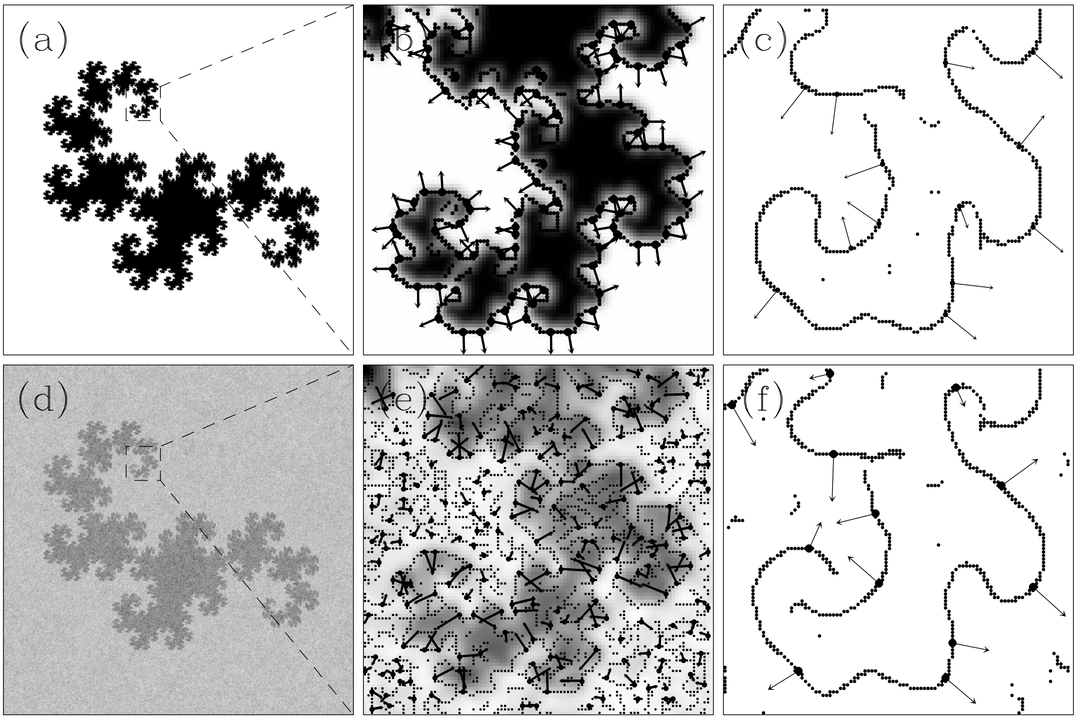

Figure 6.1: (a) The fractal Dragon curve (1024×1024). (d) The Dragon curve embedded into a fractional Brownian noise with a Hurst exponent $H = -0.7$. Note that the noise amplitude is twice the Dragon curve amplitude. (b) (resp. (e)) WTMM lines at smallest scales in a small 100×100 region for the dragon curve (resp. Dragon curve with a fractional Brownian noise background). (c) and (f) same as in (b) and (e) for scale $a = 2\sigma_W$. In (b) and (e) the background image is the smooth-convoluted image $\phi_{\mathbf{b},a} * f$ at scale $a = \sigma_W$. The black arrows represents the WT vectors $\mathcal{M}_\psi$ at the WT skeleton locations.

us to separate the information corresponding to different fractal objects in an image. This allows the self-similar properties of an active region to be separated from the surrounding quiet Sun texture, which has a different roughness and fractal dimension.

Consider an academic example:the fractal Dragon curve [1] with a fractional Brownian noise. The fractal Dragon curve is a self-similar curve defined as the limit set of an iterated function (the Lindenmayer system). It is the same type as the functions used to generate the Sierpinski gasket and the Koch curve. A sample Dragon curve is shown in Figure 6.1(a). Figure 6.1(b) shows the same Dragon curve surrounded by the fractional Brownian noise. The two components have known mono-fractal type self-similar proper-

---

[1] http://en.wikipedia.org/wiki/Dragon_curve

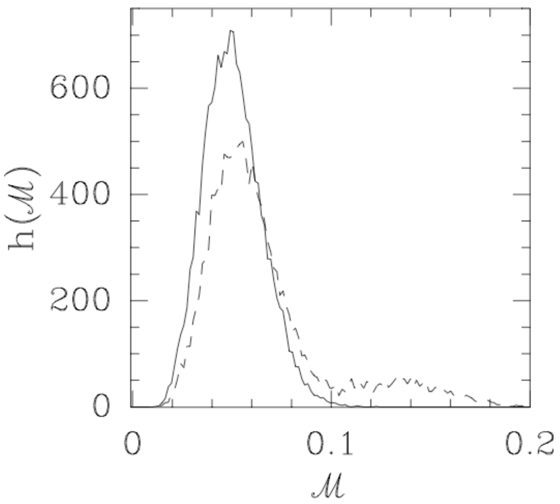

Figure 6.2: Histograms of the values of the wavelet transform modulus $\mathcal{M}_{\psi}[f](\mathbf{b}, a)$ at the smallest scale for the images shown in Figure 6.1(a) and (d). These histograms are constrained with using points that belong to a vertical line of the wavelet transform skeleton. The connected curve is the histogram corresponding to the fractional Brownian noise used to generate image shown in Figure 6.1(a) and the dashed curve to image Figure 6.1(d).

ties, i.e. a singularity spectrum degenerated to a single point: ($h = -0.7$, $D = 2$) for the fractional Brownian noise and ($h = 0$, $D = \log_2(1 + \sqrt[3]{73 - 6\sqrt{87}} + \sqrt[3]{73 + 6\sqrt{87}}/3) \simeq 1.5236$) for the boundary of the Dragon curve. The roughness $H = -0.7$ of the fractional Brownian noise was chosen to reflect the texture of the quiet Sun images as discussed in section 6.3. Figure 6.1(b) and (e) illustrate the results of the computations of the WT maxima chains at the smallest scale; the arrows correspond to the WT vectors $\mathcal{M}_{\psi}$ at the WT skeleton locations. Figure 6.1(c) and (f) show the maxima lines at a scale twice as large as in Figure 6.1(b) and (e).

In Figure 6.2 the histograms of the values of the WT modulus $\mathcal{M}_{\psi}[f](\mathbf{b}, a)$ at the smallest scale for the images shown in Fig. 6.1(a) and (d) are presented. These histograms are computed only with locations from the corresponding WT skeletons. The dashed curved histogram, computed from the noisy Dragon image shows two populations: modulus values below 0.1 are mainly associated with the noise structures whereas above 0.1 the modulus values represent step-like structures of the Dragon boundary.

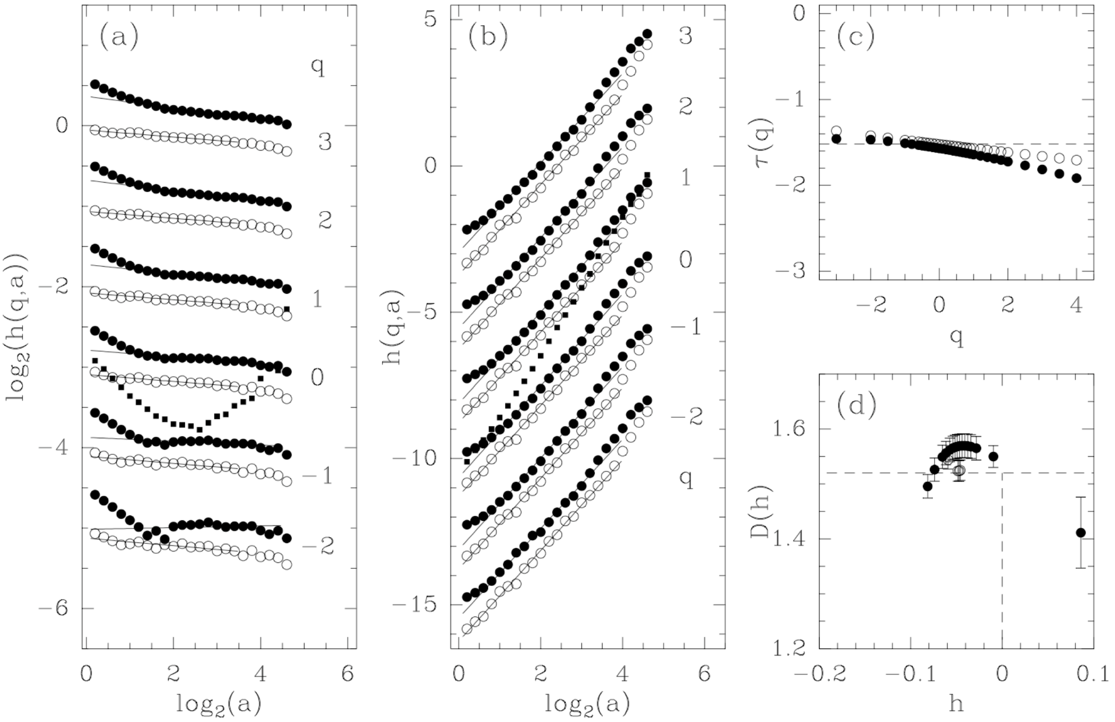

Figure 6.3: Multifractal analysis of the fractal Dragon curve (○) and the noisy Dragon curve (●) after the segmentation step. (a) $h(q,a)$ vs $\log_2 a$ for different values of q; the solid lines are the linear regression lines over the range of scales $[0,4]$ (resp. $[0.5,3.5]$) for the Dragon curve (resp. the noisy Dragon curve after segmentation). The (■) curve is the $h(q=0,a)$ partition function of the noisy Dragon curve without any segmentation. (b) $D(q,a)$ vs $\log_2 a$. (c) $\tau(q)$ vs q. The dashed horizontal line is the theoretical $\tau(q)$ spectrum of the boundary of the Dragon curve. (d) $D(h)$ vs h, the dashed lines have the same meaning as in (c). Only error bars on D are shown.

Investigating the shape of the WT modulus histograms at the smallest scale provides a threshold value to separate the maxima lines of the WT skeleton into two populations and then analyse the corresponding self-similar properties.

The application of the segmentation procedure, at a threshold of 0.12, allows for the recovery of the true multifractal parameters, as outlined in Figures 6.3(a) and (b). A smaller threshold value does not completely remove the noisy structure as highlighted in Figure 6.4. Figure 6.3(a) shows that even after the segmentation procedure, the partition function $h(q,a)$ of the noisy Dragon image is still curved below a scale of $\log_2 a = 1$. However, a well defined scaling behaviour over three octaves is displayed, compared to the four octaves for the dragon curve data alone. The $h(q = 0, a)$ partition function of the noisy Dragon without the application of the segmentation procedure is plotted with the symbol (■) for comparison.

As has been shown, without the segmentation procedure the partition function is a mixture of different self-similar behaviours. As such, reliable quantitative information cannot be extracted without the use of the segmentation procedure. Figure 6.3(c) and (d), show the $\tau(q)$ and $D(h)$ spectrum. The slight departure from monofractality displayed by the $D(h)$ curve for the segmented noisy Dragon data, can be understood as an effect of the smaller statistics. Indeed this can be seen in the fewer lines that remain in the WT skeleton after the segmentation procedure, see Figure 6.2. Even with fewer WT maxima lines a good estimate of the fractal dimension of the segmented Dragon curve, $D_F = 1.57 \pm 0.03$, is obtained at the top of the $D(h)$ curve. Finally, Figure 6.4 is a 3D visualisation of the maxima chains in $(x, y, scale)$ space of the noisy Dragon after removing maxima chains that do not contain at least one maxima line with a WT modulus at smallest scale above the threshold. Thus the removal of small scale features that would otherwise adversely affect the multifractal analysis is achieved using the proposed segmentation method.

6.3 Quiet Sun Multifractal Properties

An example of the quiet and active MDI magnetograms analysed is shown in Figure 6.5 (top), with a histogram of the wavelet transform modulus $\mathcal{M}_{\psi}[f](\mathbf{b}, a)$ at the smallest scale (bottom). Active regions result from an increased proportion of large magnetic elements of opposite polarity forming in close proximity to each other. The resulting neutral or magnetic inversion lines can be detected using standard wavelet-based techniques (Ireland *et al.*, 2008). As such, active regions should contain a greater number of higher magnitude WT gradients. This is shown in Figure 6.5 (bottom), which sug-

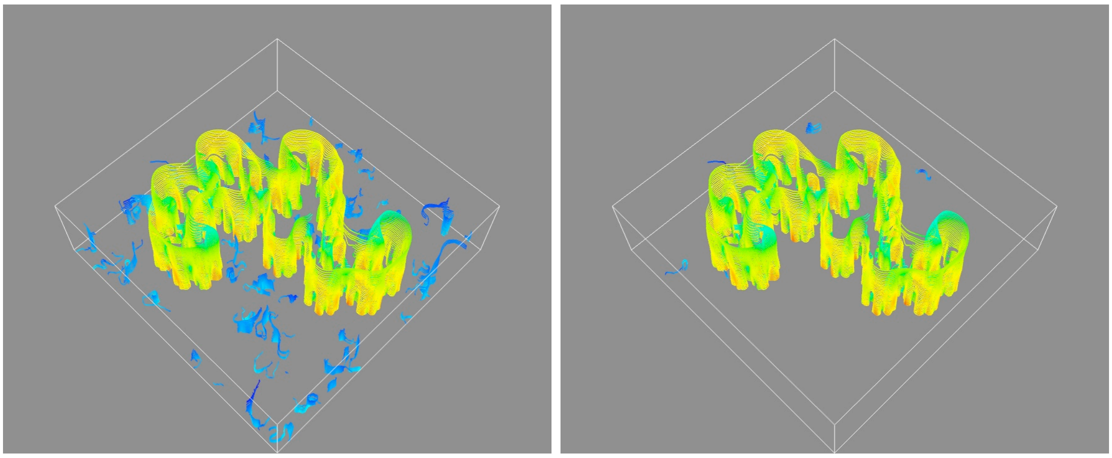

Figure 6.4: 3D visualisation in the space-scale $(x, y, scale)$ representation of the WTMM edges computed from the image shown in Figure 6.1(d) after the segmentation procedure with two different values of the WT modulus threshold. The segmentation consists in removing all the maxima lines such that the WT modulus at the smallest scale is above a given threshold. Here are displayed all the multiscale edges containing at least one maxima line belonging to the resulting skeleton. On the left (resp. right) are shown the WT multiscale edges with a threshold value on WT modulus of 0.1 (resp. 0.12). The values of the threshold are chosen to extract at best a sub-skeleton specific to the embedded dragon curve. See Fig. 6.2 for the histogram of the WT modulus values at smallest scale.

gests that moduli with strengths larger than 40 are unlikely in quiet Sun magnetograms. Due to the different self-similar behaviours of active regions and their surrounding quiet Sun, we segment the selection of WT skeletons above a threshold of 40. As outlined in Section 6.2.1, this will allow for the study of the multifractal properties of active regions in a quantitative manner.

The results of the computation of the multifractal spectra when averaging the partition functions over a set of 30 (505×505) quiet Sun images without applying the segmentation are shown in Figure 6.6. As shown in Figure 6.6(a) and (b), $h(q, a)$ and $D(q, a)$ (Equations (4.21) and (4.22)) display scaling behaviour over almost four octaves, when plotted versus $\log_2 a$, for $q \in [-2, 3]$ (symbol $\circ$). Linear regression fits of the data yields the non-linear $\tau(q)$ spectrum shown in Figure 6.6(c). This multifractal diagnosis can also be observed in Figure 6.6(a) where the slope $h(q)$ of partition function $h(q, a)$ versus $\log_2 a$ depends on q. The corresponding multifractal spectrum

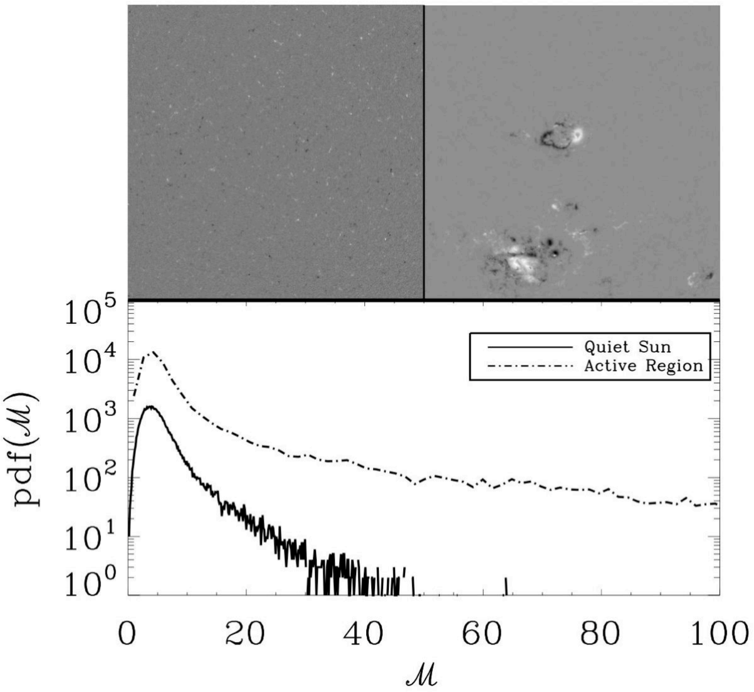

Figure 6.5: (Top, Left) MDI magnetogram taken 20 December 2006, (Top, Right) MDI magnetogram taken 28 October 2003. (Bottom) Histogram values of the wavelet transform modulus $\mathcal{M}_{\psi}[f](\mathbf{b},a)$ at the smallest scale for MDI magnetogram images of a quiet Sun (solid) and active Sun (dashed).

$D(h)$ is shown in Figure 6.6(d) (symbol •)). From the top of the $D(h)$ curve, we can see that quiet Sun images are everywhere singular ($D = 2$ at the top) with an average Hölder exponent of $h \sim -0.75$. The multifractality can be quantified by how large the $D(h)$ curve is; when using the log-normal model, $D(h)$ can be fitted with a parabola $D(h) = C_0 - (h + C_1)^2/2C_2$, where $C_0 \sim 2$, $C_1 \sim -0.75$ and $C_2 \sim 0.22$ is the intermittency coefficient.

In order to understand the source of this intermittency, a threshold was imposed on each MDI magnetogram of the quiet Sun Figure 6.7. The threshold operation has the effect of removing large magnetic features resting on the super-granular structures of the Sun. In Figure 6.6(d), we can see that the multifractality of the threshold quiet Sun image set is strongly reduced but not cancelled. We can also note that the

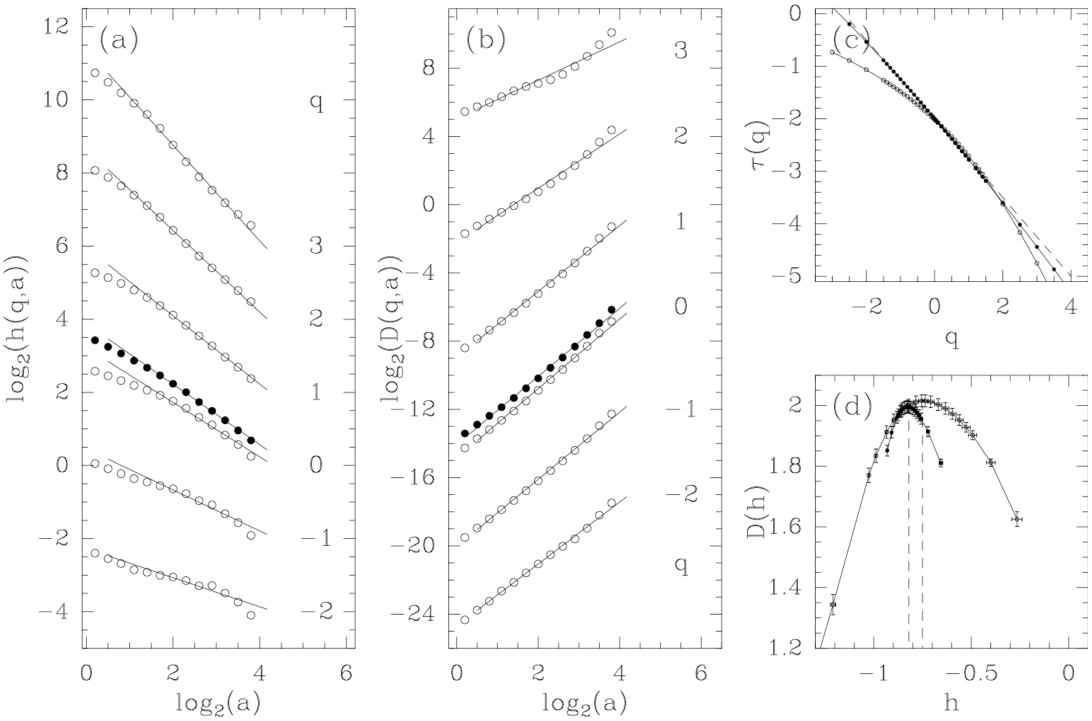

Figure 6.6: Multifractal analysis of a set of 30 quiet Sun images (505×505) (○) and the thresholded images (●). (a) $h(q, a)$ vs $\log_2 a$ for different values of q; the solid lines are the linear regression lines over the range of scales $[0, 3.7]$. The (■) curve is the $h(q = 0, a)$ partition function of the threshold quiet Sun images. (b) $D(q, a)$ vs $\log_2 a$. (c) $\tau(q)$ vs q. The dashed straight line is the theoretical linear $\tau(q) = -0.75q - 2$ spectrum of the boundary of Brownian motion images with Hurst exponent $H = -0.75$. (d) $D(h)$ vs h, the dashed lines locate the position of the top of $D(h)$ curves. Error bars on D and h are shown.

average Hölder exponent is slightly shifted from −0.75 to −0.82, and the intermittency coefficient is reduced to $C_2 \sim 0.06$.

Without the super-granular magnetic structure the quiet Sun multifractal spectrum is shown to be more noise-like (Hölder exponent close to −1) and more monofractal (reduced C_2). Therefore it can be assumed that the magnetic features resting on the super-granular structure are the cause of the quiet Sun multifractal spectrum. Additionally the quiet Sun multifractal signature is distinct from that of active regions, with a fractal dimension or $D(h)$ of 2 and a Hölder exponent no greater than −0.75.

These results demonstrate that the photosphere is a combination of two distinct

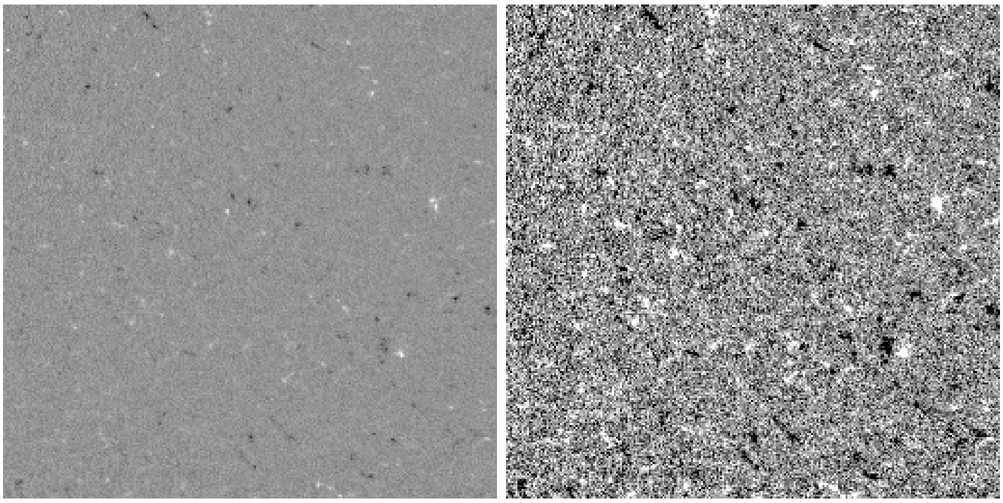

Figure 6.7: 256×256 Quiet Sun images. Image on the right is a thresholded version of the left one. Pixels with large absolute magnetic flux are shrinked down. Multifractal properties of quiet Sun images and the corresponding thresholded versions are shown in Figure 6.6.

fractal processes. Current models for the solar dynamo use information on the fractal dimension of solar disk as a whole (Pontieri *et al.*, 2003). As such, the additional information on the fractal and multifractal processes evident on the photosphere and the characteristic make-up of the quiet Sun should be incorporated into any further theoretical work.

6.4 Evolving Active Regions

The results presented here are for an active region fractal dimension and its associated Hölder exponent. These present a single point, $q = 0$, on the multifractal $D(h)$ versus h curve. This was done as an initial investigation into the power and ability of the WTMM method to characterise changes in the magnetic structure of active regions.

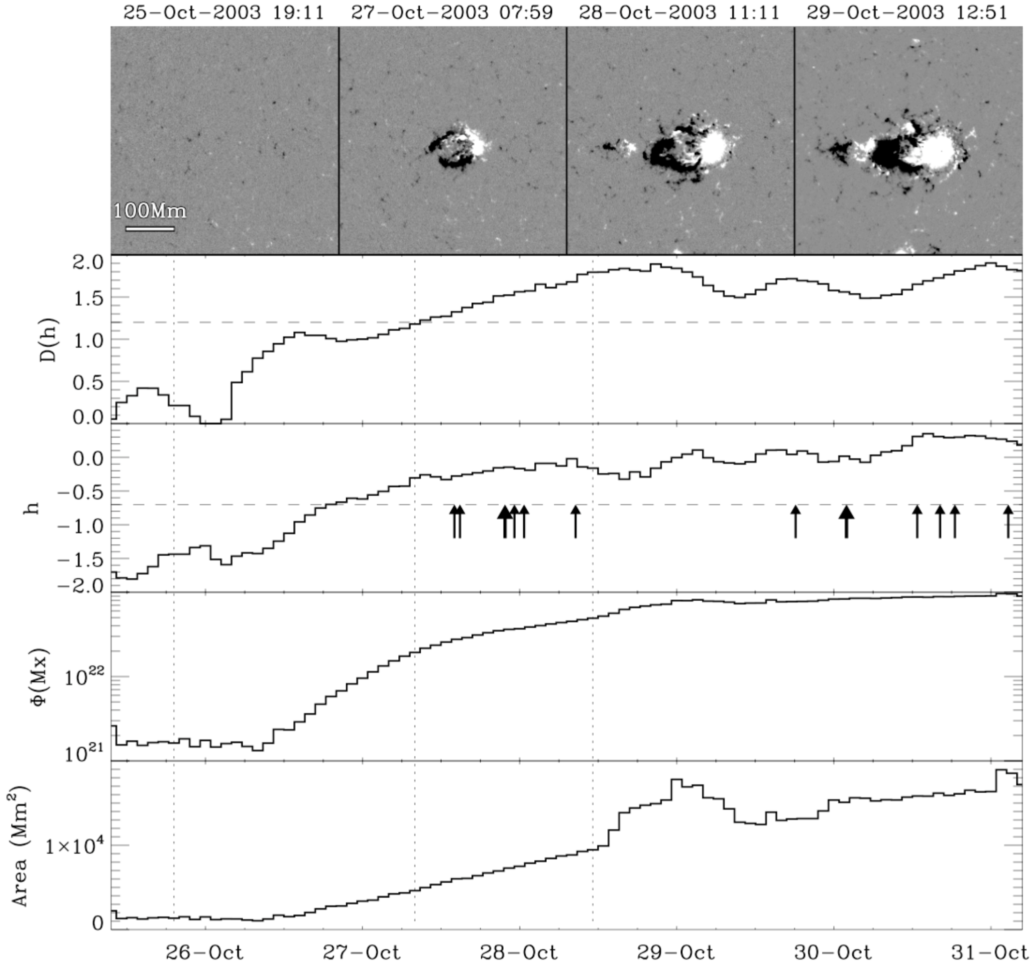

Figure 6.8: The evolution of NOAA 10488. (Top panel) MDI magnetogram image for NOAA 10488 on 25 October 2003 at 19:11 UT, 27 October 2003 at 07:59 UT, 28 October 2003 at 11:11 UT and 29 October 2003 at 12:51 UT. (Second panel) $D(h)$ for $q = 0$. (Third panel) h for $q = 0$. (Fourth panel) The total unsigned magnetic flux (Mx). (Bottom panel) Total area (Mm^2). Associated C-class flares are indicated by thin arrows; bolder arrows indicate M-class flares. Vertical dotted lines indicate the time of MDI magnetograms in the regions evolution. Dashed horizontal line in the first panel highlight a previously proposed threshold for flaring (McAteer *et al.*, 2005a). Dashed horizontal line in the second panel shows our proposed threshold.

6.4.1 NOAA 10488

NOAA 10488 emerged onto the solar disk on the 26 October 2003 and continued to grow rapidly until the 29 October 2003. The ability of the segmentation methods to detect the presence of active regions in quiet Sun data is highlighted by the rise in $D(h)$ and h prior to the increase in the other physical parameters, Figure 6.8. Prior to the regions emergence only a limited number of WT moments exceed the threshold, resulting in $D(h)$ and h values that would characterise poorly resolved *dusty* data. As the region forms and develops into a coherent structure the fractal dimension and Hölder exponent rise steadily.

While on disk NOAA 10488 underwent two flaring periods. The first occurred over an eighteen hour period starting at 14:02 UT on the 27 October 2003 and contained five C-class flares and a M1.9 flare. The second started at 18.10 UT on the 29 October 2003, lasted for two days and resulted in 8 C-class flares and two M-class flares. As the region evolves the $D(h)$ or fractal dimension is seen to grow as the region forms large two-dimensional like structures. In addition flaring periods are associated with an observably higher Hölder exponent and a fractal dimension exceeding the threshold proposed by McAteer *et al.* (2005a). An increased Hölder exponent suggests a reorganisation of the underlying magnetic field[1]. As the Hölder exponent of the region increases, Dirac-like gradients are replaced by more structured step function-like gradients. The formation of large structured gradients in the region allows for the storage and release of large amount of free magnetic energy.

6.4.2 NOAA 10763

NOAA 10763 came into view on the 12 May 2005. On disk it experienced an increase in both area and magnetic flux from the 15 May 2005 until the 16 May 2005. Around this time the region began to flare with the release of twelve C-class and four M-class flares. Similarly to NOAA 10488 the regions flaring period is associated with a fractal dimension greater than 1.2 for all M-class flares and the majority of the C-class flares.

The most significant changes are again seen in the regions Hölder exponent (h). The

---

[1] $h = -1$ corresponds to Dirac white noise, $h = 0$ a step function and $h = 1$ a smooth differential function.

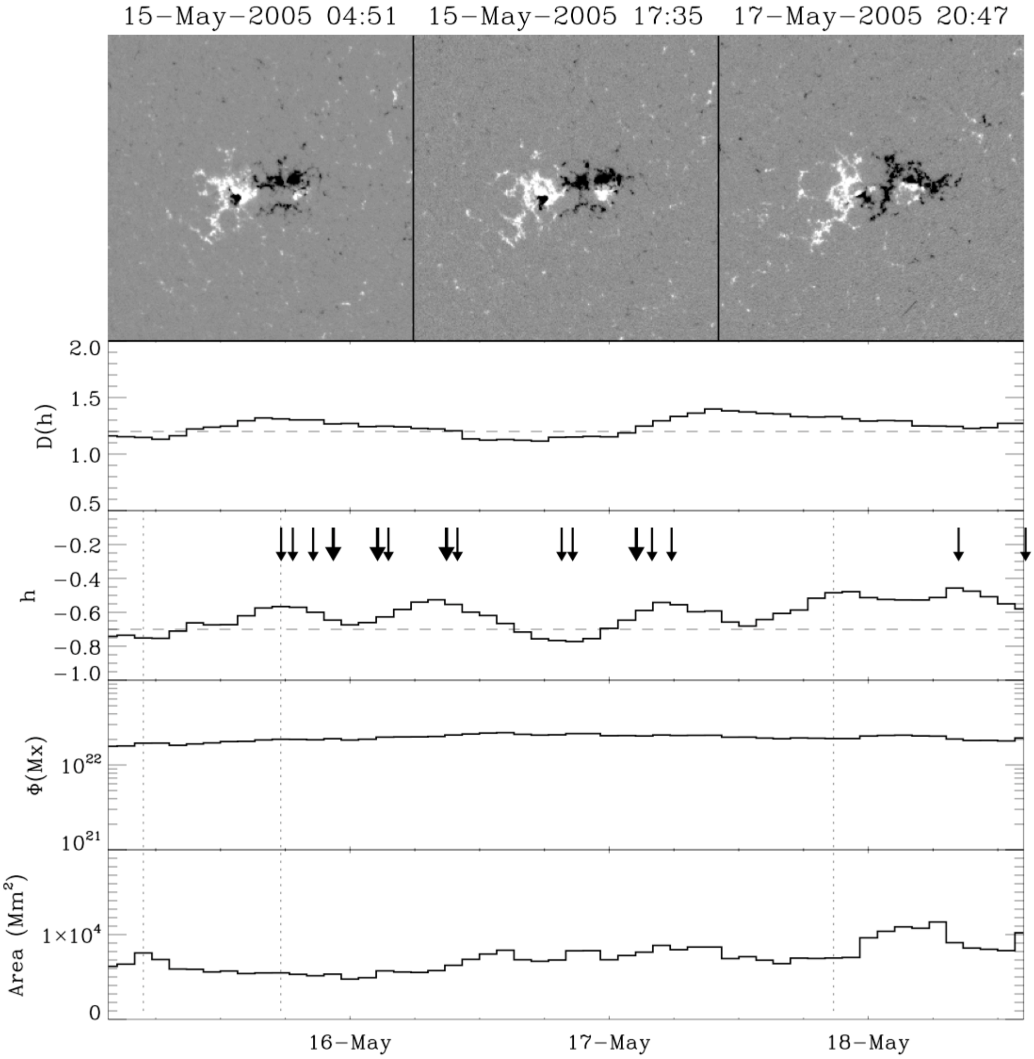

Figure 6.9: The evolution of NOAA 10763. (Top panel) MDI magnetogram image for NOAA 10763 on 15 May 2005 at 04:51 UT, 15 May 2005 at 16:35 UT and 17 May 2005 at 20:47 UT. (Second panel) $D(h)$ for $q = 0$. (Third panel) h for $q = 0$. (Fourth panel) The total unsigned magnetic flux (Mx). (Bottom panel) Total area (Mm^2). Associated C-class flares are indicated by thin arrows; bolder arrows indicate M-class flares. Vertical dotted lines indicate the time of MDI magnetograms in the regions evolution.

increase in h towards the start of the 16 May 2005 are accompanied by the majority of the regions flares. Two C-class flares occur during a period of a relatively low Hölder exponent. After which the Hölder exponent increases again to accompany the release of an M-class flare. This dip in the Hölder exponent can be understood as a reduction in the amount of magnetic free energy in the region, or the loss of a coherent structure among the gradients present in the region. The subsequent rise in the Hölder exponent or clustering of the gradients in the region into a coherent structure, accompanies the release of a M-class flare.

6.4.3 NOAA 9878

NOAA 9878 rotated onto the solar disk on 22 March 2002 already fully developed. A stable region, with little fluctuations in its area or magnetic flux. This is supported by the near constant fractal dimension which remains above the threshold for flaring until early on the 27 May 2002. The region produced one C-class flare on the 23 March 2002 at 03:13 UT, followed by 4 C-class flares starting at 10:31 UT on the 25 March 2002. Similarly to NOAA 10763 and NOAA 10488 flaring is seen to be associated with a fractal dimension greater than 1.2 and an increase in the Hölder exponent above -0.7. After flaring the Hölder exponent is seen to decrease to quiet Sun levels accompanying the release of magnetic free energy from the region.

6.4.4 NOAA 10954

NOAA 10954 emerged on the 28 April 2007, and moved across the disk before decaying on the 5 May 2007. A small region with a maximum area of $\approx 1.4 \times 10^3$ Mm^2 and total magnetic field strength of $\approx 5 \times 10^{21}$ Mx, Figure 6.11. The region emerged with a large fractal dimension, which decreased while the region decayed. The Hölder exponent approached zero during its initial emergence before decaying to a quiet Sun level. While NOAA 10954 had fractal properties that so far would indicate a possibility of flaring, the region produced no noticeable flares. This would indicate that fractal properties alone are not reliable for the prediction of flares and should be taken into account with other physical properties, such as area and total magnetic field strength.

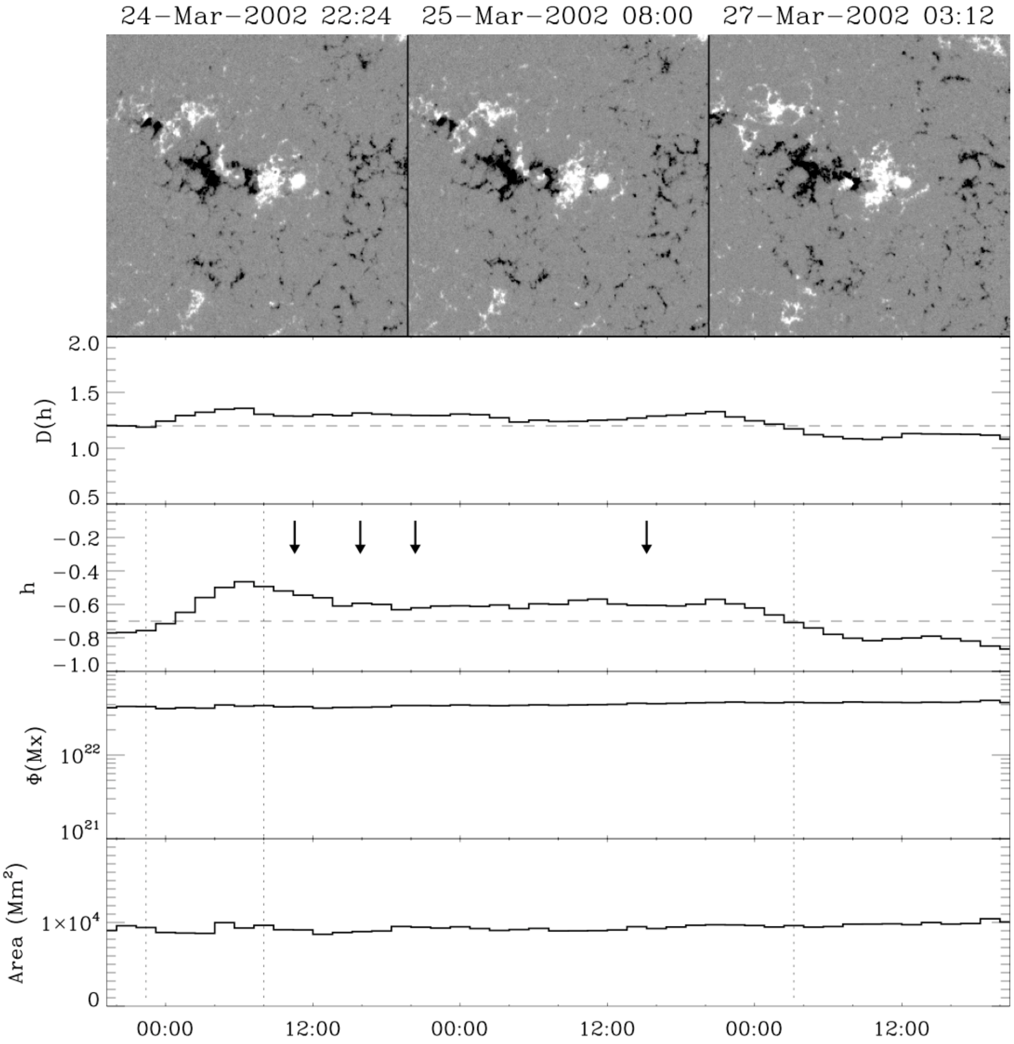

Figure 6.10: The evolution of NOAA 9878. (Top panel) MDI magnetogram image for NOAA 9878 on 24 March 2002 at 22:24 UT, 25 March 2002 at 08:00 UT and 27 March 2002 at 03:12 UT. (Second panel) $D(h)$ for $q = 0$. (Third panel) h for $q = 0$. (Fourth panel) The total unsigned magnetic flux (Mx). (Bottom panel) Total area (Mm^2). Associated C-class flares are indicated by thin arrows; bolder arrows indicate M-class flares. Vertical dotted lines indicate the time of MDI magnetograms in the regions evolution.

6.4.5 NOAA 10942

NOAA 10942 is another small region which emerged on 17 February 2007. It had a maximum area of around 2×10^3 Mm^2 and a field strength of 4×10^{21} Mx, Figure 6.12. The region fractal dimension is relatively small, only exceeding the proposed threshold

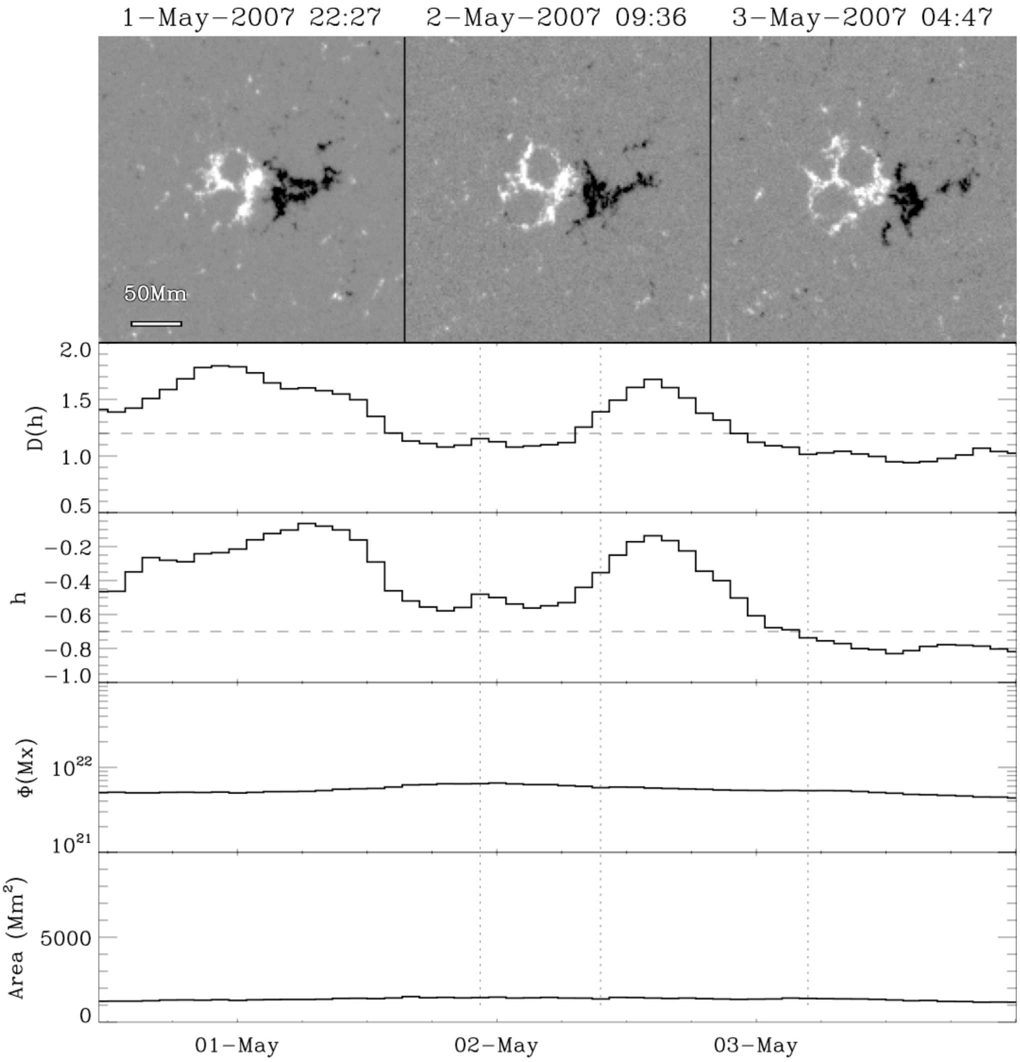

Figure 6.11: The evolution of NOAA 10954. (Top panel) MDI magnetogram image for NOAA 10954 on 1 May 2007 at 22:27 UT, 2 May 2007 at 09:36 UT and 3 May 2007 at 04:47 UT. (Second panel) $D(h)$ for $q = 0$. (Third panel) h for $q = 0$. (Fourth panel) The total unsigned magnetic flux (Mx). (Bottom panel) Total area (Mm^2). Vertical dotted lines indicate the time of MDI magnetograms in the regions evolution. Dashed horizontal lines indicate proposed thresholds for flaring.

for a short time. During this time however the Hölder exponent was very close to the proposed threshold. As with NOAA 10954, it would seem that this region was too small in area and strength to produce flares even when favourable conditions existed.

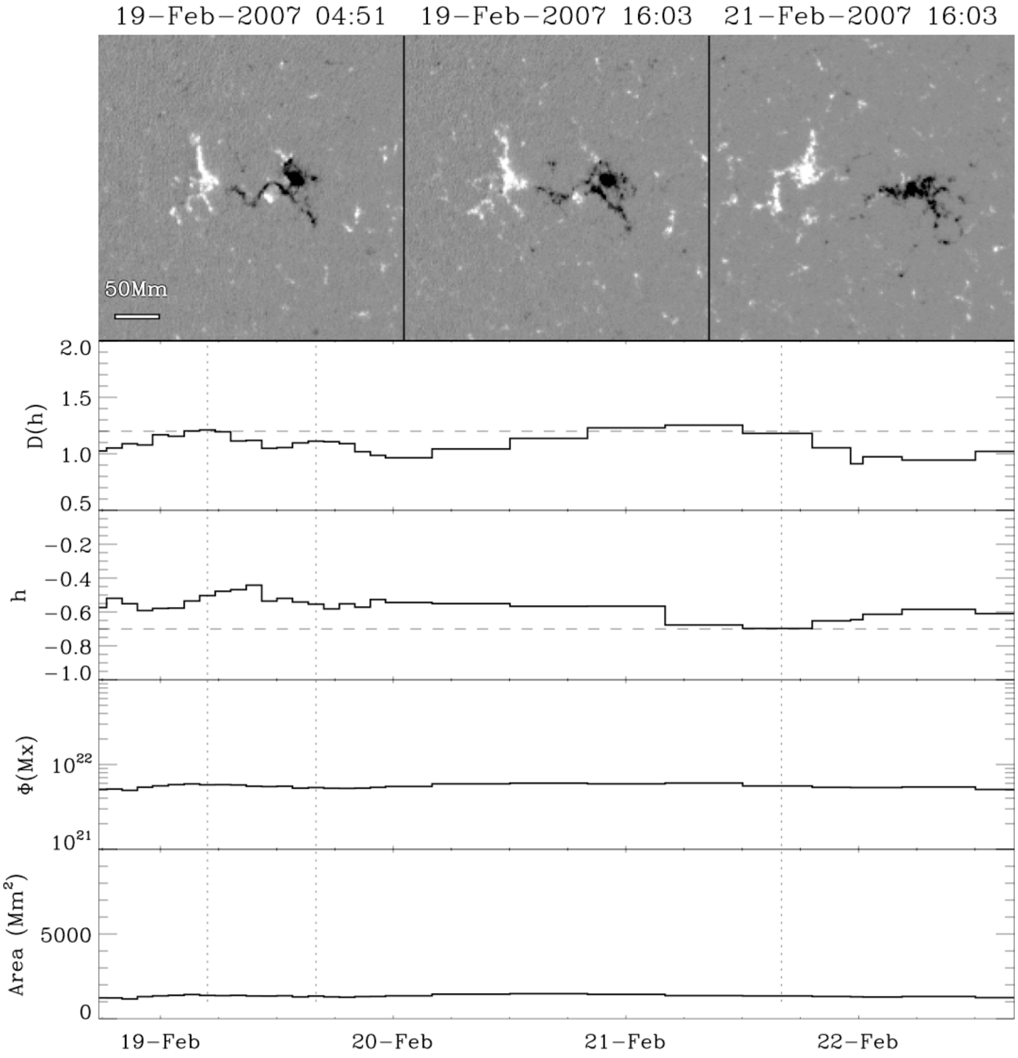

Figure 6.12: The evolution of NOAA 10942. (Top panel) MDI magnetogram image for NOAA 10942 on 19 February 2007 at 04:51 UT, 19 February 2007 at 16:03 UT and 21 February 2007 at 16:03 UT. (Second panel) $D(h)$ for $q = 0$. (Third panel) h for $q = 0$. (Fourth panel) The total unsigned magnetic flux (Mx). (Bottom panel) Total area (Mm^2). Vertical dotted lines indicate the time of MDI magnetograms in the regions evolution. Dashed horizontal lines indicate proposed thresholds for flaring.

6.4.6 NOAA 10956

NOAA 10956 rotated onto the solar disk on the 15 May 2007. Apart from two C-class flares while on the limb, the region produced no flares. The regions magnetic

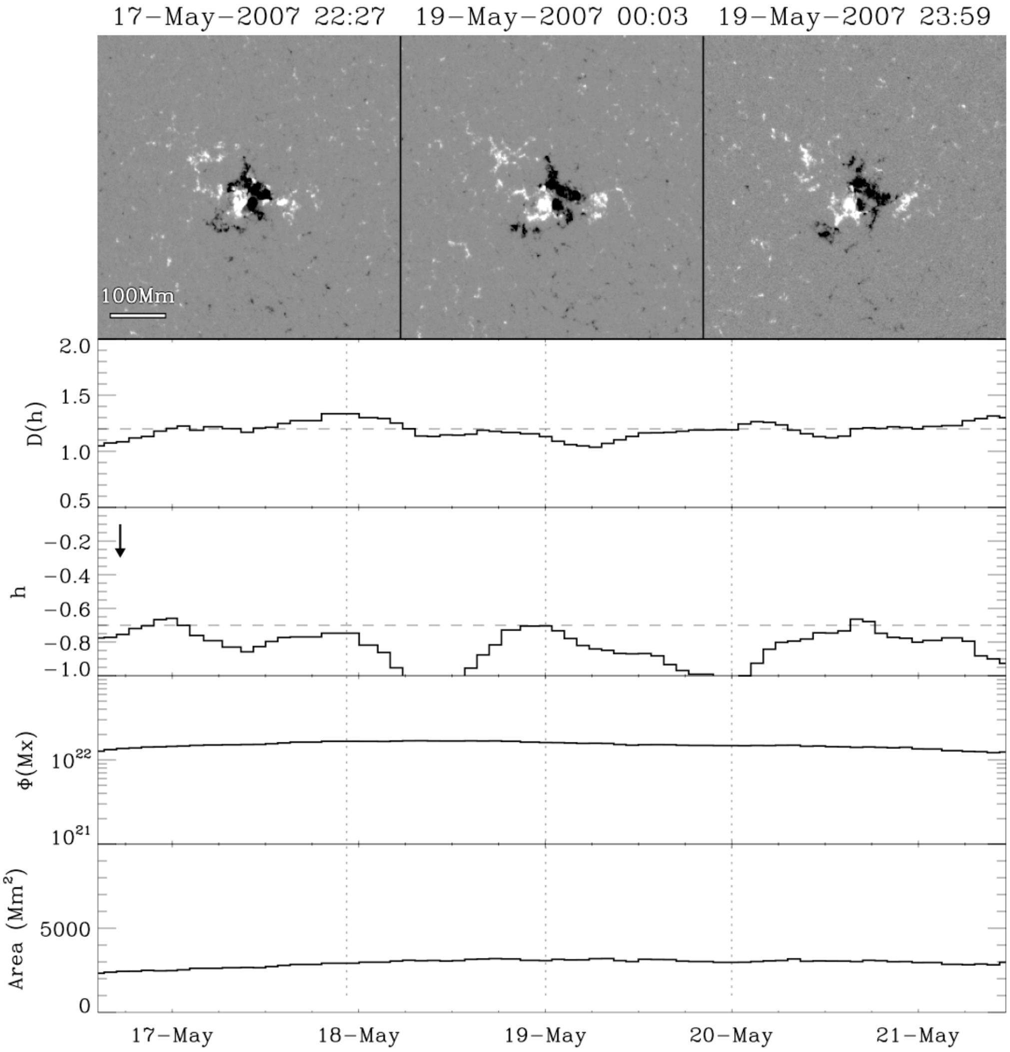

Figure 6.13: The evolution of NOAA 10956. (Top panel) MDI magnetogram image for NOAA 10956 on 17 May 2007 at 22:27 UT, 19 May 2007 at 00:03 UT and 19 May 2007 at 23:59 UT. (Second panel) $D(h)$ for $q = 0$. (Third panel) h for $q = 0$. (Fourth panel) The total unsigned magnetic flux (Mx). (Bottom panel) Total area (Mm^2). The associated C-class flare is indicated by the thin arrow. Vertical dotted lines indicate the time of MDI magnetograms in the regions evolution. Dashed horizontal lines indicate proposed thresholds for flaring.

field strength reached a peak of 1×10^{22} Mx and the area peaked at 3×10^3 Mm^2, Figure 6.13. Given the amount of magnetic flux present in the region it is not possible to rule out flaring based on the regions physical parameters. At no time during the regions time on disk, did neither the fractal dimension of Hölder exponent exceed the proposed thresholds for an extended period of time. This suggests that the field was not structured in a flaring favourable manner during the period analysed.

6.5 Conclusions

Many physical systems analysed using fractal and multifractal techniques are surrounded or embedded in a background or surrounded by instrumental noise. As such these systems are a combination of two statistically distinct structures. This work addressed the need to accurately calculate the multifractal parameters of such complex systems. The presence of multiple structures can result in an inaccurate or skewed calculation of the fractal and multifractal parameters when studied as a whole. Using the segmentation method presented here, it is possible to separate these two processes and accurately recover the fractal or multifractal structure of the system in question. A theoretical example for this method is provided in Section 6.2.1. Figure 6.3, highlights the ability of the WTMM method to allow the accurate recovery of the parameters in question. The removal of information relating to the background noise is highlighted in Figure 6.4.

Multifractal analysis of the quiet Sun data has shown that it is similar in nature to Brownian motion and exhibits a Hölder exponent of -0.75, Figure 6.6. This represents additional information that can be used in the modelling of quiet Sun magnetic fields. Additionally, the histogram plot of WT modulus, shown in Figure 6.5, highlights the statistical difference of active region magnetic fields from that of the quiet Sun. This allows for the separation of active region and quiet Sun features through the application of a threshold in the WT modulus space. The use of a threshold to separate the images in modulus space allows for the study of complexity in active regions separate from the embedded quiet Sun. As such, our results are significantly more stable and robust when compared to previous fractal and multifractal methods. The analysis of solar magnetogram data as a single process would result in the appearance of multifractal features, where there was none, see Section 6.2.1. Along with a limited range of scales over which regression was valid. This work represents a preliminary analysis of solar data using the WTMM method, and has shown it to be a stable and accurate mathematical tool for the analysis of magnetic fields on the solar disk. The results presented here for the analysis of active regions represent one data point in the multifractal spectrum, the so-called fractal dimension or $q = 0$. It should be noted that the WTMM method allows for the calculation and analysis of the full multifractal spectrum and it is planned to examine this in future work.

The results presented in this chapter show a strong correlation between changes in the fractal properties of active regions and their evolution on disk. Similar to the results of McAteer *et al.* (2005a), a lower threshold in of $D(h) > 1.2$ is found to be a *necessary but insufficient signature of flaring.* Also the Hölder exponent has been shown to detect the restructuring of active regions from a field representing Dirac-like gradients towards one closer to step-function-like gradients. Analysis of the quiet Sun magnetogram data has shown that the quiet Sun magnetic fields have a Hölder exponent of -0.7. As such, we propose that a Hölder exponent of no less than -0.7, is an indicator of the conditions favourable towards flaring. Thus if a region is sufficiently large in both area and magnetic field strength, and has a sufficiently high fractal dimension and Hölder exponent the possibility of the region producing high energy flares is greatly increased.

The results presented here are supportive of previous results which have highlighted the ability of multi-scale methods to detect characteristic changes in magnetic elements on the photosphere of the Sun (Abramenko, 2005b; Hewett *et al.*, 2008). In particular, those characteristics associated with a regions ability to produce flares, such as:

- Changes in the *flatness* of structure functions (Abramenko, 2005a).

- The *Dimensional* and *Contribution* diversity of the multifractal spectrum (Conlon *et al.*, 2008).
- Active region fractal dimension (McAteer *et al.*, 2005a).

The work presented here is an improvements on each of these methods and allowed for a more detailed analysis of the processes involved in the evolution of active regions.

Taken together with other physical parameters, the multifractal parameters discussed here may make it possible to detect the restructuring of active region magnetic fields prior to flaring. Further work is needed on a larger set of active regions to fully access the capability of the WTMM method to detect the conditions favourable for flaring and further constrain any thresholds that may or may not exist.

7

Complexity of Active Region Coronal Fields Using Extrapolation Techniques

The 3D magnetic topology of NOAA 10956 is reconstructed using a linear force-free extrapolation. EUVI observations of coronal loop structures are used to constrain the value of α used in the extrapolations. The values of α were used to investigate changes in the connectivity and energy of the magnetic field within the region during its evolution. An emergence of magnetic flux in the region was found to result in significant changes in the region's twist (α), free energy and connectivity. This is based on research published in Conlon & Gallagher (2009).

7.1 Introduction

Extreme solar events such as solar flares and coronal mass ejections (CMEs) originate in the corona of active regions (e.g. Gallagher *et al.* 2007). Flares and CMEs are known to originate in regions of intense magnetic fields as active regions. The structure and evolution of the solar corona is governed by the magnetic field, as it is a low-β plasma (Gary, 2001). An increased understanding of the coronal magnetic field is required to study the dynamics involved in the release of these high energy events.

The methods described in this chapter allow for the 3D structure of the magnetic field of an active region to be recovered and a detailed analysis of its evolution. Observation and the transformation of co-ordinates between reference frames are outlined in Section 7.2. Details of the extrapolation method and cost function are given in Section 3.4. Results of the constraint of α using EUVI are presented in Section 7.6, along with the detailed analysis of the evolution of NOAA 10956. Conclusions and future work are discussed in Section 7.7.

7.2 Observations

NOAA 10956 produced a *GOES* class B9 flare on 2007 May 19. Associated with this flare was a CME and a globally propagating disturbance within the solar corona (Long *et al.*, 2008). Extrapolations of the region's coronal magnetic field were constrained at the lower boundary with LOS magnetic field measurements obtained by the MDI on-board *SOHO*.

Images from EUVI were used to constrain the choice of α within the LFF extrapolation of the corona (Howard *et al.*, 2000). In particular, 171 Å images from EUVI were used as this passband has fewer contributions from diffuse higher temperature emission lines compared to 195 Å images (Phillips *et al.*, 2005). This results in more defined loops which are easier to compare by the methods described in Section 7.3.

7.2.1 Observation Alignment

An undefined offset in the spacecraft pointing aboard the *TRACE* telescope and the instruments small field of view can cause inaccuracies in the coordinates of *TRACE*

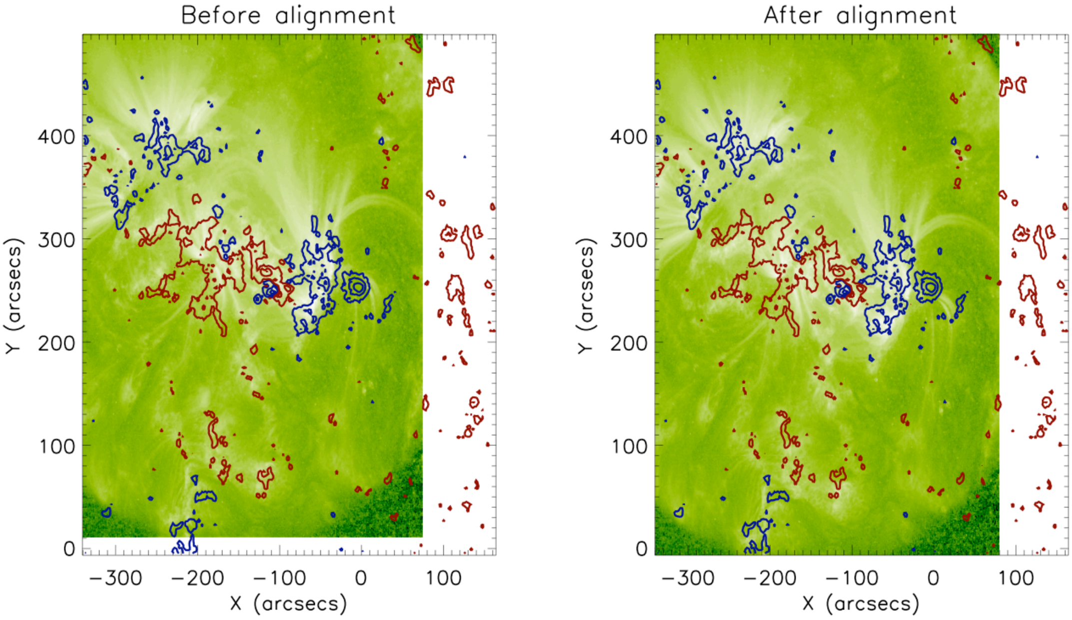

Figure 7.1: Left: Unaligned TRACE with MDI contours overlaid at -1500, -1000, -500, -100, 100, 500, 1000 and 1500 Gauss. Right: Aligned TRACE image with same contours. The TRACE image was observed at 15:59 UT on 2002 March 26, the MDI magnetogram was taken at 16:00 UT on the same day.

observations. Therefore observations from TRACE and SOHO need to be aligned in order to compare the MDI extrapolated field with TRACE observations. This is ensured by cross-correlation of the EIT and TRACE images. An example of the alignment is shown in Figure 7.1 (Gallagher, 2002).

7.2.2 Co-ordinate Transformations

The evaluation of each LFF extrapolation required the transfer of points between the *SOHO* and *STEREO* reference frames. Following the methods of Aschwanden *et al.* (2008b) a similar transformation procedure was implemented. The independent points and different resolution of the *SOHO* and *STEREO* spacecraft requires an accurate co-alignment procedure. In order to achieve this each MDI image was paired with its corresponding EUVI image, resulting in two SOHO/STEREO image pairs for the *A* and B spacecrafts. The co-alignment of each image pair required the following steps:

1. Centring the images to Sun centre.
2. Re-binning to equal pixel size (reciprocal to the distance from the Sun).
3. Rotating into a plane such that image north is the normal to the plane connecting the two spacecraft positions and Sun centre.

This is done based on the information in the FITS headers of each image.

The geometry of the transformation of points between each frame of reference is then based on the following set of equations:

$$\alpha_A = (x_A - x_{cen})(\Delta_x/3600)(\pi/180) \tag{7.1}$$

$$\delta_A = (y_B - y_{cen})(\Delta_y/3600)(\pi/180) \tag{7.2}$$

$$t^2 = \tan(\alpha_a)^2 + \tan(\delta_a)^2 \tag{7.3}$$

$$z = d_a t^2 \pm (r)^2(1+t^2) - d_a^2 t^2/(1+t^2) \tag{7.4}$$

$$x = (d_A - z)\tan(\alpha_a) \tag{7.5}$$

$$y = (d_A - z)\tan(\delta_a) \tag{7.6}$$

$$x_{B0} = d_B \sin(\alpha_{sep}) \tag{7.7}$$

$$z_b = \sqrt{d_B^2 - x_{B0}^2} \tag{7.8}$$

$$\gamma_b = \tan^{-1}(zb - z/x_{B0} \pm x) \tag{7.9}$$

$$\alpha_b = \pi/2 - \gamma_b - \alpha_s ep \tag{7.10}$$

$$\delta_b = \tan^{-1}(y/(d_B - z)) \tag{7.11}$$

$$q = (d_B/d_A) \tag{7.12}$$

$$x_B = x_{Acen} \pm q\alpha_b(3600/\Delta_x)(180/\pi) \tag{7.13}$$

$$y_B = y_{Acen} + q\delta_b(3600/\Delta_y)(180/\pi) \tag{7.14}$$

$$z_B = z \times rad_{pix} \tag{7.15}$$

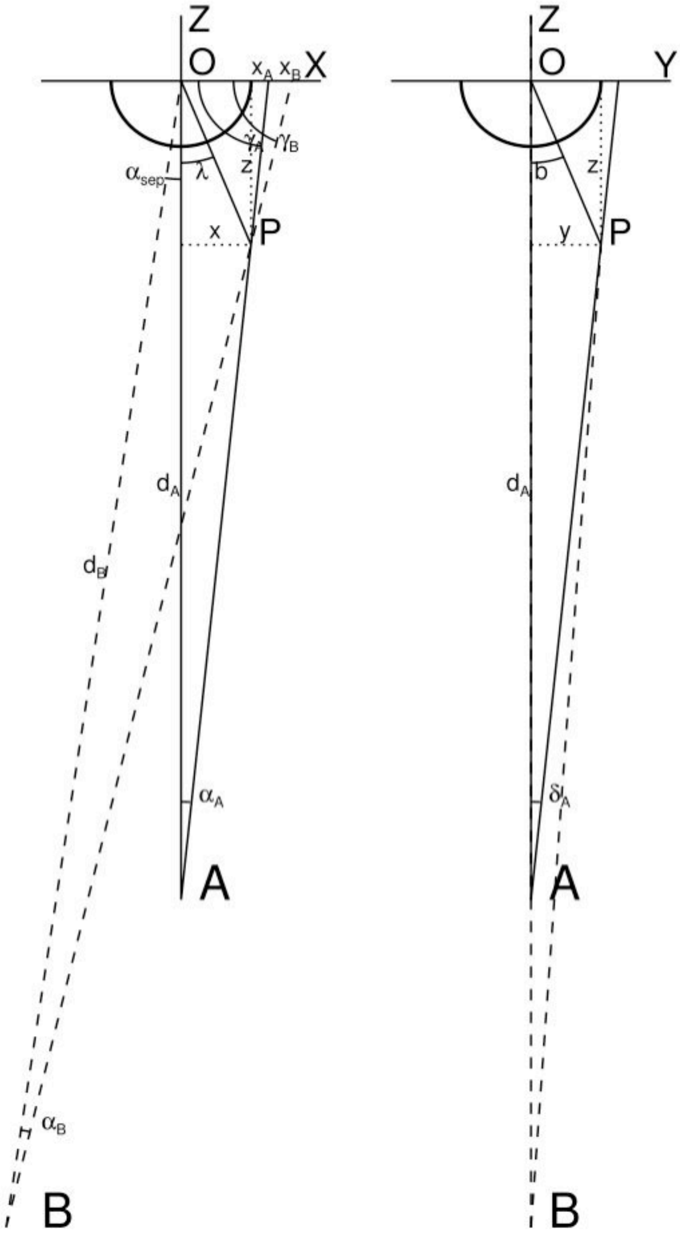

Figure 7.2: Geometry of co-aligned plane of two spacecrafts

where x_A and y_A are the x and y co-ordinate of a point in image A, r is the height given in terms of the solar radius, x_{cen} and y_{cen} are the y and y co-ordinates of the Sun centre in each image, Δ_x and Δ_y are the arc-seconds per pixel in both the x and y direction, and rad_{pix} is the radians per pixel. Other variables are as outlined in

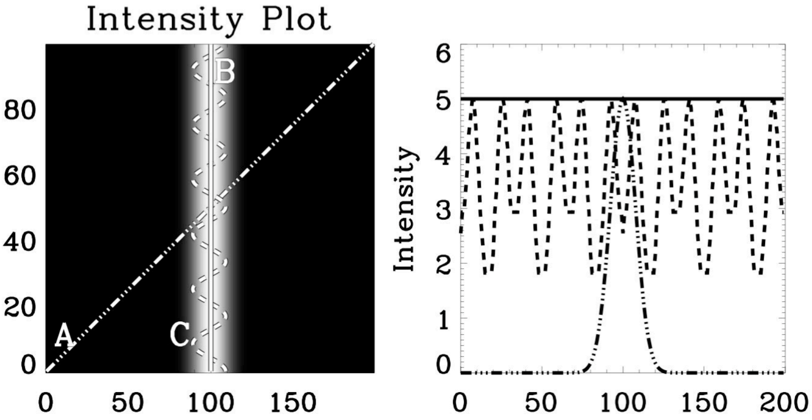

Figure 7.3: Field lines overlaid on emission with a Gaussian profile. Left panel: Bright Gaussian ridge, with three overlaid field lines A, B, and C. Field line A crosses the ridge, B rest along the ridge, and C oscillates along the ridge. Right panel: Intensity as measured along each field line.

Figure 7.2, which gives a graphical overview of the geometry. In the equation for γ_b and x_B the positive sign is for transformations in the clockwise sense and negative for anti-clockwise transformations (e.g transformation from *STEREO A* to MDI are clockwise, while those from *STEREO B* to MDI are anti-clockwise).

An additional transformation is required to convert MDI extrapolation co-ordinates (Heliographic) into the co-ordinate system of the co-aligned image pairs. This is easily done using the transformation matrix used to convert the original MDI image into the co-aligned image.

7.3 Method

For linear force-free field extrapolations α is an additional free parameter. Small changes in α result in large changes to the extrapolated field. Comparing extrapolated field-lines with EUV observations provides a method of restricting α and improving the accuracy of our results.

It is then possible to systematically determine the value of α that provides the best possible comparison with the EUV observations using the following steps:

1. Compute the linear force-free field.
2. Calculate a large number of possible magnetic field lines.
3. Project field lines onto the EUV observation.
4. Calculate the cost function along each field line.
5. Repeat for each value of α.
6. Compare the cost of the best matched field lines for each α.

In order to do this accurately it is first important to define what a *good field-line* is. Figure 7.3 shows the path and resulting intensity for three different ideal field lines. Field line A crosses the bright emission only once and has a small spike in emission along its length. Field line B rests along the field line and has a smooth bright intensity profile. Field line C oscillates on and off the bright emission and the resulting profile has a series of spikes in the intensity. With this in mind a number of methods have been developed to systematically extract loop profiles from EUV images of the solar corona (Carcedo *et al.*, 2003; Wiegelmann *et al.*, 2005). Including this information in the definition of a cost function used to constrain the choice of α removes the intermediate step of extracting coronal loop profiles. Additionally, any associated errors due to multiple loops are removed as the method looks at the emissions along each loop. For the purpose of this research, modifications to the Wiegelmann *et al.* (2005) method were studied to find the most computationally efficient and best performing cost function. A small sample of the various cost functions studied are:

$$\begin{aligned} C_W &= \int \nabla I(l) dl / l (\int I(l) dl)^2, \\ C_{EW} &= \int \nabla I(l) dl / l \int I(l) dl, \\ C_B &= 1 / \int I(l) dl, \end{aligned}$$

where $I(l)$ is the intensity of emission along a loop and l is the loop length, C_W and C_{EW} are the standard and equal weight cost functions as defined by Wiegelmann *et al.* (2005), and C_B is a modified cost function for the brightest field lines.

7.4 Testing: NOAA 9878

NOAA 9878 was close to disk centre on 26 March 2002 and began the release of a GOES C3.0 flare at 15:00 UT (Raftery *et al.*, 2009). Two MDI observations at 14:24 UT and 16:00 UT allow for the testing of the accuracy of the method and its ability to recover the observed coronal loop restructure.

Figure 7.4 shows a selection of field-lines as calculated by the C_{EW} and C_B cost function, based on TRACE and MDI observations at 14:24 UT. As can be seen both cost functions fail to completely recover the true geometry of the field. It is thought that the true value of α for the loop system in question was outside the range of α values examined here. The range could not be extended however, as errors would be introduced into the system from the complex solution to the LFF equations.

For the post flare configuration as observed at 16:00 UT, the comparison is better able to recover the geometry of the coronal field. Figure 7.5, shows a selection of field-lines as selected by the C_{EW} and C_B cost functions as been the best representative of the observed TRACE emission. As can be seen the C_B cost function performs the best. The brightness of the post-flare loops modelled is better suited to the C_B cost function compared to the C_{EW}.

As can be seen the method is able to recover the geometry of some coronal loop structures, provided an appropriate cost function is used and the level of twist in the loop is within an examinable range. As an additional check on the results, the twin perspectives of *STEREO* were used to doubly constrain the choice of α.

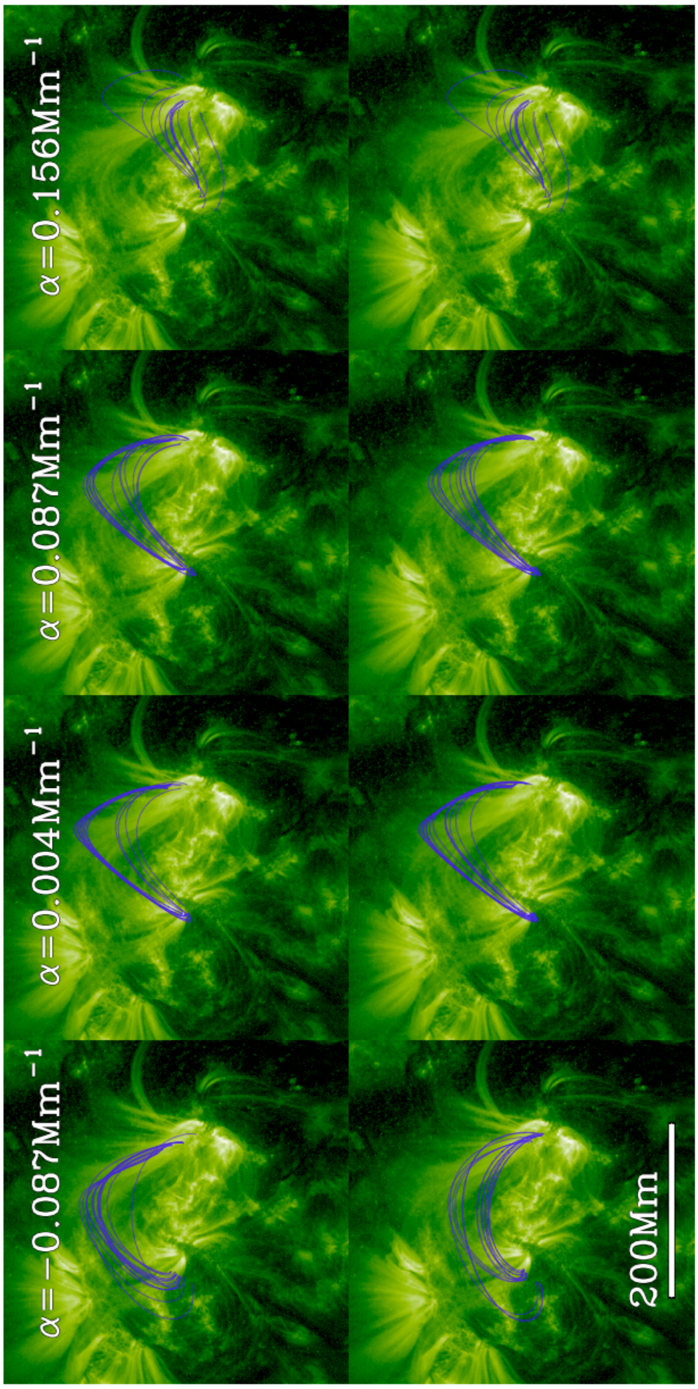

Figure 7.4: Top: TRACE 171 Å observation of NOAA 9878 at 14:24 UT on 26 March 2002. Overlaid are the best field-lines as selected by the C_{EW} cost function for a range of α values. Bottom: Same for C_B cost function.

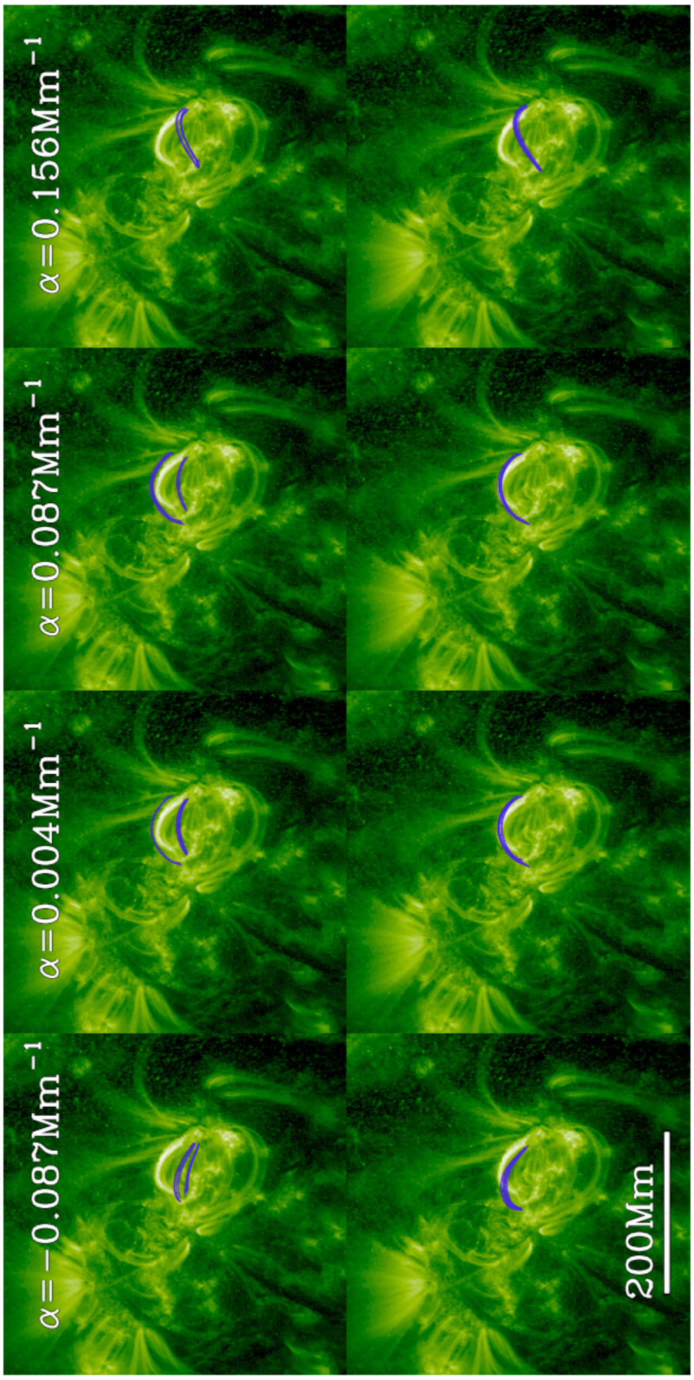

Figure 7.5: Top: *TRACE* 171 Å observation of NOAA 9878 at 16:00 UT on 26 March 2002. Overlaid are the best field-lines as selected by the C_{EW} cost function for a range of α values. Bottom: Same for C_B cost function.

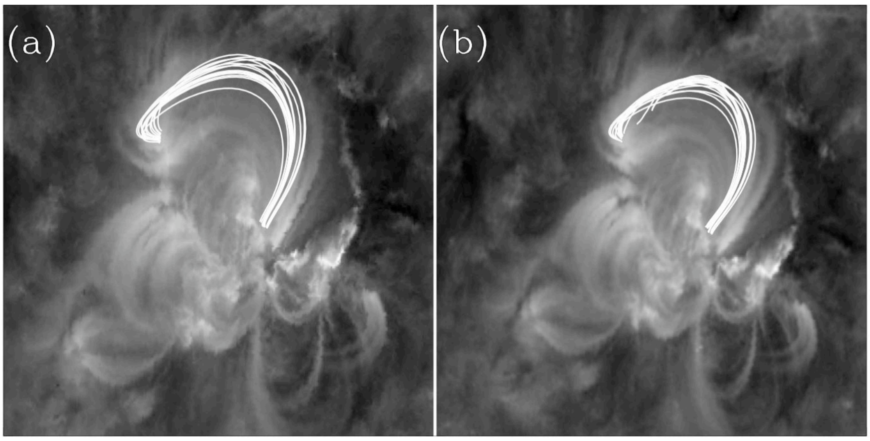

Figure 7.6: (a) 15 field-lines with the smallest cost as selected using the C_{EW} cost function with EUVI *STEREO A* images of NOAA 10956. (b) Same but for *STEREO B* images, for $\alpha = 8.7 \times 10^{-3}$ Mm^{-1}.

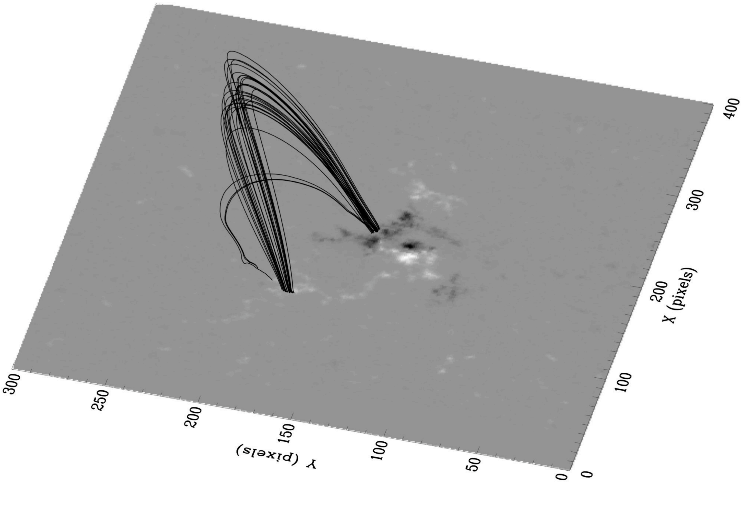

Figure 7.7: 3D view of field lines shown in Figure 7.6

7.5 *STEREO* Constrained Method

Using the LFF method from Alissandrakis (1981), field lines are extrapolated from user-defined foot-points. Field lines are then transformed to the desired perspective of each *STEREO* spacecraft, and the emission along each field line and associated cost is calculated. Small-scale loops are compact in nature and consist of multiple overlapping loops. As a result, the comparison method is restricted to large scale loops with clearly defined strands. Additionally, the infinite number of possible field line paths within the region can result in numerous invalid field lines with low costs. In order to overcome this the comparison of field lines was restricted to the 15 lines with the lowest cost for a given value of α. Field lines were restricted to start and end at user defined foot-points and the benefit of including user defined paths (e.g. circles which field lines must pass through) was also examined. Figure 7.8 shows the ability of the three cost functions to recover the geometry of the active region loop. As can be seen the inclusion of the user-defined path (Figure 7.8, bottom panels) greatly increases the accuracy of all the cost functions. The C_{EW} cost function was used in this work to select the value of α for the LFF extrapolations due to its ability to select more valid field lines.

Using the C_{EW} cost function it is possible to compare the cost function for various values of α and determine the value that most closely resembles the observed field. More than 5,000 field lines are plotted for each value of α and the cost along each is calculated. In order to enhance the sensitivity of the method to changes in the values of α only the total cost of the 15 best field lines are compared. As shown in Figure 7.8, this is a sufficient number of field lines to accurately recover the topology of the region. The contrast of the cost for each value of α was increased further by normalising the returned values and setting the cost to 1 for values of α with no field lines that match the already mentioned requirements.

Figure 7.6 shows the best field lines as selected by the method for *STEREO* EUVI images from both the A and B spacecrafts. The field lines returned by the method are not the same for each spacecraft. However, the general geometry defined by the field lines is very similar. Figure 7.7 shows the field lines from both perspectives plotted together in 3D.

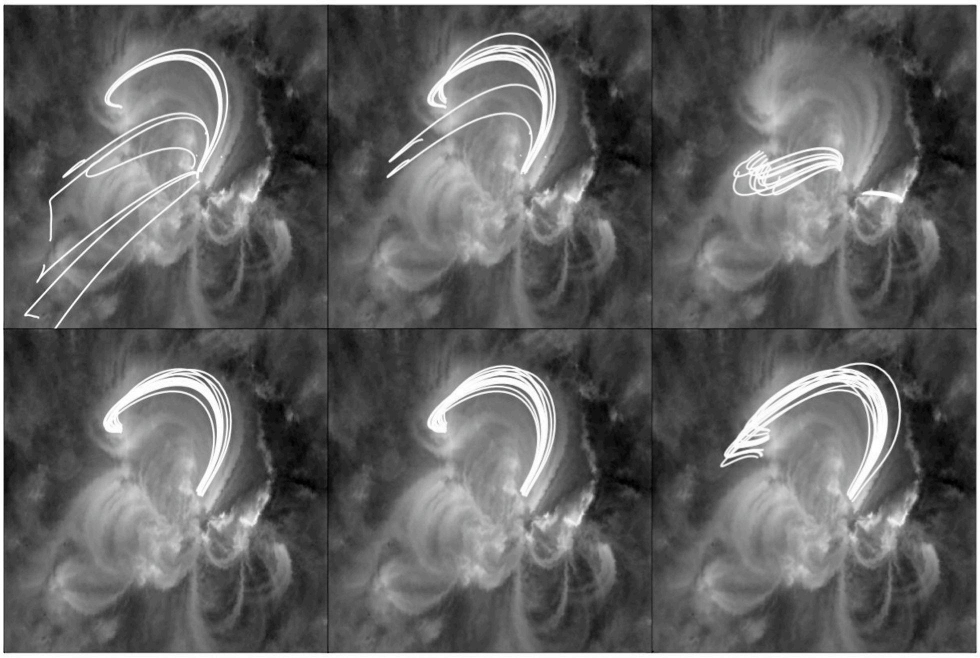

Figure 7.8: (Top): Left; Field lines with lowest cost functions using the Wiegelmann method. Centre; Field lines with lowest cost functions using the Equal Weight Wiegelmann method. Right; Field lines with lowest cost functions using the Bright method. (Bottom) Same as top with the added restrictions of field lines passing through users defined regions of interest and foot-points.

The magnetic energy within the active region was calculated as follows:

$$E_{Pot} = \int \mathbf{B}_{Pot}^2 dV, \tag{7.16}$$

$$E_{LFF} = \int \mathbf{B}_{LFF}^2 dV, \tag{7.17}$$

$$E_{free} = \int \mathbf{B}_{LFF}^2 - \mathbf{B}_{Pot}^2 dV, \tag{7.18}$$

where $\mathbf{B}_{Pot}$ and $\mathbf{B}_{LFF}$ are the potential and LFF magnetic fields, dV is a volume within the computational domain, and E_{Pot}, E_{LFF}, and E_{free} are the magnetic energy of the potential field, LFF field and the free energy, respectively.

As a precautionary warning, it should be noted that LFF extrapolations have a maximum value of α that can be studied before oscillatory signals from the complex solution of the governing set of equations begin to dominate the systems (Gary, 2001). We have investigated this effect for the data set studied here and found that for α values up to 0.03 Mm^{-1} the oscillatory signal from the complex solutions is negligible up to a height of 100 Mm, the maximum height of loops studied here.

7.6 NOAA 10956

Using the method previously described in Section 3.4, the value of α in the LFF extrapolations that provides the best match to the observed loop structures can be found. Figure 7.9 shows the evolution of the cost function for various values of α at the times studied. At all times there is a strong correlation between both the *STEREO A* and *B* cost functions. At 09:35 UT there is a distinct minimum in the cost at 5×10^{-3} Mm^{-1}. The cost for the *STEREO B* observations is seen to decrease for larger values of α, as the *STEREO A* cost does not follow this trend it is assumed false. At 11:11 UT the minimum has increased to around 1×10^{-2} Mm^{-1}, the relatively high cost returned for $\alpha = 5 \times 10^{-3}$ Mm^{-1} reinforces this increase. From 12:47 UT onwards the minimum in α or twist along the loop is seen to decrease to levels seen at 09:35 UT.

The evolution of magnetic flux within each sub-region was examined in order to more fully understand these changes in α. Each magnetogram image of NOAA 10956 was thresholded at the ±100G level to identify the main regions of magnetic flux in the global structure. Figure 7.10 shows the main positive and negative sub-regions within the active region, ranked by area from largest to smallest. From the corresponding *STEREO*/EUVI image it is clear that the large loop structure studied above is associated with field lines connecting 1^- and 3^+. Table 7.1 summarises the changing magnetic properties of the region (some negative regions are excluded due to changes in ranking during the time studied).

There was a significant emergence of flux into the region during the time analysed.

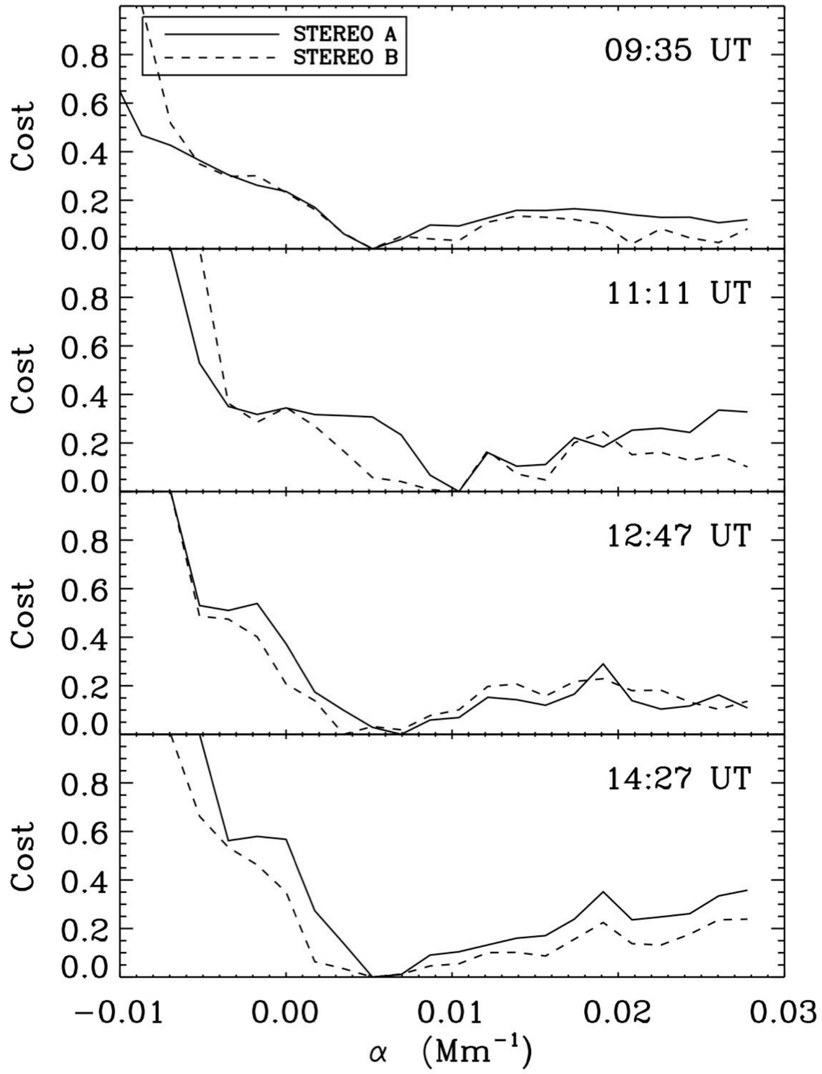

Figure 7.9: Top to bottom panels: cost function as calculated for a range of α values and MDI magnetogram at 09:35 UT, 11:11 UT, 12:47 UT, and 14:27 UT. Solid and dashed lines represent comparisons with *STEREO A* and *B* EUVI observations respectively.

While there was little or no change in the mean and maximum flux contained in each sub-region, there were significant changes in the total flux contained in each sub-region. From 09:35 UT to 11:11 UT, the total flux in regions, 1^+, 1^-, and 2^+ decreased by 3, 6, and 5 kG respectively. During this time the other regions saw little or no change in the total flux. From 11:11 UT to 12:47 UT, there was a 3 kG increase in the total

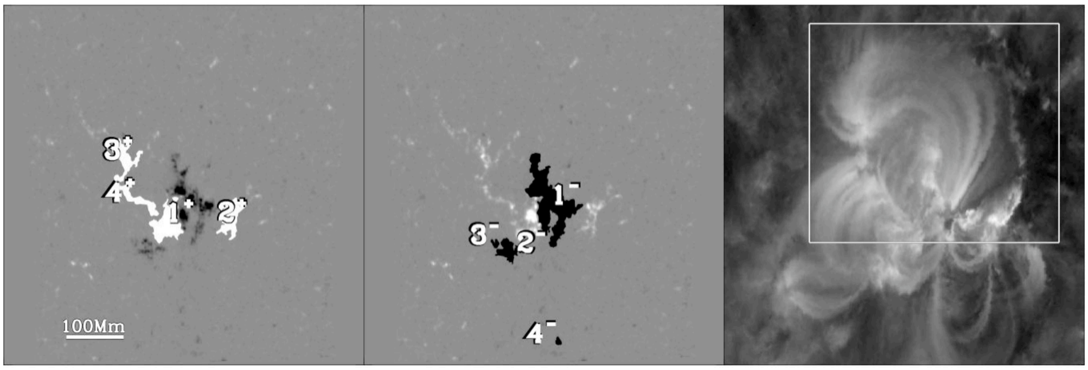

Figure 7.10: Sub-regions of active region. Left panel: Positive regions identified by thresholding, ranked in order of area. Centre panel: Same for negative regions. Right panel: Corresponding *STEREO*/EUVI Image. The smaller volume centred on the observed loop used for the energy calculations is illustrated by the box shown.

magnetic flux in region 1^+. This was accompanied by a 1 kG increase in region 2^+ and 1.4 kG decrease in region 3^+. From 12:47 UT to 14:27 UT, there was total magnetic flux increase of 3 kG. 1 kG, 8.7 kG and 2.3 kG in region 1^+, 2^+, 3^+ and 1^- respectively. There was an additional decrease in the total flux contained in region 4^+ of 4.5 kG.

Knowing the values of α, it is now possible to study changes in the connectivity within the region. As region 1^- is the common foot-point for most of the loops in the active region it was selected as the source for all the extrapolated field-lines used to examine the changing connectivity, as presented in Table 7.2. From 09:35 UT to 11:11 UT the major changes in connectivity are associated with the transfer of flux from a closed to open configuration and a 2% increase in flux connecting region 1^- to 4^+. From 11:11 UT to 12:47 UT, there is a decrease in the amount of open flux and an increase in the connectivity from region 1^- to regions 1^+, 2^+, and 3^+ by 4.8%, 0.8%, and 2.3% respectively. Additionally, the amount of flux joining region 1^- to region 4^+ decreases by 3%. From 12:47 UT to 14:27 UT the amount of open flux continues to decrease and there is no flux left connecting region 1^- to region 4^+. The amount of flux connecting to region 1^+ increases by an additional 9%. There are marginal changes in the flux connecting region 1^- to regions 2^+ and 3^+.

Table 7.1: Evolution of magnetic properties of major sub-regions contained within NOAA 10956. Results are reported in kG.

Region	Property	09:35 UT	11:11 UT	12:47 UT	14:27 UT
1^+	Mean	0.426	0.410	0.410	0.407
	Total	167.9	164.9	168.2	171.9
	Max	1.78	1.79	1.804	1.860
1^-	Mean	0.394	0.384	0.372	0.371
	Total	387.9	381.8	381.5	383.8
	Max	1.80	1.866	1.904	1.904
2^+	Mean	0.212	0.223	0.228	0.232
	Total	62.1	57.1	58.4	59.7
	Max	0.749	0.782	0.857	0.696
3^+	Mean	0.209	0.206	0.222	0.211
	Total	35.8	35.5	34.1	42.8
	Max	0.749	0.858	0.806	0.816
4^+	Mean	0.202	0.190	0.175	0.209
	Total	16.23	16.8	15.3	10.8
	Max	0.629	0.710	0.694	0.794

Table 7.2: Connectivity matrix for field lines starting at negative region 1, with threshold of ±50 G. All results are a percentage of total flux leaving negative region 1.

1^-	09:35 UT	11:11 UT	12:47 UT	14:27 UT
Open	13.9	20.6	15.9	12.9
Closed	31.9	24.3	23.8	23.6
1^+	24.5	25.1	29.8	38.9
2^+	11.1	10.8	11.6	11.2
3^+	9.8	9.7	12.0	12.3
4^+	7.4	9.3	6.2	0.00

Table 7.3: Changes in the magnetic energy contained within different volumes in NOAA 10956. The small region is a box centred on the the loop structure connecting 1^- and 3^+. The full volume in the whole computation domain. All values for energy are reports in units of 10^{32} ergs.

Size	Parameter	09:35	11:11 UT	12:47 UT	14:27 UT
Small Region	Pot	4.46	4.44	4.44	4.48
	LFF	4.48	4.50	4.46	4.49
	Free	0.013	0.061	0.021	0.01
Full Volume	Pot	6.51	6.38	6.33	6.23
	LFF	6.53	6.49	6.37	6.24
	Free	0.021	0.109	0.037	0.018

Knowing the increase of magnetic flux in the region and the significant changes in connectivity, it was decided to investigate the amount of free energy available in the region over time. Table 7.3 shows the energy calculations for two volumes: one centred on the loop structure connecting 1^- and 3^+ (see region outlined in Figure 7.10), the other being the full computational volume. From this it is clear that there is a significant buildup in free energy within both volumes from 09:35 UT to 11:11 UT. At 12:47 UT, the amount of free energy has significantly decreased and is only marginally higher than that at 09:35 UT, while at 14:27 UT the free energy is lower than at 09:35 UT.

7.7 Conclusions

NOAA 10956 rotated onto the solar disk on 15 May 2007 and on 19 May 2007 the region produced a B9 class flare, starting at 12:34 UT, peaking at 13:02 UT and ending at 13:19 UT. The flare location suggests that the source of the flare was the loop structure connecting region 1^- to 2^+ in our analysis. According to the *SOHO* LASCO CME Catalogue, the region had an associated CME which first appeared at 13:24 UT in the C2 field of view. In addition, a disappearing solar filament was observed erupting from the lower right section of the regions beginning at 12:31 UT (Long *et al.*, 2008).

Our analysis has highlighted a number of physical changes within the magnetic structure of the active region around this time. These are:

- Emerging magnetic flux elements.
- An increase in the amount of α or twist along the observed loop.
- Significant changes in the free energy of the region.
- Changes in the connectivity between sub-regions.

The increase in the amount of twist or α along the observer loop from 09:35 UT to 11:11 UT, was accompanied by a decrease in the total magnetic flux within sub-region 1^+, 1^-, and 2^+ and an increase in the amount of free energy within the volume. The increase in free energy can be explained by the increase in α used to calculate it. However, as α is obtained from a comparison to EUV observations this increase is taken as real. Following the increase in α at 11:11 UT, the amount of twist along the observed loop decreases to 09:35 UT levels by 14:27 UT. During this time period the total magnetic flux in sub regions 1^+, 1^-, 2^+, and 3^+ increases by 2-7 kG and there is a 6 kG decrease in flux in 4^+. Additionally, the free energy decreases to 09:35 UT levels over the same time period. Changes in the connectivity from region 1^- can be associated with the changes in α prior to 11:11 UT. However, by 12:47 UT the amount of flux connecting to regions 1^+ and 3^+ rose significantly.

From 09:35 UT to 11:11 UT the free energy increased from 1.3×10^{30} to 6.1×10^{30} ergs in the small volume centred on the observed loop and from 2.1×10^{30} to 10.9×10^{30} ergs in the full computational domain. By 12:47 UT the free energy in the system had dropped by a factor of 3 and by 14:27 UT had decreased below the energy at 09:35 UT. The build-up and subsequent decrease in free energy in the system is correlated with the mechanisms thought to be responsible for the release of the B9 flare at 12:30 UT. The calculated energies and free energies of the region are several orders of magnitude lower than previously reported values (Gary, 1989; Metcalf *et al.*, 1995, 2005; Régnier, 2007).

This is thought to be a combination of the smaller active region size, lower magnitude flare produced and the smaller volumes analysed.

The above investigation of magnetic properties of NOAA 10956 has shown that from 09:35 UT there was a significant amount of flux cancellations within the region, accompanied by an increase in the amount of twist and free energy along the observed loop. Following the onset of the flare at 12:34 UT, the amount of twist and free energy in the loops decreased. This was accompanied by the decrease in open flux leaving region 1^- and an increase in the magnetic flux in the region. It is suggested that the sudden decrease and subsequent increase in magnetic flux within the active region and the changes in twist and free energy caused small changes in the observed connectivity between sub-regions, Table 7.2. The emergence of magnetic flux within the region and resulting increase in magnetic free energy could have resulted in the region passing a critical threshold, passed which it was in an unstable configuration. Under the theory of self-organised criticality this would have resulted in a series of events returning the region to a stable configuration (Vlahos & Georgoulis, 2004). Whether the mechanism responsible for passing this critical threshold is the unbalanced emergence of flux within the region or the resulting non-potentiality of the flux ropes remains unknown. The decrease in both α and free energy and increase in connectivity of the loop connecting region 1^- to 3^+ suggests that the loop had room to expand and relax into the neighbouring sub-region following the flare and eruption in the neighbouring sub-region.

It has been shown that the method is able to detect changes in the amount of twist (and hence current) within coronal loop structures. The additional analysis of a sub-region's magnetic properties provided great insight into the evolution and driving forces within the active region. Future work is needed to improve the method and remove the need for user input. Expanding the method for the analysis of multiple loop structures in active regions would greatly increase the diagnostic power of the algorithm.

8

Conclusions and Future Work

This thesis has sought to increase the understanding of the mechanism thought to be responsible for solar flares and CMEs. A summary and interpretation of these findings are presented here along with possible directions for future work.

8.1 Principal Results

The primary objective of this study was to further the understanding of active region evolution and detect possible precursors for solar flaring. Two independent methods were used to achieve this. The mathematical analysis of active region magnetic fields, as observed at the photospheric level, were interpreted using fractal and multifractal techniques. Additionally, the coronal magnetic field was analysed using an extrapolation technique. The main results arising from these studies can be summarised as follows:

1. The adaptation of the MFRAC box-counting multifractal package for the analysis of MDI solar magnetogram images.
2. The box-counting multifractal package was shown to detect sudden changes in the structure of active region magnetic fields. As such, the method is responsive

to the emergence of flux elements and changes in the internal configuration of the magnetic field.

3. The multifractal spectrum, as returned by the box-counting method, was shown to decrease in width and breadth for a sample of flaring active region. The increase in both $f(\alpha)$ and α for the higher values of q, or higher moment magnetic flux elements, suggests that as an active region reconfigures to a flaring favourable state the high moment flux elements occupy a greater proportion of the active region.

4. A wavelet based modulus maximum method was successfully adapted for the analysis of *SOHO* MDI magnetogram data. The WTMM method offers increased stability and accuracy over the box-counting method.

5. Using the WTMM method the fractal and multifractal properties of the solar magnetic field were studied. The fractal properties of the quiet and active Sun magnetic fields were found to be distinct from each other in wavelet modulus space. As such, a segmentation procedure was developed to remove the active region magnetic field from the surrounding quiet Sun structures. As shown with the theoretical data set the segmentation procedure allows for the accurate recovery of the active region fractal and multifractal properties.

6. The quiet Sun magnetic field, as measured by *SOHO* MDI, was found to be multifractal in nature. The quiet Sun spectrum peaked at a fractal dimension of 2 and hölder exponent of -0.75. Further analysis of the quiet Sun multifractal spectrum revealed the super-granular magnetic features as the source of the quiet Sun's multifractality.

7. As with the box-counting method the WTMM method was suitable for detecting changes in the structure of the active Sun's magnetic fields. The segmentation

procedure allows for the detection of flux emergence with a quicker rise time than the traditional indicators of area and magnetic field strength.

8. From the sample of active regions studied a fractal dimension greater than 1.2 was a shown to be a possible threshold for detecting active regions in a flaring favourable state.
9. Similarly, from the analysis of active regions using the WTMM methods a Hölder exponent greater than -0.75 may be an indicator of active region in flaring favourable states.
10. The development of an LFF extrapolation technique to recover the 3D topology of coronal loops, as constrained by *STEREO* EUVI images of the corona.
11. Using the *STEREO* constrained LFF method changes in the amount of twist or α along the observed loops can be studied.
12. Topological and photospheric analysis tools were developed and used to analyse the changing properties of NOAA 10956 during its evolution.
13. Changes in the magnetic flux within NOAA 10956 were shown to occur simultaneously with changes in the amount of twist, free energy and connectivity along the observed loop and within the active region.

8.2 Outstanding Problems

While the methods used in this study have been shown to enhance our understanding of active region evolution, they are not without their limits. The following points highlight the main areas of concern with each of the methods:

1. Box-counting algorithms are designed for discrete data sets and defined for continuous domains. As solar magnetogram data is continuous in nature and finite in

size, numerical errors are enhanced during calculations. This leads to significant errors in the spectrum for negative values of q.

2. Both the WTMM and box-counting methods involve regression over a range of measurements and scales. The range of scales in each active region is not constant. As such, the range of scales for the regression is different for each calculation. While the best effort is made to select a suitable range of scales for all regions, for large studies, errors cannot be avoided with existing regression techniques.

3. The threshold level used in both the segmentation procedure, box-counting method and analysis for the photospheric magnetogram is fixed for all the images analysed. The strength of the quiet Sun magnetic field varies during the solar cycle and having a fixed threshold for the analysis of magnetic properties introduces some errors although they are not thought to be significant. The effect of this variation on the threshold used in the segmentation procedure is unknown. The nature of the solar 11 year cycle inhibits the analysis of both full disk quiet and active Sun magnetograms. As such, the errors associated with a fixed threshold in the segmentation procedure may remain unknown.

4. The LFF extrapolation method developed here is limited to the analysis of one observed coronal loop structure. Furthermore, it is restricted through the use of user-defined guiding paths. This restricts the method ability to automatically select the best comparison if that differs from the initial guess.

5. The field lines selected by the LFF extrapolation method are dependant on the cost function used in their calculation. Different cost function may perform better for coronal loops during different phases of their evolution (e.g. pre-flare vs post-flare).

8.3 Future Work

During the development and analysis of these methods, limitations on the code and scope of these projects were inevitable. Further work is required before a complete understanding of active region evolution can be achieved. The following points outline some areas of improvement and further study:

1. As fractal and multifractal methods are based on the self-similar nature of active regions, all analysis would benefit from increased resolution of images. Alternatively, increased cadence would allow for averaging over a greater number of images, therefore increasing the statistics of the calculations.

2. Fractal and multifractal methods have been shown to detect changes in the internal structure of active regions and shown to be correlated with extended periods of flaring. However, a large statistical study is required to confirm any threshold found. A large statistical study would provide forecasters with a range of thresholds depending on their individual requirements.

3. As already mentioned, the range of scales over which regression is performed is at present fixed in the methods discussed here. An automated regression method, if implemented, would further increase the accuracy of the results presented here.

4. The box-counting method showed a relationship between changes in the width and breadth of the multifractal spectrum with flaring over time. While the WTMM method is able to calculate the multifractal spectrum of active regions only results for the peak of this spectrum were investigated here. Therefore the shape of the $D(h)$ versus h spectrum may provide an additional insight into the changing structure of active regions. The range of scales over which the regression is valid is susceptible to changes in the value of q. This may restrict the analysis of the full $D(h)$ versus h spectrum until increased resolution images are available or the

cadence of magnetogram observations is increased.

5. All the methods studied as part of this thesis require photospheric measurements of the solar magnetic field. As chromospheric measurements of the solar magnetic field become available, the methods used in this thesis could be used to analyse their properties. A comparison of the photospheric and chromospheric measurements may give an insight into the structure of the solar atmosphere.

6. In the course of this study we made use of LFF extrapolation techniques. While we presented a novel method of constraining α with *STEREO* EUVI observations, our extracted topology remains an approximation to the real field. Only through the use of more advanced methods such as NLFF extrapolations or MHD modelling can the true nature of the coronal magnetic field be known. However, such a method requires more detailed knowledge of the boundary conditions on all sides of the computational domain.

7. It has been shown that the methods developed here provide an insight into the evolution of active regions and may prove useful in the prediction of solar flares. From a practical point of view, it can be envisioned that these parameters alone would not be sufficient in predicting solar flares. It is essential that other factors such as area, total magnetic field strength, and number of spots should be utilised with these methods in order to ensure accurate predictions. Personally, I believe that with a combination of physical parameters, the fractal and multifractal parameters discussed here would be of assistance when predicting active regions in flaring favourable states.

8. The ultimate goal of this thesis was to provide some mechanism upon which real-time space weather predictions could be made. Due to time constraints, this is unfeasible. With the completion of a large statistical study, the power of these methods should be known and their incorporation into a space weather suite

such as `SolarMonitor.org` or the Heliophysics Integrated Observatory (`www.helio-vo.eu`) could be possible.

References

ABBETT, W.P. & FISHER, G.H. (2003). A Coupled Model for the Emergence of Active Region Magnetic Flux into the Solar Corona. *Astrophys. J.*, **582**, 475–485. xiii, 14, 15

ABRAMENKO, V., YURCHYSHYN, V. & WANG, H. (2008). Intermittency in the Photosphere and Corona above an Active Region. *Astrophys. J.*, **681**, 1669–1676. 86

ABRAMENKO, V.I. (2005a). Multifractal Analysis Of Solar Magnetograms. *Solar Phys.*, **228**, 29–42. xvi, 61, 62, 71, 86, 87, 106

ABRAMENKO, V.I. (2005b). Relationship between Magnetic Power Spectrum and Flare Productivity in Solar Active Regions. *Astrophys. J.*, **629**, 1141–1149. 16, 58, 59, 62, 71, 81, 106

ABRAMENKO, V.I., YURCHYSHYN, V.B., WANG, H., SPIROCK, T.J. & GOODE, P.R. (2002). Scaling Behavior of Structure Functions of the Longitudinal Magnetic Field in Active Regions on the Sun. *Astrophys. J.*, **577**, 487–495. 71

ABRY, P., JAFFARD, S. & LASHERMES, B. (2004). Revisiting scaling, multifractal and multiplicative cascades with the wavelet leader lens. In *Proc. of SPIE on Wavelet Applications in Industrial Processing II*, vol. 5607, Philadelphia, USA. 69

ALBER, J., M. ANDPEINKE (1997). Improved multifractal box-counting algorithm, virtual phase transitions, and negative dimensions. *Physical Review E*, **57**, 5489–5493. 72, 73

ALISSANDRAKIS, C.E. (1981). On the computation of constant alpha force-free magnetic field. *Astron. Astrophys.*, **100**, 197–200. 47, 48, 118

ARNEODO, A., ARGOUL, F., BACRY, E., ELEZGARAY, J. & MUZY, J.F. (1995a). *Ondelettes, Multifractales et Turbulences : de l'ADN aux croissances cristallines*. Diderot Editeur, Art et Sciences, Paris. 86

ARNEODO, A., BACRY, E. & MUZY, J.F. (1995b). The thermodynamics of fractal revisited with wavelets. *Physica A Statistical Mechanics and its Applications*, **213**, 232–275. 63, 67

ARNEODO, A., DECOSTER, N. & ROUX, S.G. (1999). Intermittency, Log-Normal Statistics, and Multifractal Cascade Process in High-Resolution Satellite Images of Cloud Structure. *Physical Review Letters*, **83**, 1255–1258. 67

ARNÉODO, A., DECOSTER, N. & ROUX, S.G. (2000). A wavelet-based method for multifractal image analysis. I. Methodology and test applications on isotropic and anisotropic random rough surfaces. *European Physical Journal B*, **15**, 567–600. 67

ASCHWANDEN, M.J. (2005). *Physics of the Solar Corona. An Introduction with Problems and Solutions (2nd edition)*. xiii, 15, 18, 19, 43

ASCHWANDEN, M.J., NITTA, N.V., WUELSER, J. & LEMEN, J.R. (2008a). First 3D Reconstructions of Coronal Loops with the STEREO A+B Spacecraft. II. Electron Density and Temperature Measurements. *Astrophys. J.*, **680**, 1477–1495. 29

Aschwanden, M.J., Wülser, J.P., Nitta, N.V. & Lemen, J.R. (2008b). First Three-Dimensional Reconstructions of Coronal Loops with the STEREO A and B Spacecraft. I. Geometry. *Astrophys. J.*, **679**, 827–842. 17, 29, 110

Aschwanden, M.J., Wuelser, J.P., Nitta, N.V., Lemen, J.R. & Sandman, A. (2009). First Three-Dimensional Reconstructions of Coronal Loops with the STEREO A+B Spacecraft. III. Instant Stereoscopic Tomography of Active Regions. *Astrophys. J.*, **695**, 12–29. 17, 29

Babcock, H.W. (1953). The Solar Magnetograph. *Astrophysical Journal*, **118**, 387. xiv, 5, 6, 25, 26

Badii, R. & Politi, A. (1985). Statistical description of chaotic attractors: the dimension function. *J. Stat. Phys.*, **40**, 725. 66

Berger, T.E. & Lites, B.W. (2003). Weak-Field Magnetogram Calibration using Advanced Stokes Polarimeter Flux Density Maps - II. SOHO/MDI Full-Disk Mode Calibration. *Solar Phys.*, **213**, 213–229. 72, 88

Biskamp, D. (1986). Magnetic Reconnection Via Current Sheets (Invited paper). In M.A. Dubois, D. Grésellon & M.N. Bussac, eds., *Magnetic Reconnection and Turbulence*, 19–+. 19

Bugayevskiy, L.M. & Snyder, J.P. (1995). *Map projections : a reference manual*. 72

Bunde, A., Kropp, J. & Schellnhuber, H.J., eds. (2002). *The Science of Disasters : climate disruptions, heart attacks and market crashes*. Springer Verlag, Berlin. 86

Burnette, A.B., Canfield, R.C. & Pevtsov, A.A. (2004). Photospheric and Coronal Currents in Solar Active Regions. *Astrophys. J.*, **606**, 565–570. 50

Cadavid, A.C., Lawrence, J.K., Ruzmaikin, A.A. & Kayleng-Knight, A. (1994). Multifractal models of small-scale solar magnetic fields. *Astrophys. J.*, **429**, 391–399. 59, 64, 72, 74

Caddle, L.B., Grant, J.L., Szatkiewicz, J., van Hase, J., Shirley, B.J., Bewersdorf, J., Cremer, C., Arneodo, A., Khalil, A. & Mills, K.D. (2007). Chromosome neighborhood composition determines translocation outcomes after exposure to high-dose radiation in primary cells. *Chromosome Res*, **15**, 1061–73. 88

Carcedo, L., Brown, D.S., Hood, A.W., Neukirch, T. & Wiegelmann, T. (2003). A Quantitative Method to Optimise Magnetic Field Line Fitting of Observed Coronal Loops. *Solar Phys.*, **218**, 29–40. 114

Chappell, D. & Scalo, J. (2001). Multifractal Scaling, Geometrical Diversity, and Hierarchical Structure in the Cool Interstellar Medium. *Astrophys. J.*, **551**, 712–729. 64, 73

Conlon, P.A. & Gallagher, P.T. (2009). Constraining Magnetic Field Extrapolations of a Solar Active Region Using *STEREO*. *Astrophys. J.*, submitted. 108

Conlon, P.A., Gallagher, P.T., McAteer, R.T.J., Ireland, J., Young, C.A., Kestener, P., Hewett, R.J. & Maguire, K. (2008). Multifractal Properties of Evolving Active Regions. *Solar Physics*, **248**, 297–309. xvii, 67, 70, 75, 86, 87, 88, 107

Conlon, P.A., Kestener, P., McAteer, R., Gallagher, P., Fennell, L. & Khalil, A., A.and Arenedo (2009). Characterising Complexity in Compounded Sytems II: Magnetic Fields, Flares & Frecasts. *Astrophys. J.*, submitted. 58, 85

Daubechies, I. (1992). *Ten Lecture on Wavelets*. Capital City Press, Vermont. 59

Davidson, P.A. (2004). *Turbulence : an introduction for scientists and engineers*. xiv, 37

Decoster, N., Roux, S.G. & Arnéodo, A. (2000). A wavelet-based method for multifractal image analysis. II. Applications to synthetic multifractal rough surfaces. *European Physical Journal B*, **15**, 739–764. 86

Delaboudinière, J.P., Artzner, G.E., Brunaud, J., Gabriel, A.H., Hochedez, J.F., Millier, F., Song, X.Y., Au, B., Dere, K.P., Howard, R.A., Kreplin, R., Michels, D.J., Moses, J.D., Defise, J.M., Jamar, C., Rochus, P., Chauvineau, J.P., Marioge, J.P., Catura, R.C., Lemen, J.R., Shing, L., Stern, R.A., Gurman, J.B., Neupert, W.M., Maucherat, A., Clette, F., Cugnon, P. & van Dessel, E.L. (1995). EIT: Extreme-Ultraviolet Imaging Telescope for the SOHO Mission. *Solar Phys.*, **162**, 291–312. xiv, 27

DeRosa, M.L., Schrijver, C.J., Barnes, G., Leka, K.D., Lites, B.W., Aschwanden, M.J., Amari, T., Canou, A., McTiernan, J.M., Régnier, S., Thalmann, J.K., Valori, G., Wheatland, M.S., Wiegelmann, T., Cheung, M.C.M., Conlon, P.A., Fuhrmann, M., Inhester, B. & Tadesse, T. (2009). A Critical Assessment of Nonlinear Force-Free Field Modeling of the Solar Corona for Active Region 10953. *Astrophys. J.*, **696**, 1780–1791. xv, 46, 52

Domingo, V., Fleck, B. & Poland, A.I. (1995). The SOHO Mission: an Overview. *Solar Physics*, **162**, 1–2. 22

Frisch, U. (1995). *Turbulence*. Cambridge Univ. Press, Cambridge. 57

Gallagher, P. (2002). Trace/eit 19.5 nm image alignment using cross-correlation, `http://www.tcd.ie/Physics/People/Peter.Gallagher/trace-align/index.html`. 110

GALLAGHER, P.T. (1999). *Optical and EUV Observations of the Solar Atmosphere*. Ph.D. thesis, Queen's University, Belfast, Northern Ireland. xiii, 7

GALLAGHER, P.T. (2000). *Optical and EUV Observations of the Solar Atmosphere*. Ph.D. thesis, AA(The Queen's University of Belfast and the Rutherford Appleton Laboratory). xiv, 9, 24, 25

GALLAGHER, P.T., MOON, Y.J. & WANG, H. (2002). Active-Region Monitoring and Flare Forecasting I. Data Processing and First Results. *Solar Phys.*, **209**, 171–183. 18

GALLAGHER, P.T., MCATEER, R.T.J., YOUNG, C.A., IRELAND, J., HEWETT, R.J. & CONLON, P. (2007). Solar Activity Monitoring. In J. Lilensten, ed., *Space Weather : Research Towards Applications in Europe 2nd European Space Weather Week (ESWW2)*, vol. 344 of *Astrophysics and Space Science Library*, 15. 108

GARY, G.A. (1989). Linear force-free magnetic fields for solar extrapolation and interpretation. *Astrophys. J. Suppl. Series*, **69**, 323–348. 47, 126

GARY, G.A. (2001). Plasma Beta above a Solar Active Region: Rethinking the Paradigm. *Solar Phys.*, **203**, 71–86. 9, 43, 109, 121

GEORGOULIS, M.K. (2005). Turbulence In The Solar Atmosphere: Manifestations And Diagnostics Via Solar Image Processing. *Solar Phys.*, **228**, 5–27. xvi, 60, 61, 62, 71, 87

GEORGOULIS, M.K. (2008). Magnetic complexity in eruptive solar active regions and associated eruption parameters. *Geophys. Res. Lett.*, **35**, 6–+. 16, 87

GOOSSENS, M. (2004). Book Review: An Introduction To Plasma Astrophysics and Magnetohydrodynamics / Kluwer Academic, 2003. *The Observatory*, **124**, 303–+. 36

Gordon Holman, S.B. (1990). What is a solar flare? `http://hesperia.gsfc.nasa.gov/sftheory/flare.htm`. 17

Green, L.M., Démoulin, P., Mandrini, C.H. & Van Driel-Gesztelyi, L. (2003). How are Emerging Flux, Flares and CMEs Related to Magnetic Polarity Imbalance in MDI Data? *Solar Phys.*, **215**, 307–325. 72

Hale, G.E., Ellerman, F., Nicholson, S.B. & Joy, A.H. (1919). The magnetic polarity of sun-spots. *The Astrophysical Journal*, **49**, 153. 10

Halsey, T.C., Jensen, M.H., Kadanoff, L.P., Procaccia, I. & Shraiman, B.I. (1986). Fractal measures and their singularities - The characterization of strange sets. *Phys. Rev. A*, **33**, 1141–1151. 43, 66

Handy, B.N., Acton, L.W., Kankelborg, C.C., Wolfson, C.J., Akin, D.J., Bruner, M.E., Caravalho, R., Catura, R.C., Chevalier, R., Duncan, D.W., Edwards, C.G., Feinstein, C.N., Freeland, S.L., Friedlaender, F.M., Hoffmann, C.H., Hurlburt, N.E., Jurcevich, B.K., Katz, N.L., Kelly, G.A., Lemen, J.R., Levay, M., Lindgren, R.W., Mathur, D.P., Meyer, S.B., Morrison, S.J., Morrison, M.D., Nightingale, R.W., Pope, T.P., Rehse, R.A., Schrijver, C.J., Shine, R.A., Shing, L., Strong, K.T., Tarbell, T.D., Title, A.M., Torgerson, D.D., Golub, L., Bookbinder, J.A., Caldwell, D., Cheimets, P.N., Davis, W.N., Deluca, E.E., McMullen, R.A., Warren, H.P., Amato, D., Fisher, R., Maldonado, H. & Parkinson, C. (1999). The transition region and coronal explorer. *Solar Physics-dsa*, **187**, 229–260. xiv, 30, 31

Hewett, R.J., Gallagher, P.T., McAteer, R.T.J., Young, C.A., Ireland, J., Conlon, P.A. & Maguire, K. (2008). Multiscale Analysis of Active Region Evolution. *Solar Phys.*, **248**, 311–322. 40, 59, 82, 106

Howard, R.A., Moses, J.D. & Socker, D.G. (2000). Sun-Earth connection coronal and heliospheric investigation (SECCHI). In S. Fineschi, C. M. Korendyke, O. H. Siegmund, & B. E. Woodgate , ed., *Society of Photo-Optical Instrumentation Engineers (SPIE) Conference Series*, vol. 4139 of *Presented at the Society of Photo-Optical Instrumentation Engineers (SPIE) Conference*, 259–283. 109

Ireland, J., Young, C.A., McAteer, R.T.J., Whelan, C., Hewett, R.J. & Gallagher, P.T. (2008). Multiresolution Analysis of Active Region Magnetic Structure and its Correlation with the Mount Wilson Classification and Flaring Activity. *Solar Phys.*, **252**, 121–137. 92

Jansen, F., Pirjola, R. & Favre, R. (2000). Space weather: Hazard to the Earth? 20

Kestener, P. & Arneodo, A. (2003). A three-dimensional wavelet based multifractal method : about the need of revisiting the multifractal description of turbulence dissipation data. *Phys. Rev. Lett.*, **91**, 194501. 67

Kestener, P. & Arneodo, A. (2004). Generalizing the wavelet-based multifractal formalism to random vector fields: Application to three-dimensional turbulence velocity and vorticity data. *Physical Review Letters*, **93**, 44501, (c) 2004: The American Physical Society. 86

Kestener, P. & Arneodo, A. (2004). Generalizing the wavelet-based multifractal formalism to vector-valued random fields: application to turbulent velocity and vorticity 3d numerical data. *Phys. Rev. Lett.*, to appear. 67

Kestener, P. & Arneodo, A. (2007). A multifractal formalism for vector-valued random fields based on wavelet analysis: application to turbulent velocity and vorticity 3d numerical data. *Stochastic Environmental Research and Risk Assessment (SERRA)*. 67

Kestener, P., Lina, J.M., Saint-Jean, P. & Arneodo, A. (2001). Wavelet-based multifractal formalism to assist in diagnosis in digitized mammograms. *Image Anal. Stereol.*, **20**, 169. 86, 88

Kestener, P., Conlon, P., Khalil, A., Fennell, R., L. McAteer, Gallagher, P. & Arneodo, A. (2009). Characterising Complexity in Compound Systems I: Segmentation in Wavelet-Space. *Astrophys. J.*, submitted. 85

Khalil, A., Joncas, G., Nekka, F., Kestener, P. & Arneodo, A. (2006). Morphological analysis of h i features. ii. wavelet-based multifractal formalism. *The Astrophysical Journal Supplement Series*, **165**, 512–550. 63

Khalil, A., Joncas, G., Nekka, F., Kestener, P. & Arneodo, A. (2006). Morphological Analysis of H I Features. II. Wavelet-based Multifractal Formalism. *Astrophys. J. Suppl. Series*, **165**, 512–550. 67

Khalil, A., Grant, J.L., Caddle, L.B., Atzema, E., Mills, K.D. & Arneodo, A. (2007). Chromosome territories have a highly nonspherical morphology and nonrandom positioning. *Chromosome research : an international journal on the molecular, supramolecular and evolutionary aspects of chromosome biology*, **15**, 899–916. 88

Kolmogorov, A.N. (1941). *C. R. Acad. Sci. USSR*, **30**, 301. 41

Kulsrud, R.M. (2001). Magnetic reconnection: Sweet-Parker versus Petschek. *Earth, Planets, and Space*, **53**, 417–422. 19

Lawerence, J.K., Ruzmaikin, A. & A.C., C. (1993). Multifractal measure of the solar magnetic field. *The Astrophysical Journal*, **417**, 805–811. 58, 64

Lawrence, J.K., Cadavid, A.C. & Ruzmaikin, A.A. (1996). On the Multifractal Distribution of Solar Magnetic Fields. *Astrophys. J.*, **465**, 425–+. 71

LESUR, G. & LONGARETTI, P. (2005). On the relevance of subcritical hydrodynamic turbulence to accretion disk transport. *Astron. Astrophys.*, **444**, 25–44. xiv, 42

LIM, E.K., JEONG, H., CHAE, J. & MOON, Y.J. (2007). A Check for Consistency between Different Magnetic Helicity Measurements Based on the Helicity Conservation Principle. *Astrophys. J.*, **656**, 1167–1172. 50

LONG, D.M., GALLAGHER, P.T., MCATEER, R.T.J. & BLOOMFIELD, D.S. (2008). The Kinematics of a Globally Propagating Disturbance in the Solar Corona. *Astrophys. J. Lett.*, **680**, L81–L84. 109, 125

MACH, J. & MAS, F. (1997). Mfrac v2.0: Software for fractal and multifractal indices calculation. `http://www.qf.ub.es/d2/jordi/mfrac.html`. 72, 74

MANDELBROT (1983). *The Fractal Geometry of Nature*. New York: Freeman. 59, 72

MANDELBROT, B.B. (1974a). Intermittent turbulence in self-similar cascades: divergence of high moments and dimension of the carrier. *Journal of Fluid Mechanics*, **62**, 331–358. 42, 57, 66

MANDELBROT, B.B. (1974b). Multiplications alatoires itres et distributions invariantes par moyenne pondre alatoire. *C. R. Acad. Sci. Paris Ser. A*, **278**, 289,355. 54

MANDELBROT, B.B. (1977). *Fractals : Form, Chance and Dimensions*. Freeman, San Francisco. 54

MANDELBROT, B.B. & VAN NESS, J.W. (1968). *S.I.A.M. Rev.*, **10**, 422. 42

MCATEER, R.T.J., GALLAGHER, P.T. & IRELAND, J. (2005a). Statistics of Active Region Complexity: A Large-Scale Fractal Dimension Survey. *Astrophys. J.*, **631**, 628–635. xvi, xx, 16, 21, 58, 60, 71, 81, 82, 86, 88, 97, 98, 106, 107

McAteer, R.T.J., Gallagher, P.T., Ireland, J. & Young, C.A. (2005b). Automated Boundary-extraction And Region-growing Techniques Applied To Solar Magnetograms. *Solar Phys.*, **228**, 55–66. 72

McIntosh, P.S. (1990). The classification of sunspot groups. *Solar Physics*, **125**, 251–267. 10

Meneveau, C. & Sreenivasan, K.R. (1991). The multifractal nature of turbulent energy dissipation. *Journal of Fluid Mechanics*, **224**, 429–484. 57, 66

Metcalf, T.R., Jiao, L., McClymont, A.N., Canfield, R.C. & Uitenbroek, H. (1995). Is the solar chromospheric magnetic field force-free? *Astrophys. J.*, **439**, 474–481. 126

Metcalf, T.R., Leka, K.D. & Mickey, D.L. (2005). Magnetic Free Energy in NOAA Active Region 10486 on 2003 October 29. *Astrophys. J. Lett.*, **623**, L53–L56. 126

Metcalf, T.R., Derosa, M.L., Schrijver, C.J., Barnes, G., van Ballegooijen, A.A., Wiegelmann, T., Wheatland, M.S., Valori, G. & McTtiernan, J.M. (2008). Nonlinear Force-Free Modeling of Coronal Magnetic Fields. II. Modeling a Filament Arcade and Simulated Chromospheric and Photospheric Vector Fields. *Solar Phys.*, **247**, 269–299. 16, 46

Mostelle, F. & Tukey, J.W. (1977). *Data and Analysis and Regression*. Addison-Wesley. 74

Muzy, J., Elezgaray, J., Bacry, E., Argoul, F. & Arneodo, A. (1995). *Ondelettes, Multifractales et Turbuleces. De l'ADN auxcroissances cristallines*. Diderot Editeur Arts Sciences. 63

MUZY, J.F., BACRY, E. & ARNEODO, A. (1991). Wavelets and multifractal formalism for singular signals: Application to turbulence data. *Physical Review Letters*, **67**, 3515–3518. 67

MUZY, J.F., BACRY, E. & ARNEODO, A. (1993). Multifractal formalism for fractal signals: The structure-function approach versus the wavelet-transform modulus-maxima method. *Phys. Rev. E*, **47**, 875–884. 67

MUZY, J.F., BACRY, E. & ARNEODO, A. (1994). The multifractal formalism revisited with wavelets. *Int. J. of Bifurcation and Chaos*, **4**, 245. 67

NATIONAL ACADEMIES PRESS (2008). Severe space weather events–understanding societal and economic impacts: A workshop report. In *Severe Space Weather Events–Understanding Societal and Economic Impacts: A Workshop Report*, The National Academies Press. 1

O'NEILL, I.J. (2006). *Quiescent Coronal Loops Heated by Turbulence*. Thesis submitted to The University of Wales by Ian James ONeill MPhys (Wales) In Candidature for the Degree of Philosophiae Doctor. xii, 6

OSTERBROCK, D.E. (1961). The Heating of the Solar Chromosphere, Plages, and Corona by Magnetohydrodynamic Waves. *Astrophys. J.*, **134**, 347–+. 32

PARISI, G. & FRISCH, U. (1985). Fully developed turbulence and intermittency. In M. Ghil, R. Benzi & G. Parisi, eds., *Turbulence and Predictability in Geophysical Fluid Dynamics and Climate Dynamics*, Proc. of Int. School, 84, North-Holland, Amsterdam. 43, 66

PARKER, E.N. (1957). Acceleration of Cosmic Rays in Solar Flares. *Physical Review*, **107**, 830–836. 19

Pence, W. (1999). CFITSIO, v2.0: A New Full-Featured Data Interface. In D. M. Mehringer, R. L. Plante, & D. A. Roberts, ed., *Astronomical Data Analysis Software and Systems VIII*, vol. 172 of *Astronomical Society of the Pacific Conference Series*, 487–+. 73

Petschek, H.E. (1964). Magnetic Field Annihilation. *NASA Special Publication*, **50**, 425–+. 19

Phillips, K. (1998). Book Review: Guide to the sun / Cambridge U Press, 1992 ; paperback 1995. *Mercury*, **27**, 32. 8

Phillips, K.J.H., Chifor, C. & Landi, E. (2005). The High-Temperature Response of the TRACE 171 Å and 195 Å Channels. *Astrophys. J.*, **626**, 1110–1115. 27, 109

Pontieri, A., Lepreti, F., Sorriso-Valvo, L., Vecchio, A. & Carbone, V. (2003). A Simple Model for the Solar Cycle. *Solar Phys.*, **213**, 195–201. 96

Pontrjagin, L. & Schnirelmann, L. (1932). Sur une propriété métriue de la dimension. *Annals of Mathematics*, **33**, 156–162. 59

Prialnik, D. (2000). *An Introduction to the Theory of Stellar Structure and Evolution*. 3

Priest, E. & Forbes, T. (2000). *Magnetic Reconnection*. Magnetic Reconnection, by Eric Priest and Terry Forbes, pp. 612. ISBN 0521481791. Cambridge, UK: Cambridge University Press, June 2000. 19

Qahwaji, R. & Colak, T. (2007). Automatic Short-Term Solar Flare Prediction Using Machine Learning and Sunspot Associations. *Solar Phys.*, **241**, 195–211. 11

Raftery, C.L., Gallagher, P.T., Milligan, R.O. & Klimchuk, J.A. (2009). Multi-wavelength observations and modelling of a canonical solar flare. *Astron. Astrophys.*, **494**, 1127–1136. 115

Régnier, S. (2007). Nonlinear force-free field extrapolation: numerical methods and applications. *Memorie della Societa Astronomica Italiana*, **78**, 126. 126

Roux, S.G., Arnéodo, A. & Decoster, N. (2000a). A wavelet-based method for the multifractal image analysis. iii. applications to high-resolution satellite images of cloud structure. *Eur. Phys. J.*, **15**, 765–786. 63

Roux, S.G., Arnéodo, A. & Decoster, N. (2000b). A wavelet-based method for multifractal image analysis. III. Applications to high-resolution satellite images of cloud structure. *European Physical Journal B*, **15**, 765–786. 86

Sakurai, T. (1982). Green's Function Methods for Potential Magnetic Fields. *Solar Phys.*, **76**, 301–321. 47

Scherrer, P.H., Bogart, R.S., Bush, R.I., Hoeksema, J.T., Kosovichev, A.G., Schou, J., Rosenberg, W., Springer, L., Tarbell, T.D., Title, A., Wolfson, C.J., Zayer, I. & MDI Engineering Team (1995). The Solar Oscillations Investigation - Michelson Doppler Imager. *Solar Phys.*, **162**, 129–188. 23

Schmidt, H.U. (1964). On the Observable Effects of Magnetic Energy Storage and Release Connected With Solar Flares. *NASA Special Publication*, **50**, 107–+. 47

Schrijver, C.J. & Aschwanden, M.J. (2002). Constraining the Properties of Non-radiative Heating of the Coronae of Cool Stars and the Sun. *Astrophys. J.*, **566**, 1147–1165. xv, 53

Schrijver, C.J., Derosa, M.L., Metcalf, T.R., Liu, Y., McTiernan, J., Régnier, S., Valori, G., Wheatland, M.S. & Wiegelmann, T. (2006). Nonlinear Force-Free Modeling of Coronal Magnetic Fields Part I: A Quantitative Comparison of Methods. *Solar Phys.*, **235**, 161–190. xv, 46, 51

Schrijver, C.J., DeRosa, M.L., Metcalf, T., Barnes, G., Lites, B., Tarbell, T., McTiernan, J., Valori, G., Wiegelmann, T., Wheatland, M.S., Amari, T., Aulanier, G., Démoulin, P., Fuhrmann, M., Kusano, K., Régnier, S. & Thalmann, J.K. (2008). Nonlinear Force-free Field Modeling of a Solar Active Region around the Time of a Major Flare and Coronal Mass Ejection. *Astrophys. J.*, **675**, 1637–1644. 46

Schroeder, M. (1991). *Fractals, chaos, power laws. Minutes from an infinte paradise*. New York: Freeman. 54

SpaceWeather (2006). Mount wilson sunspot magnetic classification. `www.spaceweather.com/glossary/magneticclasses.html`. xxiv, 11

Sweet, P.A. (1958). The Neutral Point Theory of Solar Flares. In B. Lehnert, ed., *Electromagnetic Phenomena in Cosmical Physics*, vol. 6 of *IAU Symposium*, 123–+. 19

Taylor, A.R., Gibson, S.J., Peracaula, M., Martin, P.G., Landecker, T.L., Brunt, C.M., Dewdney, P.E., Dougherty, S.M., Gray, A.D., Higgs, L.A., Kerton, C.R., Knee, L.B.G., Kothes, R., Purton, C.R., Uyaniker, B., Wallace, B.J., Willis, A.G. & Durand, D. (2003). The Canadian Galactic Plane Survey. *Astronom. J.*, **125**, 3145–3164. 67

Turiel, A., Pérez-Vicente, C.J. & Grazzini, J. (2005). Numerical methods for the estimation of multifractal singularity spectra in sampled data: a comparative study. *Elsevier Science*, submitted March 13th 2005. 59

Vlahos, L. & Georgoulis, M.K. (2004). On the Self-Similarity of Unstable Magnetic Discontinuities in Solar Active Regions. *Astrophys. J. Lett.*, **603**, L61–L64. 127

Wang, Y.M. & Sheeley, N.R., Jr. (1992). On potential field models of the solar corona. *Astrophys. J.*, **392**, 310–319. 16

Welsch, B.T., Abbett, W.P., De Rosa, M.L., Fisher, G.H., Georgoulis, M.K., Kusano, K., Longcope, D.W., Ravindra, B. & Schuck, P.W. (2007). Tests and Comparisons of Velocity-Inversion Techniques. *Astrophys. J.*, **670**, 1434–1452. 16

Wiegelmann, T., Inhester, B., Lagg, A. & Solanki, S.K. (2005). How To Use Magnetic Field Information For Coronal Loop Identification. *Solar Phys.*, **228**, 67–78. 114, 115

Wuelser, J.P., Lemen, J.R., Tarbell, T.D., Wolfson, C.J., Cannon, J.C., Carpenter, B.A., Duncan, D.W., Gradwohl, G.S., Meyer, S.B., Moore, A.S., Navarro, R.L., Pearson, J.D., Rossi, G.R., Springer, L.A., Howard, R.A., Moses, J.D., Newmark, J.S., Delaboudiniere, J.P., Artzner, G.E., Auchere, F., Bougnet, M., Bouyries, P., Bridou, F., Clotaire, J.Y., Colas, G., Delmotte, F., Jerome, A., Lamare, M., Mercier, R., Mullot, M., Ravet, M.F., Song, X., Bothmer, V. & Deutsch, W. (2004). EUVI: the STEREO-SECCHI extreme ultraviolet imager. In S. Fineschi & M. A. Gummin, ed., *Society of Photo-Optical Instrumentation Engineers (SPIE) Conference Series*, vol. 5171 of *Society of Photo-Optical Instrumentation Engineers (SPIE) Conference Series*, 111–122. xiv, 28, 29

Zirin, H. (1988). *Astrophysics of the Sun*. Cambridge University Press. 10